Universidade de Aveiro Departamento de Engenharia Mecânica
2019

José Miguel
Clemente Costa

Desenvolvimento de um modelo pormenorizado das veias meníngeas
Development of a detailed bridging veins model

Universidade de Aveiro Departamento de Engenharia Mecânica
2019

José Miguel
Clemente Costa

Desenvolvimento de um modelo pormenorizado das veias meníngeas
Development of a detailed bridging veins model

Dissertação apresentada à Universidade de Aveiro para cumprimento dos requisitos necessários à obtenção do grau de Mestre em Engenharia Mecânica, realizada sob orientação científica de Ricardo José Alves de Sousa, Professor Auxiliar com Agregação do Departamento de Engenharia Mecânica da Universidade de Aveiro e de Fábio António Oliveira Fernandes, Inverstigador Júnior do Departamento de Engenharia Mecânica da Universidade do Aveiro.

Esta dissertação teve o apoio dos projetos

UID/EMS/00481/2019-FCT - FCT - Fundação para a Ciência e a Tecnologia;

CENTRO-01-0145-FEDER-022083 - Programa Operacional Regional do Centro (Centro2020), através do Portugal 2020 e do Fundo Europeu de Desenvolvimento Regional;

O júri / The jury

Presidente / President

Prof. Doutor Rui António da Silva Moreira
Professor Auxiliar da Universidade de Aveiro

Vogais / Committee

Prof. Doutor Marco Paulo Lages Parente
Professor Auxiliar da Faculdade de Engenharia da Universidade do Porto

Prof. Doutor Fábio António Oliveira Fernandes
Inverstigador Júnior da Universidade de Aveiro (co-orientador)

Agradecimentos / Acknowledgements

O concluir desta dissertação é o culminar de uma longa jornada que não seria possível fazer sem ajuda.

Antes demais, gostaria de deixar os meus sinceros agradecimentos ao professor Ricardo Sousa e ao professor Fábio Fernandes por toda a disponibilidade e apoio prestado ao longo deste trabalho, assim como os conhecimentos técnicos e palavras de confiança nos momentos mais atribulados deste percurso.
Por fim e mais importante, gostaria de agradecer à minha família, especialmente à minha mãe e à minha irmã, por todo o apoio prestado desde o início da minha aventura escolar que culminou nesta dissertação. Pois sem elas provavelmente esta conquista não seria possível.

Palavras-chave

veias meníngeas; seio sagital superior; traumatismo cranioencefálico; hematoma subdural agudo; elementos finitos; aceleração linear; aceleração rotacional.

Resumo

O traumatismo cranioencefálico é uma das maiores causas de morte e incapacidade no mundo. Uma das lesões mais frequentes e com maior taxa de mortalidade, resultante de um traumatismo craniano, é o hematoma subdural agudo. Dada a importância deste tipo de lesões é necessário criar limites e critérios de dano. Para obter estes limites e critérios de dano, é necessário efectuar testes experimentais em cadáveres humanos, animais ou dummies. No entanto, devido a problemas éticos e económicos, cada vez mais os modelos de elementos finitos são uma boa alternativa. Uma vez validado, o modelo de elemetos finitos da cabeça é uma mais valia, que pode ser utilizado como ferramenta de design no desenvolvimento de equipamentos para proteção da cabeça e na reconstrução de lesões como o traumatismo craniano. O YEt Another Head Model (YEAHM) é exemplo de um desses modelos que pode ser utilizado para substituir ou auxiliar os testes experimentais. O YEAHM já tem incorporado um modelo de veias meníngeas que ajuda na detecção de hematomas subdurais agudos, no entanto este modelo apresenta geometria irrealista e falhas na validação. No estudo realizado neste trabalho esse modelo foi melhorado e validado. A validação consiste no cálculo da taxa de sucesso que o modelo consegue obter na detecção de rupturas das veias meníngeas. No fim, foi obtido um modelo 3D de elementos finitos das veias meníngeas que tem em consideração a pressão sanguínea. Os resultados mostram que o modelo obteve uma taxa de sucesso máxima de 90%, e em comparação com outros modelos já desenvolvidos consegue resultados iguais ou melhores. Para concluir, é possível afirmar que o modelo desenvolvido neste trabalho é um grande passo nos modelos de elementos finitos das veias meníngeas.

Keywords bridging veins; superior sagittal sinus; traumatic brain injury; acute subdural hematoma; finite elements; linear acceleration; rotational acceleration.

Abstract

Traumatic brain injury is one of the major causes of death and disability in the world. One of the most frequent and deadly injury resulted from a head trauma is acute subdural hematoma (ASDH), which consists on the rupture of a bridging vein (BV). Given the importance of this type of injury, it is necessary to set thresholds and damage criteria. To access this thresholds and damage criteria, experimental tests performed on human cadavers, animals or dummies are required. However due to ethical and economical issues, more and more the finite element (FE) models are becoming a very good cost-effective alternative. Once properly validated, the finite element head model (FEHM) is a valuable tool, that can be used in the development of head protective gear as a design tool and in the reconstruction of head traumas by predicting brain injuries under impact conditions. The YEt Another Head Model (YEAHM) is the example of a FE model that can be used to assist/replace the experimental tests. The YEAHM already has a bridging veins FE model to help on the prediction of ASDH. However, this model presents unrealistic geometry and lacks validation. In this study the bridging veins FE model was improved and validated. The validation consists on the calculation of the model prediction success rate. At the end, it was obtained a 3D bridging veins FE model with tubular shape that takes in consideration the blood pressure. Results showed that this model presents a maximum success rate of 90% and, in comparison with FE models already developed, presents equal or even better prediction results. In summary, it can be stated that the model developed in this work is a big step in field of bridging veins FE models.

Contents

List of Tables

List of Figures

Acronyms

ASDH	Acute subdural haematoma
AIS	Abbreviated injury scale
BC	Boundary condition
BV	Bridging vein
CNS	Central nervous system
CSDM	Cumulative strain damage measure
CSF	Cerebrospinal fluid
CT	Computed tomography
CTE	Chronic traumatic encephalopathy
DAI	Diffuse axonal injury
DBI	Diffuse brain injury
DDM	Dilaation damage measure
EDH	Epidural haematoma
FE	Finite element
FEA	Finite element analysis
FEHM	Finite element head model
GAMBIT	Generalized acceleration model for brain injury threshold
HIC	Head injury criterion
HIP	Head injury power
KTH	Kungliga Tekniska Högskolan
MRI	Magnetic resonance imaging
MTBI	Mild traumatic brain injury
OD	Outer diameter
PI	Power index
PLA	Peak linear acceleration
PNS	Peripheral nervous system
RMDM	Relative motion damage measure
SDH	Subdural haematoma
SEDF	Strain energy density function
SIMon	Simulated Injury Monitor
SSS	Superior sagittal sinus
TBI	Traumatic brain injury
UCDBTM	University College Dublin Brain Trauma Model
UDS	University of Strasbourg
ULP	University of Louis Pasteur
WSTC	Wayne State Tolerance Curve
WSUBIM	Wayne State University Brain Injury Model
YEAHM	Yeat Another Head Model

Nomenclature

Ψ	Strain energy density function
$\boldsymbol{S}$	Stress tensor
$\boldsymbol{E}$	Lagrangian strain tensor
C	Cauchy-Green tensor
$\overline{C}$	Deviatoric part of the Cauchy-Green tensor
I	Stress invariant
$\overline{I_1}$	First invariant of the Cauchy-Green tensor
J	Volume ratio
U	Displacement vector
F	Deformation gradient
$\overline{F}$	Deviatoric part of the deformation gradient
λ	Lamé's first parameter
μ	Lamé's second parameter
$\boldsymbol{E}_{lin}$	Linear version of Lagrangian strain tensor
E	Young's modulus
ν	Poisson's ratio
σ_U	Rupture stress
ε_U	Rupture strain
σ_Y	Yield stress
ε_Y	Yield strain
K	Bulk modulus
a	linear acceleration
α	angular acceleration
ω	angular velocity
G	GAMBIT value
n, m, s	GAMBIT empirical constants
M	Mass of the head
I_{xx}, I_{yy}, I_{zz}	Moments of inertia
ρ	Density
η	stress triaxiality
p	pressure stress
q	Mises equivalent stress
ω_D	state variable

Chapter 1

Introduction

1.1 Motivation

Traumtic brain injury (TBI) will become the major cause of death and disability in children and young adults by the year of 2020 according to the World Health Organization [1]. This may lead to serious public health problems with high social and economic costs [2], not only because the mortality rate of trauma with head injury is almost triple that of trauma without head injury [3], but also because it leads to a higher lifelong disability rate.

TBI can be caused by a wide range of day-to-day activities, from car and bicycle related accidents to the practice of sports such as motor sports, hockey, soccer, football, cycling, winter sports, among others.

There are several types of head injuries, such as skull fracture, subdural heamatoma (SDH), cerebral contusions, diffuse axonal injury (DAI), chronic traumatic encephalopathy (CTE), epidural hematoma (EDH), etc. These ones are, according to Monea *et al.* [1], the most frequent head injuries resulting from bicycle-related accidents. In sports, the most common head injury is concussion, but the one that as the highest death rate is acute subdural heamatoma ASDH. Studies reveal reports of the occurence of ASDH, skull fracture and epidural heamatoma after being struck on the head by a soccer ball [4-7]. Even in contact against another player there are reports of EDH and SDH, but in this case the most common to occur is contusion [8; 9].

Among every sports, one of the most prone to concussion and severe head injury is fighting sports [10]. In judo, chronic SDH and other forms of intracranial hemorrhage have been reported, and ASDH is indicate as the biggest cause of death in boxing.

Car accidents are one of the main causes of death in the world and the majority of the injuries that lead to this high mortality rate occurs in the head. ASDH is one of the most frequent injury resulting from head trauma, being the most frequent traumatic head injury in bicycle-related accidents. Statistically, 26% to 63% of all closed head injuries are consider to be ASDH [11], with a mortality rate ranging from 30% to 90%[12; 13].

Although concussion is related as the most common head injury, ASDH is the one with highest mortality rate. The rupture of a bridging vein (BV), which is in charge of draining blood from the cerebral cortex into the superior sagittal sinus, is hypothesised as one of the major causes of ASDH alongside with hemorrhagic contusion or intracranial hematoma and the laceration of a cortical artery or vein [12].

For the reasons mencioned above, there is a need for biomechanical studies of head

injury, in order to predict the thresholds for the external loadings, which could be used in the development of protective gear such as helmets. There are two ways to assess these thresholds, experimentally or with computational simulation. It is obvious that experimental tests are very hard to perform, because the only way is to use human cadavers or animals. However, dead tissue is different than living tissue, and even though some animals like porcines and simians have similar tissue to humans their body mechanics are different, an impact to a erectus body will have different mechanics. So, the best option is to develop a very accurate computacional head model. Finite element head models (FEHMs) are a very cost-effective alternative to the experimental method, however they face a big challenge, the validation, which besides being dificult to do, is highly dependent on the post-mortem experimental tests. Nevertheless, once the model is validated, it is no longer necessary to use specimens. Also, with computacional head models it is possible to study intracranial injuries, which could not be done with post-mortem experiments.

This work focus on the development and validation of a detailed 3D finite element bridging veins model that later can be used to detect ASDH. This would be a big step in the field of the FEHMs, since every model of BVs developed so far use 3D structural elements (beam, truss) and have a validation ratio lower than 90%.

1.2 Objectives

The main goal of this work is to improve and validate the model already created by Migueis [14] of the superior sagittal sinus (SSS), transverse sinuses, straight sinus and bridging veins, in order to have an accurate model to study the ASDH and to help on the development of head protections by setting the tresholds of the external loadings that leads to head injuries.

First, state-of-the-art had to be studied in order to understand how bridging veins work, their anatomy, mechanical properties, what finite element models already exist and the thresholds criteria to define the model. The second task after the state-of-the-art, was to choose the mechanical properties of the BVs, and then use the Explicit version of the FE package ABAQUS to try to validate, with a simplistic BV geometry, the material model and damage model, and also choose the type of finite element. This conditions are the same that are going to be used in the full model.

The third step was to improve the CAD model that was developed by Migueis [14] and make it more similar to reality, giving it thickness, changing from a filled cylindrical shape into a pipe-like structure, and smoothing the intersections between the bridging veins and the superior sagittal sinus.

Moreover, the fourth step was to take the improved bridging veins CAD model and incorporate on the YEAHM model, developed and validated by Fernandes et al. [15], and finally use the Explicit version of the FE package ABAQUS to recreate the experimental tests conducted by Depreitere and his colleagues [12] in order to validate the BVs model.

1.3 Lecture guide

- **Chapter 1** - Introduction

  Chapter 1 is composed of three parts. Motivation, where a brief contextualization is made, explaining the reasons that led to this work, the main goals and some

general background fundamental to understand the work developed in the further chapters. Objectives, where the main goal is explained and all the phases that the work had to go through in order to get there. Finally, a lecture guide is presented to supply the reader with a practical reading guide.

- **Chapter 2** - State-of-the-art review

  Chapter 2 presents the state-of-the-art. A brief introduction to the head anatomy is presented, explaining the different parts of the brain, how it is divided, and the layers that exist to protect him. Then, the bridging veins are focused, since they are the principal subject of this work. Their anatomy and mechanical properties are studied, which will make possible further in this work model the veins, both materially and geometrically. After, the head injuries are described and categorized, being explained the biomechanics and mechanisms of head injuries and associated thresholds. Finally, it is made a literature review about finite element head models where it is explained their evolution along the years, focusing on the Yet Another Head Model (YEAHM), which will be used in this work to assembly the model of the bridging veins.

- **Chapter 3** - Bridging veins models

  This chapter can be divided into three main parts. The first part describes the process of the material validation, using both solid and shell elements, and which one was chosen to be used on the full FE BV+SSS model. The second part, describes the process behind the development of the 3D CAD model. Finally, the third part tackles the SSS-BV intersection problem, being explained the reasons behind the choice of the fillet size.

- **Chapter 4** - Bridging veins FE model

  This chapter starts by describing the experimental tests conducted by Depreitere and his colleagues, that served as reference to validate the bridging veins FE model using the software ABAQUS. After that, the FE model initial definitions are explained as well as the problems associated with them and the new improved definitions. Then the FE model validation results are presented, as well as the results obtained by other authors that work on the success rate of FE models to predict ASDH. Finally, the results obtained in this work are discussed and compared with results from other authors.

- **Chapter 5** - Conclusions and future work

  This chapter presents general conclusions and discuss the results obtained in this work, as well as some suggestions and ideas to implement in future works related to this study.

Chapter 2

State-of-the-art review

2.1 Head anatomy

The head is a very complex structure, that includes the skull, brain, meninges, blood vessels such as bridging veins and nerves.

In this section it is described the head anatomy, explaning the different parts of the head, their characteristics and functions. After that, the bridging veins properties are studied, geometrically and mechanically. Then, the types of injury that normally occurs in the head are adressed, both skull fractures and brain traumas.

Lastly, the different criteria and thresholds already reported by some authors are shown, as well as some computacional models already existing, giving special emphasis in the YEAHM, developed and validated by Fernandes *et al.* [15].

2.1.1 Nervous system

The nervous system is the part of the human body that collects information from within and the outside environment through our five senses (touch, sight, hearing, smell and taste) and then utilizes that information to send signals to parts of the body in order to coordinate their actions [16].

This system is divided in two parts: the central nervous system (CNS), illustrated on the left side of Figure 2.1, that is composed by the brain and spinal cord and the peripheral nervous system (PNS), illustrated on the right side of Figure 2.1, that is composed by cranial and spinal nerves whose main function is to connect the CNS to the limbs and organs.

This work will focus on the CNS since the main study elements are the brain, meninges and more specifically the bridging veins.

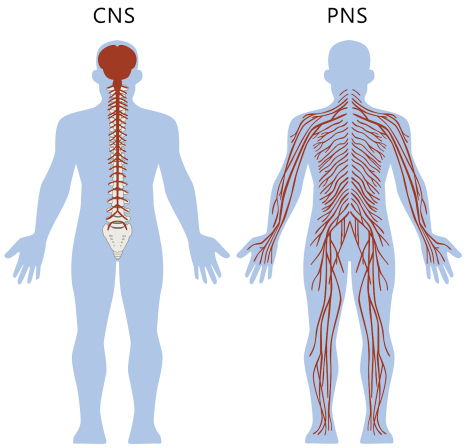

Figure 2.1: Nervous system illustration, on the right side the PNS and on the left the CNS [17].

2.1.2 Brain anatomy

The human brain is one of the most important organs, that controls all functions of the body, it receives information through our five senses: sight, smell, touch, taste and hearing, utilizing that information to take the necessary actions to move our body, control the speech and emotions [18]. It is also capable of storing memmory.

The brain is divided in three major areas: cerebrum, cerebellum and brainstem (Figure 2.2).

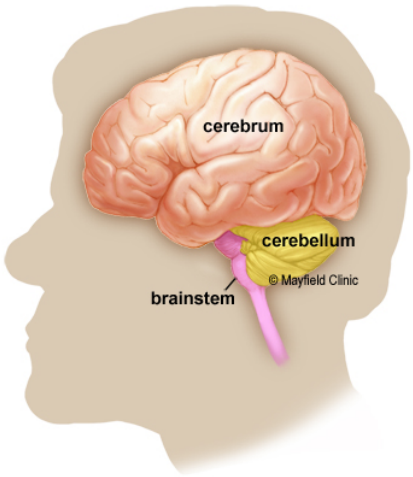

Figure 2.2: The three major areas of the brain: cerebrum, cerebellum and brainstem. Adapted from Mayfield Brain & Spine [18].

2.1.2.1 Cerebrum

The cerebrum is the largest part of the brain, divided into two hemispheres, the right and left connected by the corpus callosum. Each hemisphere controls the opposite side of the body, but they do not share the same functions. While, the left hemisphere controls speech, comphrension, arithmetic and writing skills, the right side controls creactivity, spatial ability, artistic and musical skills. According to Mayfield Brain & Spine [18], the left hemisphere is dominant in hand use and language in about 92%.

The two hemispheres are each one divided in four lobes (Figure 2.3): frontal, temporal, parietal and occipital. Each lobe is once again divided into areas that have specific functions.

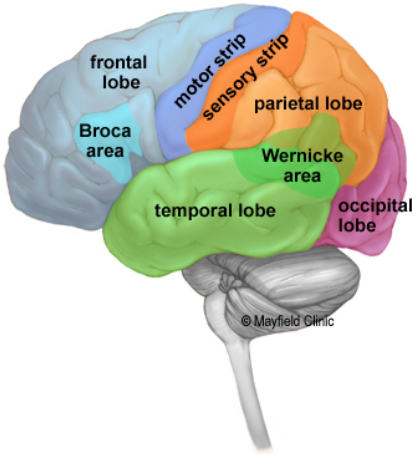

Figure 2.3: The four lobes of the brain: frontal, parietal, occipital and temporal. Adapted from Mayfield Brain & Spine [18].

Frontal lobe:

The frontal lobe, as shown in light blue in Figure 2.3, is the largest of the four lobes and is the last one to develop, continuing to create neural connections until a person's mid-twenties [19]. This late maturation makes the frontal lobe highly malleable and susceptible to development damage, which means that brain damage early in life may affect cognition and behaviour forever.

Its located just behind the forehead under the frontal skull bones, in the front part of the cerebrum. The central sulcus separates the frontal and parietal lobes, while the lateral sulcus separates the frontal and temporal lobes.

Highly social mammals have larger and more developed frontal lobes than any other animal, which establishes a connection between social interactions and the lobe development.

The main functions of the frontal lobe are: coordinating body movemets, help with language understanding and speech, impulse control, planning, judgment, problem solving, emmotional expression, concentration and self awareness [19].

The frontal lobe is probably the most prone to damage, because is the last one to fully develop and is located in the front part of the head which makes it more exposed to

impacts. Some consequences of frontal lobe damage are: aggresion, behaviour changes, difficulties with language, loss of memory, loss of motor control and spatial abilities [19].

Parietal lobe:

The parietal lobe, as shown in orange in Figure 2.3, is located just under the parietal bone of the skull, near the top and center of the cerebrum, just behind the frontal lobe and above the occipial and temporal lobes.

This lobe is the brain's primary sensory area, which is essential for sensory perception and senses' management. Besides the principal functions mentioned above, other functions are: some visual functions, assessing numerical relationships, coordinating hand, arm and eye motions, processing languages and coordinating attention [19].

Damage to the parietal lobe can lead to three main problems: if the injury is located on the right side, it can harm the ability to care for at least one side of the body; if the injury is on the left side it can cause Gerstmann's syndrome, which enables the capacity of writing, understanding arithmetic language and the ability to perceive objects; if the damage is both on the right and left side, may lead to a condition named Balint's syndrome which enables motor skills and visual attention [19].

Occipital lobe:

The occipital lobe, as shown in purple in Figure 2.3, is the smallest of the four lobes, located at the forebrain under the occipital bone of the skull.

This lobe is mainly dedicated to visual functions like: mapping the visual world, determinating color properties of the items in the visual field, assessing distance (size and depth), identifying visual stimulli, transmitting visual information to others brain regions, receiving raw visual data from perceptual senses in the eyes' retina [19].

The main effects of injury to the occiptal lobe are visual related, like: difficulties to perceive colors, shape, dimensions and size, inability to dettect if an object is moving, difficulty to recognize familiar objects and faces, and even blindness. Although there are others consequences such as epilepsy, hallucinations and difficulties with motor skills and balance [19].

Temporal lobe:

The temporal lobe, as shown in green in Figure 2.3, is located behind the temples at the forebrain, being fundamental in the process of sensory input such as pain and auditory stimulli, it also plays a role in visual memories, emotions and language understanding and speech production.

Damage to the temporal lobe may lead to very serious injuries, such as: life-threatening bleeding, blood clots, temporal lobe epilepsy, aphasia (disorder of speech and language), decrease of memory skills, changes in personality, develop of addictions, loss of impulse control, increase of aggression, loss of coordination and loss of spatial awareness [19].

2.1.2.2 Cerebellum

The cerebellum is located under the cerebrum and it is divided into three main areas: the neocerebellum that is responsible for motor control, the paleocerebellum that is responsible for posture, and the archicerebellum that is responsible for spatial orientation. Besides the functions mencioned above, the cerebellum may also be involved in some

cognitive functions such as attention and language.

2.1.2.3 Brainstem

The brainstem is the posterior part of the brain and the oldest part of the central nervous system, that connects the cerebrum and cerebellum to the spinal cord. It is responsible for breathing, cardiac regulation, respiratory functions, regulation of the CNS and regulation of the sleeping cycle.

2.1.3 Meninges

The human brain is a very delicate structure that needs protection. The first layer to offer that protection is the skull, which is a complex structure composed by 22 bones, being 21 one of them firmly attached to each others via sutures and only one movable, the mandible [16]. Besides the skull, the human body have three layers of membranes that provides protection and support to the brain and spinal cord (Figure 2.4).

The first layer just underneath the skull is the dura mater, which is a thick collagenous tissue that is divided in two layers: an outer vascular periosted and an inner meningeal layer.

Under the dura mater is the arachnoid mater, which is a thin transparent membrane with a spiderweb appearence, a space can be formed in the middle of these two layers in case of a trauma, this space is named subdural space.

The innermost layer beneath the arachnoid mater is the pia mater, which is a thin membrane composed of fibrous tissue, these two are separeted by the subarachnoid space that contains the cerebrospinal fluid (CSF).

The CSF is a colorless acellular fluid, produced by the choroid flexus that circulates in the ventricles of the brain, central canal of the spinal cord and subarachnoid space [16]. This fluid act like a hydrodinamic protective cushon, it also serves a vital function in the autoregulation of cerebral blood flow and in the removal of harmfull substances.

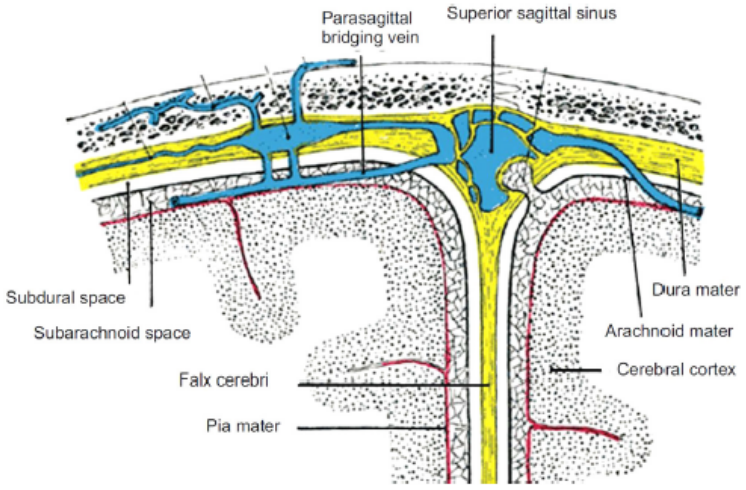

Figure 2.4: Human head layers: skull, meninges and brain. Adapted from Gray [20].

2.1.4 Bridging veins

Bridging veins (Figure 2.5) are located between the brain and skull, and their function is to drain blood from the cerebral cortex into the superior sagittal sinus (SSS) [21]. After this blood gets into the SSS, it is drained to the confluence of sinuses, which ultimately arrives to the internal jugular vein.

These veins exhibit complex mechanical behaviour, being nonlinear, viscoelastic and prone to damage [21], but these mechanical properties need to be studied in order to create a biofidelic finite element model. The FE model can be used to study the biomechanics of head impact and set up tolerance criteria, to then improve head gear and benefit forensic science.

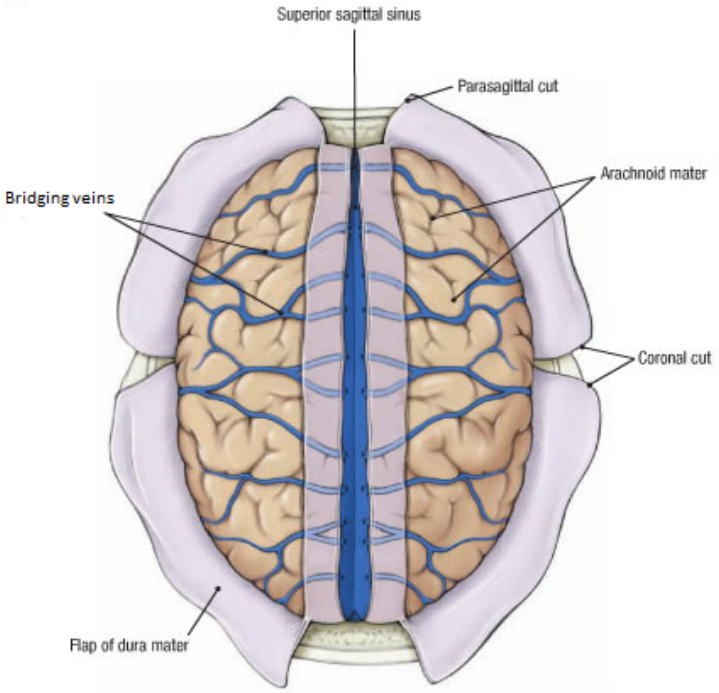

Figure 2.5: Illustration of the brain with the bridging veins and the SSS. Adapted from Duke University School of Medicine [22].

2.1.4.1 Bridging veins anatomy

Bridging veins (BVs) are fixed to the cranial side to the dura mater and in the cerebral side to the movable hemispheres.

An impact against the head causing and antero-posterior rotation is the one that can lead more easily to a BVs rupture, since there is no protection against this type of movement. The cerebral falx minimizes the lateral movement of the brain, making this movement less dangerous [21].

The direction of the confluence between the BVs and the superior sagittal sinus shows high variability [21], as firstly described by Oka *et al.* [23]. According to Brockmann *et al.* [24], there are five categories to describe this intersection (Figure 2.6): antegrade

(along the flow direction of the SSS), perpendicular, retrograde (opposed to the flow direction), hairpin shaped (changing direction shortly before entering the sinus) and lacunae (enlarged venous space). Naturally, the sharp edges are not present in reality, just in the illustration.

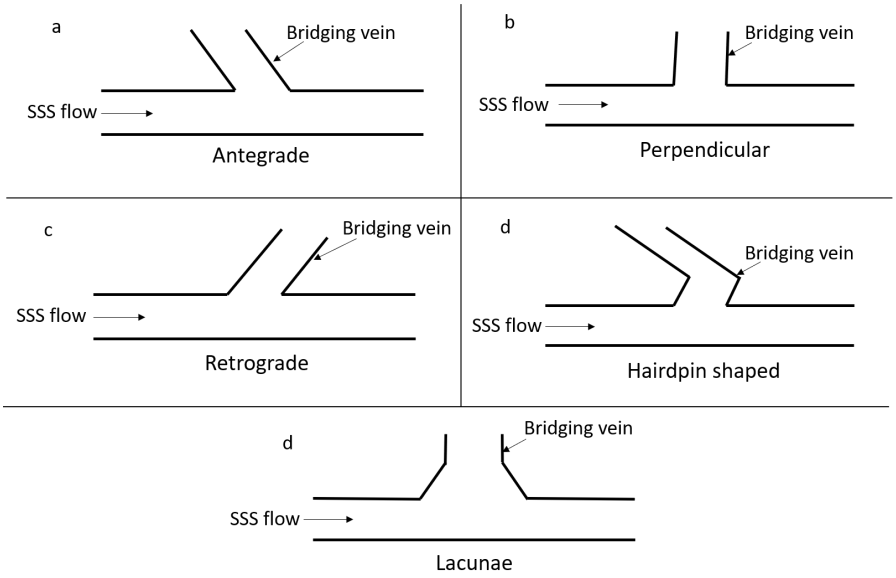

Figure 2.6: Illustration of the five categories of inflow from the bridging veins into the SSS according to Brockmann *et al.* [24].

According to Han *et al.* [25] the SSS can be divided in four segments (Figure 2.7), from anterior to posterior. The first two segments have an average length of about 5 cm, whereas the last two have about 7 cm.

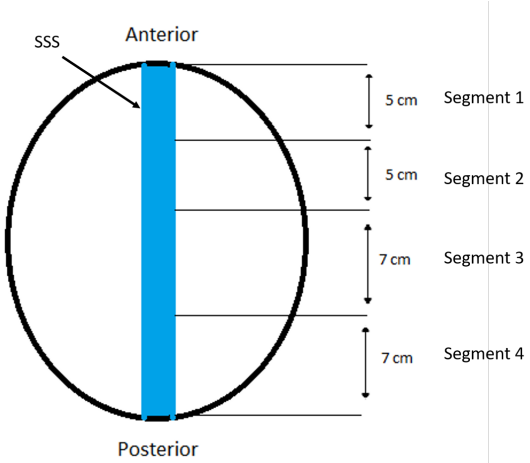

Figure 2.7: Illustration of the segments of the SSS according to Han *et al.* [25].

Han et al. [25] reported that segments 1 and 4 showed clusters of incoming BVs and segments 2 and 3 only had a few. On the other hand, Brockmann et al. [24] used the coronary suture, to describe the entrances of BVs along the SSS. For BVs at the level of the coronary suture, there is a dominat lacunae formation, followed by hairpin shaped inflow [21], for BVs at the level of the segment 3, the inflow is mainly retrograde, with an average angle of 35°, and about 2 cm anterior to the coronary suture the inflow is predominat antegrade. Han *el al.* [25] reported that BVs entering the SSS, at the level of segment 1, have various inflow directions: 20% antegrade, 40% prependicular and 40% retrograde [21].

Musigazi and Depreitere [26], after having performed a study on BV anatomy based on CT angiogram data from 78 patients, divided the cortex into 10 segments, as shown in Figure 2.8, that acted as landmarks to categorized the number of BVs and their entry angles on the SSS per segment. They reported that the highest number of BVs was in segment 5 with 30 %, followed by segments 4 and 6 with 20%. It was also reported an average of 0 to 3 bridging veins per segment and side, and a median angle of entrance on the SSS of 63 to 86° frontal and 44 to 76° parietal, being considered 180° frontal direction and 0° occipital direction.

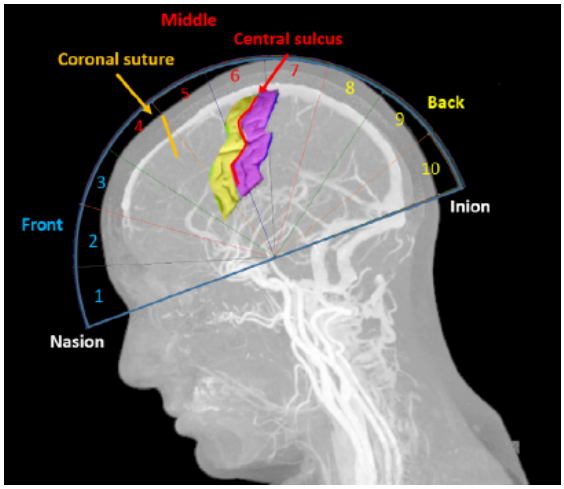

Figure 2.8: Segments used by Musigazi and Depreitere to categorize the number of BVs and their entry angles on the SSS along the cerebral cortex [27].

Table 2.1, shows the anatomical properties, length, outer diameter and wall thickness, of the bridging veins according to several authors.

The maximum outer diameter (OD) of a bridging vein reported is 5.3 mm and the minimum is 0.5 mm, this diameter varies significantly according to the location along the vein. The OD remains more or less constant along the subarachnoid portion. There are two major observation reports that describe the geometry of a bridging vein: Vignes *et al.* [28] states that, the diameter increases just before a region called the outflow cuff segment, near the SSS, and Pang *et al.* [29] states that the outflow cuff is connected to the SSS through the ampullar bulging.

Table 2.2, shows the different geometrical parameters of BVs reported by Monea *et al.* [1], separed by gender and for the general population.

Table 2.1: Bridging veins anatomical parameters according to different authors. Adapted from Famaey *et al.* [21].

Length (mm)	**Outer Diameter** (mm)	**Wall Thickness** (mm)	**Reference**
10-20	1-3	Subdural: 0.1±0.6 Subarachnoid: 0.05-0.2	[30]
0-70	0.5-5.3	-	[23]
6.42±4	1.4±0.63	0.05±0.02	[31]
-	0.5-4	-	[32]
-	1.4-3.1	-	[32]
-	1.84±0.35	0.12±0.02	[33]
Male: 22.11±7.6 Female: 17.92±5.93	Male: 2.7±0.85 Female: 2.71±1.06	Male: 0.03±0.01 Female: 0.04±0.02	[34]
-	0.5-4	-	[28]
- -	Cadavers: 2.5±1.1 DSA: 3.4±1.18	- -	[25]
-	3.42±1.18	0.044±0.017	[1]

Table 2.2: Bridging veins anatomical parameters, divided by gender and for the general population. Adapted from Monea *et al.* [1].

	No.	**Max SSS opening diameter dmax** (mm)	**Min BV diameter dmin** (mm)	**Mean SSS & BV diameter dmean** (mm)		**No.**	**Thickness** (mm)
All	125	4.99±1.86	1.88±0.83	3.42±1.18	**All**	130	0.044±0.0017
Females	57	4.53±1.67	1.66±0.64	3.09±1.04	**Females**	57	0.048±0.020
Males	68	5.39±1.94	2.02±0.93	3.43±1.18	**Males**	73	0.040±0.012

The venous wall of the bridging veins is divided in three layers (Figure 2.9) like any other venous wall, the three layers are:

Tunica adventitia:

The tunica adventitia is the surface that covers the outside of the vein. It is the thickest layer, containing scattered mesenchymal cells surrounded by connective tissue, that consists of an abundance of collagen and elastin fibres [30]. This layer also contains tiny blood vessels called vasa vasorum that supply to the wall of the veins.

Tunica media:

The tunica media is the middle layer, consisting of smooth muscle cells and elastin fibres. There is no consensus relating the smooth muscle cells, while Yamashima and Friede [30] and Vignes *et al.* [28] state that BVs wall have these cells, Pang *et al.* [29] and Kiliç and Akakin [35] observe that there is an absence of the smooth muscle layer. Pang *et al.* used porcine BVs, whereas Yamashima and Friede [30] and Kiliç and Akakin [35] used human specimens.

Tunica intima:

The tunica intima is the innermost layer, composed of multi-layered smooth endothe-

lium covered by elastin tissue [30]. This layer sometimes contains one-way valves to prevent the blood from flowing backwards.

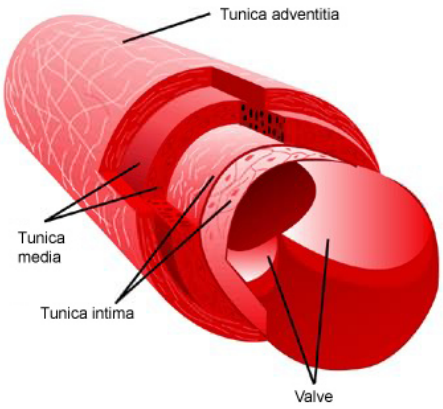

Figure 2.9: The three layers of the bridging veins. Adapted from Brad UK [36].

According to Yamashima and Friede [30] the thickness of the bridging veins wall has a high variability in the subdural portion.

The distribution of the collagen fibres shows differences along the BVs, while in the subdural portion the collagen fibres have a loose webbing patter, in the subarachnoid portion they have a more dense structure [30].

According to Pang *et al.* [29] and Niereberger *et al.* [37] the collagen fibres are mainly oriented in the longitudinal direction, whereas in the outflow cuff segment, the main orientation is circumferencial or helicoidal according to Vignes *et al.* [28]. Yamashima and Friede [30], state that more than half of the collagen fibres were circumferencial and that longitudinal fibres were much less abundant.

The limitation that the circumferencial orientation of the collagen fibres give in the diammeter of the outflow cuff segment, act as a valve that gives a dynamic resistance against sudden changes in blood flow [38].

2.1.4.2 Mechanical properties of bridging veins

Bridging veins reveal a complex mechanical behaviour, being described by Pant *et al.* [29] as nonlinear elastic, anisotropic, viscoelastic and prone to damage.

The mechanical behaviour of most materials can be described by the continuum mechanics-based constitutive relations [21]. To describe biological tissue can be used a wide range of constitutive relations, from the Hookean law to more complex mathematical expression [39].

For hyperelastic materials, the stress-strain relationship derives from a strain energy density function (SEDF). This function (Ψ) defines the potencial energy stored in a unit volume of a cube, relating the second Piola-Kirchhoff stress tensor ($\boldsymbol{S}$) and the Lagrangian strain tensor ($\boldsymbol{E}$):

$$\mathbf{S} = \frac{\delta \Psi(\mathbf{E})}{\delta \mathbf{E}} \tag{2.1}$$

The Lagrangian strain tensor is defined as a function of the right Cauchy-Green tensor as:

$$\mathbf{E} = \frac{1}{2}(\mathbf{C\text{-}I}), \tag{2.2}$$

or, directly as a function of the displacement vector $\boldsymbol{U}$ as:

$$\mathbf{E} = \frac{1}{2}(\nabla\mathbf{U} + \nabla\mathbf{U}^T + \nabla\mathbf{U}^T\nabla\mathbf{U}) \tag{2.3}$$

Since the biological material of bridging veins can be considered incompressible, the deformation is characterized in terms of the invariants of the deviatoric part $\overline{\mathbf{C}}$ of the right Cauchy-Green tensor $\boldsymbol{C}$.

$$\mathbf{C} = \mathbf{F}^T\mathbf{F} \tag{2.4}$$

and,

$$\overline{\mathbf{C}} = \overline{\mathbf{F}}^T\overline{\mathbf{F}} \tag{2.5}$$

where, $\boldsymbol{F}$ is the deformation gradient and $\overline{\mathbf{F}}$ is the deviatoric part of the deformation gradient.

Linear elasticity

The simplest case when analising the mechanical behaviour of a material is the linear regime, where the stress/strain relation is linear, which means that the mathematical formula of the SEDF is:

$$\Psi = \frac{\lambda}{2}(tr\mathbf{E}_{lin})^2 + \mu(tr\mathbf{E}_{lin}^2) \tag{2.6}$$

Being, λ the Lamé's first parameter, μ the Lamé's second parameter and E_{lin} the linearised version of the Langragian strain tensor. Usually, when dealing with linear regime is more common to use the Young's modulus E and the Poisson's ratio ν. The Lamé's coefficients can be related with these two parameters, using the following formulas:

$$\lambda = \frac{E\nu}{(1+\nu)(1-2\nu)} \tag{2.7}$$

$$\mu = \frac{E}{2(1+\nu)} \tag{2.8}$$

Linear theory is still widely used for mechanically characterize biological tissue [21], and with a simple tensile test the two parameters described above can be determined. Several authors have conducted these tests, the results are showned in the Table 2.3.

Table 2.3: Bridging veins mechanical properties according to different authors. Adapted from Famaey *et al.* [21].

σ_U (MPa)	ε_U (%)	σ_Y (MPa)	ε_Y (%)	E (MPa)	Reference
3.33±1.52	53±19.5	-	-	-	[31]
1.32±0.62	50±19	1.15±0.47	29± 9	6.43±3.44	[33]
4.99±2.55	25±8	4.13±2.14	18±7	30.69±19.40	[34]
4.19±2.37	29.82±13.26	1.73±1.37	12.85±13.35	25.72±15.86	[1]

Nonlinear elasticity

As said before, bridging veins are mainly composed of connective tissue, using the elastin fibres for low strain stimulation and the collagen fibres to high strain loading regimes [39-41]. There are two major nonlinear isotropic SEDFs used for vascular tissue, they are:

Fung and Cowin (1994) [44]

$$\Psi = \frac{c}{2}[e^Q - 1] \tag{2.9}$$

$$Q = A_1E_{11}^2 + A_2E_{22}^2 + 2A_3E_{11}E_{22} + A_4E_{12} + 2A_5E_{12}E_{11} + 2A_6E_{12}E_{22} \tag{2.10}$$

where c and A_i are the material parameters and the E_{ij} are the diferrent components of the Lagrangian strain tensor [45].

Neo-hookean (Famaey and Vander Sloten, 2008) [39]

$$\Psi = \frac{\mu}{2}(\overline{I}_1 - 3) + \frac{K}{2}(J-1)^2 \tag{2.11}$$

where μ is the shear modulus, K is the bulk modulus, $\overline{I}_1$ and J are the invariants of the Cauchy-Green strain tensor [21].

Anisotropy

According to Gasser *et al.* [46], the mechanical properties of the bridging veins tissue are orientation-dependent. The most common SEDF used for cardiovascular tissue that takes in consideration the anisotropy is the Holzapfel-Gasser-Ogden model [41]:

$$\Psi(I_1, I_4^*, I_6^*) = \frac{c}{2}(I_1 - 3) + \frac{k_1}{2k_2}\sum_{i=4,6}(exp[k_2(I_i^* - 1)^2] - 1) \tag{2.12}$$

where c>0 and k_1 are stress-like parameters, k_2 is a dimensionless parameter, and I_1^* is the pseudo-inveriant related to the fibre direction and can be written as [46]:

$$I_i^* = kI_1 + (1-3k)I_i, \quad I_i = \lambda_\theta^2\cos\alpha^2 + \lambda_z^2\sin\alpha^2, \quad i = 4, 6, ... \tag{2.13}$$

where α is the angle between the fiber direction and the circumferencial direction of the vessel, and k is a parameter related to the dispersion of the fibers [21].

Although the model above can be used for venous walls, its mainly purpose is to describe arterial tissue. There are two models developed more specifically for bridging veins, one was developed by Rezakhaniha and Stergiopulos [47], and the other one by Nierenberger *et al.* [48].

Viscoelasticity

Many biological soft tissues have visco-elastic properties [49], which means that the mechanical properties of the material change with the strain rate.

Only in the first tests, conducted by Löwenhielm [50] and Gennarelli and Thibault [11] was stated that exists a strain rate dependency. However, all later studies, even conducted by Löwenhielm [51], rejected the strain rate dependency. Hence, it is likely that no viscoelastic effects need to be captured in the material model [21].

2.2 Head injuries

Head injuries include both injuries to the skull and the brain, they can be classified as closed and open. A closed head injury, is a brain injury that does not open up the brain or skull, whereas a open head injury occur when something hits the head forcefully to penetrate the skull [19]. The two major head fractures are: facial fracture and skull fracture. However, head fractures are not relevant to the topics discussed in this work, therefore they will not be explained in detail. As far as the brain is concerned the injuries can be devided in focal and diffuse.

2.2.1 Focal brain injury

Focal brain injury is an injury concentrated in one region of the brain, resulting from direct mechanical forces. The more common focal brain injuries are the following:

Epidural hematoma (EDH):

Epidural hematoma (left side of Figure 2.10) is when bleeding occurs in the epidural space, between the skull and dura mater. The cause of EDH is typically a skull fracture, but can also be the result of an arterial laceration. This kind of hematoma are often caused by accelaration/decelaration trauma and transverse forces.

EDH is not the most common traumatic brain injury, with only 0.2%-6% and 1.2%-1.7% changes to occur, according to Cooper [54] and Oehmichen *et al.* [55]. This hematona is less dangerous in life-threatening situations than the subdural hematoma.

Subdural hematoma (SDH):

A subdural hematoma (right side of Figure 2.10) is a severe injury and potencially life-threatening, that occurs when a blood vessel, such as a bridging vein rupture. SDH are caused by tangential forces against the skull, creating a rotational movement between the skull and brain [56], which leads to traction efforts on the blood vessels.

According to Sahuquillo-Barris *et al.* [57], a SDH is a result of an impact of short duration with high tension load.

There are three types of SDH: acute (one third of all subdural hematomas), subacute and chronic. The main difference between the three types of SDH is the speed of their onset, the acute subdural hematoma develops before the other two. The ASDH is generally caused by high-speed acceleration or deceleration, being the most deadliest.

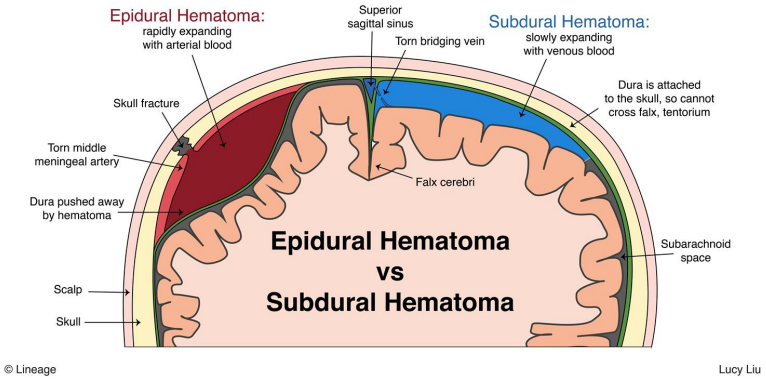

Figure 2.10: Illustration of the subdural heamatoma (right side) and epidural hematoma (left side). Adapted from Lineage Medical, Inc [58].

Intracerebral hematomas:

The intracerebral hematoma generally occurs in the deep tissue of the brain and ventricles, is usually caused by rupture of tiny arteries within the brain tissue. This injury is normally associated with sudden acceleration/decelaration of the head, or the rise of blood pressure.

Contusion:

Contusion is the most common injury resulting from head impact, that causes a localized bruise in the brain.

There are two types of contusion, coup and contre-coup. In the coup contusions, the brain is injured on the area where the hit occured, whereas in the contre-coup contusion the injury is on the opposite side where the hit was. Contre-coup injuries are more common to occur than coup contusions [59].

2.2.2 Diffuse brain injury

Unlike focal injuries, diffuse brain injuties (DBI) occur over a more widespread area, being associated with full rupture of the brain tissue. This type of injury, is usually caused by accelaration/deceleration of the head, as well as rotational forces. DBI account for proximally 40% of all severe brain injuries, and one third of deads due to head injuries [60].

The two major types of diffuse brain injury are the following:

2.2.2.1 Concussion

A concussion occurs when a blow to the head causes physical trauma to the brain, affecting the brain function, leading to the loss of concentration, memory, balance and coordination. This injury is usually caused by a blow to the head, very common in contact sports, such as football and boxing.

Nearly 2 million people are affected each year [19], and most make a full recovery. The time of recovery is fast, normally within 10 days the symptoms dissapear, but some people suffer from post-concussion syndrome, such as headaches, changes in mood, changes in vision, light and noise sensitivity and insomnia.

2.2.2.2 Diffuse anoxal injury

Diffuse anoxal injury (DAI) (Figure 2.11) describes an injury that causes widespread axonal damage, motivated by the stretch of an axon or the complete axotomy. Stretch injuries in the axons are considered to be a greater contributor for the occurance of DAI than injuries with complete axotomy.

Myelinction increases the dinamic modulus of white mater axons, making them more stiffer, and therefore less susceptible to shear stress than gray mater. However white mater axons are longer and therefore more prone to damage [61; 62].

The areas more commonly affected by this pathology include, axons in the brainstem, parasagittal white mater near the cerebral cortex, and corpus callosum. According to Oehmichen *et al.* [55], DAI is caused by acceleration/deceleration rotational or translational forces, which was expected since diffuse injuries usually are caused by this type of mechanical forces. Another important factor to consider, is the duration of the impact, since longer duration of force application increases the amount of energy transferred to the brain, causing more damage [63].

According to Meythaler *et al.* [64], DAI accounts for 40% to 50% of all traumatic brain injuries requiring hospital admission in the United States. Studies reveal that after one month follwing the injury, 55% of the pacients died, 3% were in vegetative state, and 9% had a severe disability [59; 65; 66].

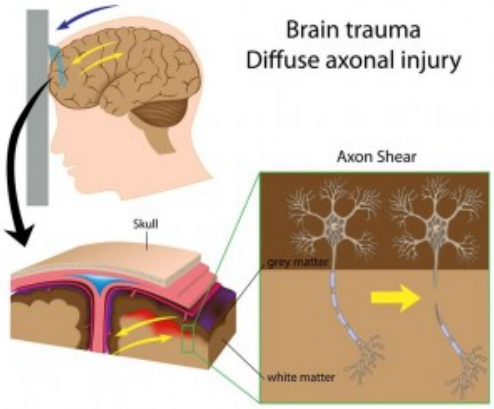

Figure 2.11: Illustration of the diffuse axonal injury. Adapted from Accident Attorneys [67].

2.3 The biomechanics and mechanisms of head injuries

Head injury usually results from a direct impact to the head or indirect impact (an impulse transmitted to the head through the neck) applied to the head-neck system. If the impact is indirect, that means that either the head or the torso were abruptly accelerated or decelerated. The impact and the impulse can both accelerate or decelerate a stationary head, but in the case of an impact it can also produce skull deformations or fracture, and consequently brain injuries. Table 2.4, shows the peak forces for different parts of the skull. However, injuries to the human brain are typically result of direct contact, instead of an impulse transmitted to the head-neck system [68; 69].

Some authors, state that the type of brain injury depends on the kinematic relationship between the impactor and the head [70]. This distinction is very important in forensic science, since is relevant in crime scenes to understand if the head injury sustained by the victim, was caused by a blow to the head or result of a fall [71]. However, if the impact velocity and the characteristics of the impactor are the same, there is no difference in the forces involved in a stationary head being stroke or a moving head hitting an object at rest.

Table 2.4: Peak force for fracture at different regions of the skull.

Impact area	**Force** (kN)	**Reference**
Frontal	4.0	[72]
	4.2	[73]
	4.3-4.5	[74]
	4.7	[75]
	5.5	[76]
	6.2	[77]
	15.6	[78]
Temporal	2.0	[72]
	3.4-4.4	[74]
	3.6	[73]
	5.2	[79]
	6.2	[78]
Occipital	11.7-11.9	[74]
	12.5	[80]
Parietal	3.5	[81]
Vertex	3.5	[74]

2.3.1 Linear and angular acceleration

For a given head impact, if the force vector passes through the centre of gravity of the head then it will be subjected to a linear acceleration. On the other hand, if the force vector does not passes through the centre of gravity, both linear and angular acceleration will be present.

If the human head was spherical, an impact perpendicular to the surface of the head, would always cause linear acceleration, because the force vector would be aligned with the center of gravity. However, the head has a complex geometry and can not be considered

spherical, then it is more likely to observe linear and angular acceleration [71]. Some authors, report that for impacts with the same characteristics, the angular acceleration is more likely to be higher in lateral impacts then in frontal or occipital impacts.

The first studies related to the biomechanics of head injury, assumed that the severity of the brain injury was associated with the presence of skull fracture. However, following studies quickly understand that was not just about the skull fracture, but all the head response to the impact, that determined the severity of the brain injury [71].

Holbourn [82], was one of the first researchers to state that, rotational motion of the head is the major cause of brain injury. To illustrate the Houlbourn's hypothesis, is normally used the bowl of porridge analogy (Figure 2.12). If the bowl is suddenly moved sideways, recreating a linear acceleration, there will be no appearance of relative motion in the porridge. However, if the bowl is rotated abruptly, the part of the porridge on the edge of the bowl will tend to move, while the porridge in the center will tend to remain stationary, causing shear stress.

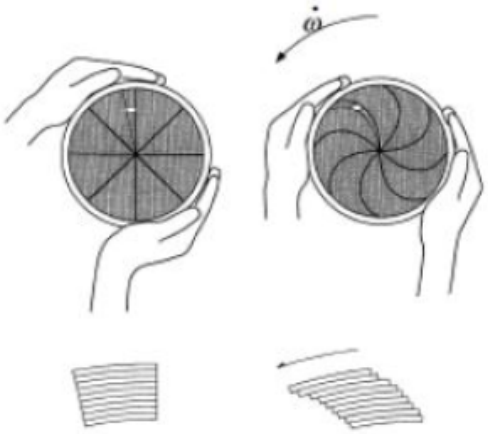

Figure 2.12: Illustration of the bowl of porridge analogy, utilized to explain the Houlbourn's hypothesis. Adapted from McLean and Anderson [71].

Using a model of the human head, Holbourn tested his hypothesis. He observed that, the strains caused by angular acceleration could be demonstrated, while in the case of linear acceleration the model was relatively insensitive. He also observed that, for short duration impacts, the duration of application of the force played an important role in the production of shear strains, whereas for long impacts, the shear strains were independent of the time for which the force acts. At least, he observed that, if there is a deformable object between the head and the impactor, the duration of the impact is extended, reducing the average level of the force transmitted to the head [83].

According to Ommaya and Gennarelli [84], linear acceleration in the sagittal plane is associated with focal lesions, whereas concussion, which is a diffuse injury, is associated with angular acceleration. A few years later, in a work by Gennarelli *et al.* [65], was concluded that axonal injury in the brain is proportional with the degree of coronal motion caused by the angular acceleration. Translational acceleration is associated with intracranial pressure, while rotational acceleration is associated with diffuse brain

injuries.

In resume, many authors agree that rotational forces, by tearing brain tissue and bridging veins, can cause almost every type of head injury, except skull fractures and EDH [10].

The Wayne State Tolerance Curve (WSTC), developed by Gurdjian and co-workers [85; 86], was one of the first head injury tolerance criteria. It was developed based only on direct frontal impacts, which makes the criteria invalid for non-contact situations or to other impact directions. Basically, the criteria states that, every point below the curve shown in Figure 2.13 is unlikely to be associated with severe brain injury.

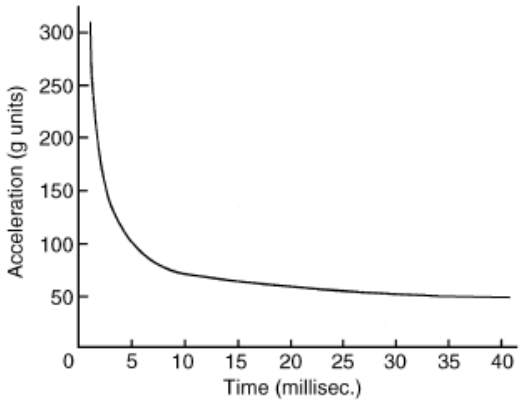

Figure 2.13: The Wayne State tolerance curve. Adatped from McLean and Roberts [71].

Figure 2.14, shows the relation between the angular acceleration and pulse duration for different types of injury. This curves are based in the Wayne state tolerance curve.

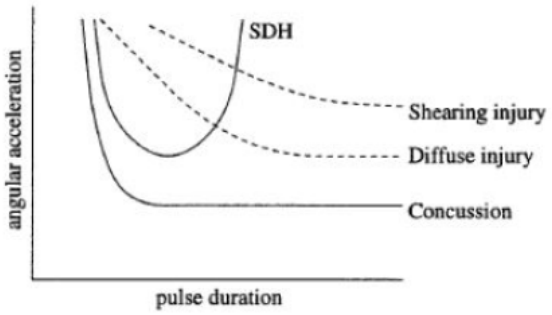

Figure 2.14: Angular acceleration vs pulse duration for different types of injury. Adatped from Wismans [87].

2.3.2 Tolerance criteria and thresholds

Tolerance criteria is a very important field in head injury understanding, because it is necessary to set thresholds to know if an impact will induce a force or accelerations higher

than the head can bear, evaluating the risk of sustaining a head injury, and to study the effectiveness of protective gear.

According to van den Bosch [88], the injury criteria can be divided in three categories: injury criteria only based on translational acceleration of the head's centre of gravity, injury criteria based on both translational and rotational acceleration, and injury criteria based on stresses and strains in the brain tissue.

In order to understand some criteria and thresholds that will be presented later in this work, it is necessary to know the Abbreviated Injury Scale (AIS). This scale, shown in Table 2.5, tries to catalog the severity of head injuries.

2.3.2.1 Criteria based on translational acceleration

The criteria showned below are all based in the assumption that linear acceleration alone is enough to predict head injury, thus ignoring the angular acceleration.

Peak linear acceleration (PLA)

The peak linear acceleration is the maximum value of linear acceleration that the head can bear, and the risk of sustaining an injury associated with it. This criterion in almost all cases does not take in consideration the time duration. The Table 2.6, shows the thresholds of the peak linear acceleration criterion.

Head injury criterion (HIC)

Head injury criterion is the most applied criterion, and was proposed by the National Highway Traffic Safety Administration, as the new criterion to predict, by finding the maximum of the equation, the most damaging part of the acceleration pulse. The Δt_{max} in the HIC equation corresponds to the time interval with the maximum variation of acceleration.

$$HIC_{\Delta t_{max}} = \left[\left(\frac{1}{t_2 - t_1} \int_{t1}^{t2} a(t)dt \right)^{2.5} (t_2 - t_1) \right]_{max} \tag{2.14}$$

where,

- $a(t)$, is the resultant head acceleration
- t_2 and t_1, are the final and initial time of the interval ($t_2 - t_1 \leq \Delta t_{max}$)

This criterion, results from the evolution of the WSTC, and is based on the assumption that linear acceleration and pulse duration are enough to predict the thresholds. However, many authors discredit this criterion, becasuse does not take in consideration angular acceleration, impact force and direction, which were proved to be major factors in head injuries. Nevertheless, HIC continues to be widely used, and is a useful predictor for comparing energy-absorting safety devices [10].

In Table 2.7, are shown the thresholds based on HIC for different head injuries, and Figure 2.15 correlates the HIC criterion with the probability of sustaining a head injury.

Table 2.5: Abbreviated Injury Scale. Adapted from Hayes *et al.* [89].

AIS level	**Injury description**	**Mortality rate** (%)
1	Minor	0.0
2	Moderate	0.1-0.4
3	Serious	0.8-2.1
4	Severe	7.9-10.6
5	Critical	53.1-58.4
6	Non-survivable	-

Table 2.6: PLA thresholds.

Injury	**Tolerance**	**Reference**
Head injury	a = 80 g for 3 ms	[90; 91; 92]
	50 % Probability:	[93]
	AIS 2+: 116 g	
	AIS 3+: 162 g	
	AIS 4: 200-250 g	[94]
	AIS 5: 250-300 g	
	AIS 6: >300 g	
Skull fracture	5% Risk a = 180 g	[95]
	40% Risk a = 250 g	
	50% Risk a = 135 g	[93]
MTBI	25% Probability: a = 559 m/s^2	[96]
	50% Probability: a = 778 m/s^2	
	75% Probability: a = 965 m/s^2	
	50% Probability: a = 762 m/s^2	[97]
	95% Probability: a = 1131 m/s^2	
	85 g for an impact	[98]
	duration $10 \leqslant t \leqslant 30$ ms	
Concussion	a = 81 g	[99]
	60.51-168.71 g	[100]
	105±27 g	[101]
	74±21 g	[102]
	50% Probability: a = 65.1 g	[103]
	75% Probability: a = 88.5 g	

Table 2.7: HIC thresholds.

Injury	Tolerance	Reference
Head injury	Severe but not life-threatening 1000	[104]
	8.5% Probability of death: 1000	[105]
	31% Probability of death: 2000	
	65% Probability of death: 4000	
	16% Probability of death: life-threatening 1000	[106]
	99% Probability of life-threatening injuries: 3000	
	50% Probability of AIS 2+: 825	[93]
	50% Probability of AIS 3+: 1442	
MTBI	25% Probability for (HIC_{15}) 136	[96]
	50% Probability for (HIC_{15}) 235	
	75% Probability for (HIC_{15}) 333	
	50% Probability for (HIC_{15}) 240	[97]
	95% Probability for (HIC_{15}) 485	[98]
	240	
Skull fracture	50% Risk: 667	[107]
SDH	50% Risk: 1429	[107]
Moderate neurological injury	50% Risk: 533	[107]
Severe neurological injury	50% Risk: 1032	[107]
Concussion	200	[99]

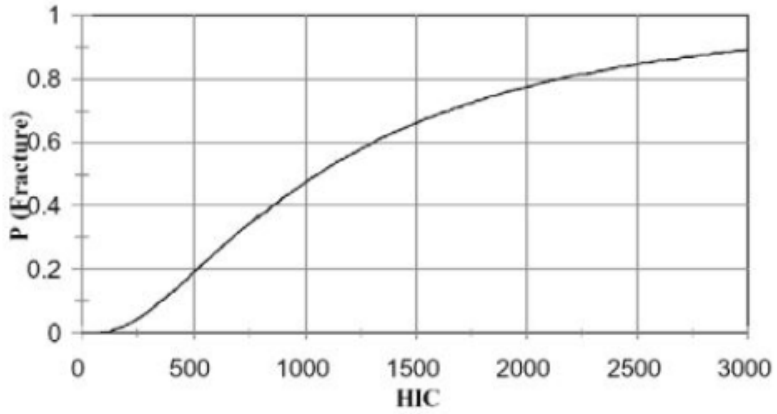

Figure 2.15: Probability of sustaining a head injury according to the HIC criterion. Adatped from Hertz [108].

2.3.2.2 Criteria based on translational and rotational acceleration

The angular acceleration is considered by many authors a very important factor in head injuries, alongside with the linear acceleration. Some studies have tried to relate the angular acceleration with the severity of the injury, Gennarelli *et al.* (2003) [109], presented the values shown in Table 2.8, that catalogs the injuty severity for diffuse brain injuries according to the angular acceleration and angular velocity. Table 2.9, presents several thresholds for different angular acceleration and velocity.

Table 2.8: Categories of DBI severity according to angular acceleration and velocity.

AIS Level	**Injury severity**	**Angular acceleration** (rad/s^2)	**Angular velocity** (rad/s)
1	Mild cerebral concussion	2877.8	25
2	Classical cerebral concussion	5755.6	50
3	Severe cerebral concussion	8633.4	75
4	Mild DAI	11511.2	100
5	Moderate DAI	14389	125
6	Severe DAI	17266.8	150

Table 2.9: Human brain tolerance to rotational acceleration and velocity.

Injury	Threshold	Reference
Brain surface shearing	α = 2000-3000 rad/s^2	[80]
Bridging vein rupture	α = 4500 rad/s^2 or ω = 50-70 rad/s	[51; 110]
	α = 5000 rad/s^2 or ω = 50 rad/s	[111]
	α = 10 $krad/s^2$ or t <10 ms	[13]
Concussion	50% Probability:	[112; 113]
	α = 1800 rad/s^2 for t <20 ms	
	ω = 30 for t $\geqslant$ 20 ms	
	99% Probability:	
	α >7500 for t >6.5 ms	
	α = 14000 rad/s^2 for 11 ms	[114]
	α = 13000 rad/s^2 for 11 ms	[115]
	α = 20 $krad/s^2$ for 18 ms	[11]
	α = 13600-16000 rad/s^2 and ω = 25-48 rad/s	[116]
	α = 18 $krad/s^2$ for 18 ms	[117]
	50% Probability: α = 6200 rad/s^2	[118]
	50% Probability: α = 6322 rad/s^2	[97]
	50% Probability: α = 9267 rad/s^2	[97]
	α = 6400 rad/s^2 and ω = 35 rad/s	[119]
	α = 6200 rad/s^2	[120]
	α = 7600 rad/s^2 for 15 ms	[121]
	α = 7300 rad/s^2 for 23 ms	
	α = 1800 rad/s^2	[122]
	α = 6432 rad/s^2	[123]
	α = 5022 rad/s^2	[124]
	α = 5582.3 rad/s^2	[125]
	50% Probability: α = 1747 rad/s^2	[103]
	75% Probability: α = 2296 rad/s^2	(coronal plane)
	α = 7912 rad/s^2	[99]
	α= 5312 rad/s^2	[100]
	α = 5025 rad/s^2	[102]
	50% Probability: α = 1747 rad/s^2	[126]
DAI	α = 20 $krad/s^2$ for 18 ms	[11]
	α = 19 $krad/s^2$ for 20 ms	[127]
	α = 10000 rad/s^2 and ω = 100 rad/s	[128]
	α = 18000 rad/s^2	[129]
	α = 8000 rad/s^2 or ω = 70 rad/s	[130]
Mild DAI	α = 12500-15500 rad/s^2	[122]
SDH	α = 32 $krad/s^2$ for 14 ms	[131]
	α = 10000 rad/s^2	[130]
	α = 10000 rad/s^2 for t >4 ms or ω = 19 rad/s	[11]
TBI	α = 1700 rad/s^2 and ω = 60-70 rad/s	[132]
	ω <30 rad/s and α <4500 rad/s^2:safe	[12]
	ω <30 rad/s and α >4500 rad/s^2: AIS 5	[133]
	ω >30 rad/s and α = 1700 rad/s^2: AIS 2	[134]
	ω >30 rad/s and α >3000 rad/s^2: AIS 3	
	ω >30 rad/s and α >3900 rad/s^2: AIS 4	
	ω >30 rad/s and α >4500 rad/s^2: AIS 5	
	α = 25000 rad/s^2 for short durations	[135]
	α >5000 rad/s^2	[136]
	4500 rad/s^2 <α <5000 rad/s^2 and ω = 60 rad/s	[104]
MTBI	25% Probability: α = 4384 rad/s^2	[96]
	50% Probability: α = 5757 rad/s^2	
	75% Probability: α = 7130 rad/s^2	
	α = 6000 rad/s^2 for 10 <t <30 ms	[98]
	25% Probability: α = 4600 rad/s^2	
	50% Probability: α = 5900 rad/s^2	
	80% Probability: α = 7900 rad/s^2	
Head injury	50% Probability:	[93]
	AIS 2+: ω = 40 rad/s and α = 11368 rad/s^2	
	AIS 3+: ω = 55 rad/s and α = 18755 rad/s^2	

Generalized acceleration model for brain injury threshold (GAMBIT)

The head injuty criterion GAMBIT developed by Newman [94], takes into account both translational and rotational acceleration, and its given by the expression 2.15. Some values and thresholds are presented in Table 2.10 and 2.11, respectively. However, the GAMBIT is not much used nowadays, due to the fact that was never extensively validated and lacks pulse duration dependency.

$$G(t) = \left[\left(\frac{a(t)}{a_c}^n\right) + \left(\frac{\alpha(t)}{\alpha_c}^m\right)\right]^{1/s} \tag{2.15}$$

where,

- $a(t)$ and $\alpha(t)$, are the instantaneous values of the linear and angular acceleration
- n, m and s, are empirical constants
- a_c and α_c, are critical tolerance levels for the linear and agular acceleration.

Table 2.10: GAMBIT values.

n	m	s	a_c(g)	$a_c(rad/s^2)$	Reference
2	2	2	250	25000	[94]
2	2	2	250	10000	[137; 138]

Table 2.11: GAMBIT thresholds.

Injury	**Threshold**	**Reference**
Head injury	50% Probability of AIS >3:	[97]
	G = 1	
	$1.5 \leqslant G \leqslant 2$	[137]
Concussion	50% Probability:	[97]
	$G \geqslant 0.4$	
	95% Probability:	
	$G \geqslant 0.56$	

Head injury power (HIP)

Newman *et al.* [118], proposed the HIP criterion, which takes in consideration the translational and rotational kinetic energy chage rate, calculating the sum of the power along each dregee of freedom of the head. The HIP value is expressed in Watts, and the mathematical expression, which is divided in two parts the first for the linear acceleration and the second for the angular acceleration, is the following:

$$\begin{aligned} HIP = Ma_x \int a_x dt + Ma_y \int a_y dt + Ma_z \int a_z dt \\ + I_{xx}\alpha_x \int \alpha_x dt + I_{yy}\alpha_y \int \alpha_y dt + I_{zz}\alpha_z \int \alpha_z dt \end{aligned} \tag{2.16}$$

where,

- m is the mass of the human head
- I_{xx}, I_{yy}, and I_{zz}, represent the moments of inertia for the human head in the three directions (x,y and z).

Table 2.12, presents thresholds for different head injuries according to HIP criterion, however HIP_{max} was only validated for mild traumatic brain injury, and not for severe brain injuries.

Table 2.12: HIP thresholds.

Injury	Threshold	Reference
Skull fracture	50% Probability: HIP_{max} = 38 kW	[107]
SDH	50% Probability: HIP_{max} = 55 kW	
Moderate neurological injury	50% Probability: HIP_{max} = 24 kW	
Severe neurological injury	50% Probability: HIP_{max} = 48 kW	
Concussion	50% Probability: HIP_{max} = 12.8 kW 95% Probability: HIP_{max} = 20.88 kW	[97]

Power index (PI)

The Power index (PI), was proposed by Kleiven [139], is an upgrade of the HIP, by adding scaling coefficients to the various directions and differentiating between positive and negative accelerations [21]. The empirical expression is shown in equation 2.17.

$$\begin{aligned} PI = &[C_1^+\theta(a_x) + C_1^-\theta(-a_x)]ma_x \int a_x dt + C_2 ma_y \int a_y dt \\ &+[C_3^+\theta(a_z) + C_3^-\theta(-a_z)]ma_z \int a_z dt + C_4 I_{xx}\alpha_x \int \alpha_x dt \\ &+[C_5^+\theta(\alpha_y) + C_5^-\theta(-\alpha_y)]I_{yy}\alpha_y \int \alpha_y dt + C_6 I_{zz}\alpha_z \int \alpha_z dt \end{aligned} \tag{2.17}$$

with,

$$f(x) = \begin{cases} 1, & a > 0 \\ 0, & a < 0 \end{cases}$$

2.3.2.3 Criteria based on stresses and strains

Criteria based on stress and strain, are commonly used for researches rather than criteria based on kinematics, such as linear and angular acceleration. The problem associated with criteria based on stress and strain, is the fact that these parameters are difficult to measure inside the brain [88]. To counter this setback, detailed and accurate FEHM are used.

There are five major criteria based on stress and strain, they are: the brain pressure tolerance, the brain von Mises stress, the cumulative strain damage measure criteria (CSDM), the dilatation damage measure (DDM) and the relative motion damage measure (RMDM). The last three were developed by DiMasi *el al.* [140] and Bandak [141; 142].

In Table 2.13 and 2.14, are some thresholds for different head injuries, according to the brain pressure tolerance and the brain von Mises stress, respectively.

Table 2.13: Brain pressure criterion thresholds.

Brain injury	**Brain pressure** (kPa)	**Reference**
Moderate	172.3	[143]
Severe or fatal	234.4	
Minor or absent	$\leqslant$ 173	[144]
Severe	$\geqslant$ 235	
Brain injuries (brain contusions, oedema and hematoma)	200	[145; 146; 147]
Brain injury by coup pressure	180	[148]
	256	[149]

Table 2.14: Brain von Mises stress thresholds.

Brain injury	**von Mises stress** (kPa)	**Reference**
Brain injury	12	[148]
	14.8	[149]
Severe brain injury	11-16.5	[150]
	27	[151]
Concussion	22	[147]
	20	[152]
	40	[153]
Long duration concussion	20	[137]
Short duration concussion	10	
Severe neurological injury	46	[154]
50% Moderate neurological injury	18	[155; 156]
50% Severe neurological injury	38	
50% Mild DAI	26	[157]
50% Severe DAI	33	
50% Probability of concussion	8.4 in corpus callosum	[45]
Severe and irreversible TBI	14.8$\pm$4.5	[149]

2.4 Finite element human head models

A finite element human head model (FEHM), when properly validated, can be a very powerful tool to simulate head injuries under impact conditions and to compute variables such as stress and strain. The reason why they are such a valuable tool, is because obtaining values from living humans is not ethical, and can lead to serious injuries for the subject. Another possibility is to obtain data from human cadavers or animals, however the mechanical properties of dead human tissue and animal tissue differs from living human tissue, which can lead to inaccurate results. Nevertheless, the impact experiments conducted on human cadavers by Nahum *et al.* [143] and by Depreitere *et al.* [12], are used as reference to validate FEHMs. Human dummies such as Hybrids, SIDs, BioRID, CRABI and THOR are yet another possibility, however replacing dummy parts after experiments leads to high costs [2].

The first finite element head model to be developed, was a very simplistic two-dimensional skull model by Hardy and Marcal [158], which was later improved by Shugar [159] by adding an elastic fluid-filled brain assumed to be firmly attached to the skull [2]. However, both version presented unrealistic results for large deformation simulation.

The first three-dimensional FEHMs appeared in the late 70s and had a simplified geometry, examples are: Chan [160] that modeled the human head as a spherical shell and a prolate ellipsoid, Khalil and Hubbard [161] that used an ellipsoid shell for the skull and an inviscid fluid core as the intracranial content, and Hosey and Liu [162] that modeled both head and neck. However, only in the 90s with the advance of computational power appeared the more realistic 3D models, examples are: Horgan and Gilchrist [163]; Kleiven [45], Mao *et al.* [164], Ruan *et al.* [165], Sahoo *et al.* [166], Takhounts *et al.* [167], Yang [168] and Zhang *et al.* [169].

Most of the 3D models mencioned above have a geometry similar to spheroidal/ ellipsoidal structures, not taking into account the gyri and sulci. Some authors, studied the influence of gyri and sulci on head injuries. Cloots *et al.* [170], using a 2D FE model, reported that gyri and sulci had a significant effect on von Mises stress maximum value, whereas Ho and Kleiven [171], reported that sulci played an important role on reducing the stress and strain rates, especially for angular accelerations in the sagittal plane. Another important aspect that most of the 3D models created do not take into account, is the relative motion between the skull and brain, which is a significant factor in some brain injuries, because the excessive relative motion may injure the brain surface and stretch or even tear bridging veins.

Next, it will be provided a short state-of-the-art review of some finite element head models.

UDS FEHM:

The UDS FE head model was developed by University of Strasbourg, and took into consideration the bridging veins, they were represented as the width of the CSF, in other words, the distance between the inner surface of the skull and the outer surface of the brain. However, BVs were not represented mechanically, not contributing for the stiffness of the FE model, but their strain could be computed [21].

ULP FEHM:

The ULP FE model, shown in Figure 2.16, was developed by University of Louis Pasteur and includes the skull, brain, falx, tentorium, CSF, and scalp. It is important to mention that the model has been improved over the years. The CSF was changed from an elastic material model to a Lagrangian formulation and was introduced an elastic-brittle constitutive law for the skull-brain interface. Except for the brain, which has viscoelastic properties, all the other parts of the model has homogeneous and isotropic material properties. [2]

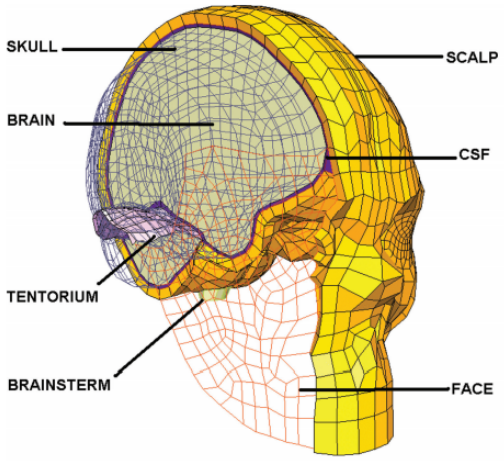

Figure 2.16: ULP finite element head model. Adapted from Deck and Willinger [157].

Shugar model:

The Shugar model was developed by Shugar [172], and included a coarsely meshed three-layered skull, the falx, tentorium, foramen magnum and brain [21]. This model was updated by Huang [173], in order to account for bridging veins deformation. He used a similar approach to the UDS model, using the space between the skull and brain to represent the BVs, instead of a tied connection.

SIMon FEHM:

The simulated injury monitor (SIMon) model was created by Takhounts *et al.* [167], and includes the cerebrum, cerebellum, falx, tentorium, combined pia-arachnoid complex with CSF, ventricles, brainstem and bridging veins. In this model the BVs were modeled as cable discrete beams with Young's modulus of 0.275 MPa [21].

KTH FEHM:

The Kungliga Tekniska Högskola (KTH) model shown in Figure 2.17, was developed by Kleiven [45; 139; 174; 175] and includes the scalp, skull, meninges, CSF, cerebrum, cerebellum, brainstem, transverse ans superior sagittal sinus, a simplified neck with spinal cord and 11 pairs of bridging veins. The BVs in this model were represented by discrete beam elements with a stiffness of 1.9 N per unit strain, conecting a node on the cortical surface of the brain to a node on the SSS.

UCDBTM:

The UCDBTM model, shown in Figure 2.18, was presented in Horgan and Glichrist [163], and includes the skull, CSF, cerebrum, cerebellum, brainstem, scalp, falx, tentorium, dura and pia mater, and 11 pairs of bridging veins modeled in a very similar way as in the KTH model [21].

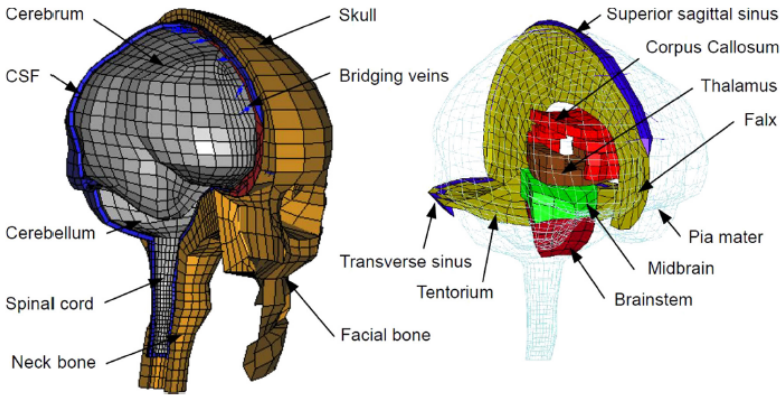

Figure 2.17: KTH finite element head model developed by Kleiven [45]. Adapted from Famaey *et al.* [21].

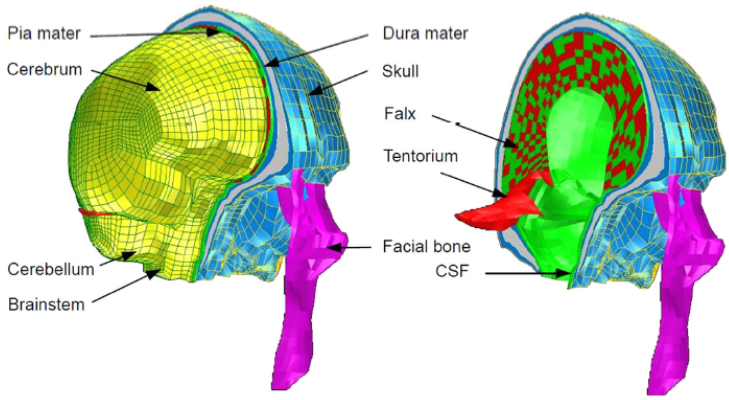

Figure 2.18: UCDBTM finite element head model. Adapted from Famaey *et al.* [21].

WSUBIM:

The Waye State University Brain Injury Model has been improved over the years, the first version was developed by Ruan *et al* [165] and then was improved by Zhou *et al.* [176], being later on updated and used by Zhang *et al.* [169; 177] and Viano *et al.* [119]. This updated version contained the scalp, skull, dura, falx, cerebri, tentorium, pia, CSF, venous sinuses, ventricles, cerebrum (grey matter and white matter), cerebellum, brainstem, and ten pairs of bridging veins [21] shown in Figure 2.19. The bridging veins in this model were represented by linear elastic spring elements with a spring constant of 0.219 N/mm [21].

The most recent FE head model to be developed at Wayne State University was by Mao *et al.* [164]. Based on CT an MRI images, contains hexahedral meshes of the brain (cerebrum, cerebellum, brainstem, corpus callosum, ventricles, and thalamus), as well as 11 pairs of bridging veins, CSF, skull, facial bones, flesh, skin, falx, tentorium, pia, arachnoid, and dura. The 11 pairs of BVs were modeled using beam elements, with lengths ranging from 6.63 to 17.91 mm, outter diameter of 2.76 mm and a wall thickness of 0.03 [21].

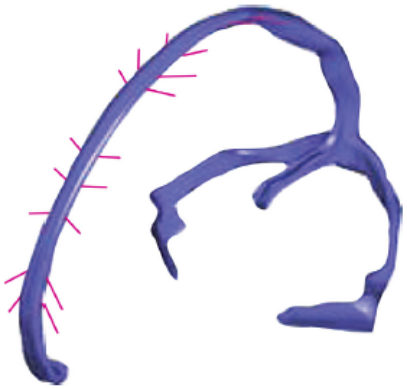

Figure 2.19: Superior sagittal sinus and bridging veins model in the WSUBIM. Adapted from Viano *et al.* [119].

Yet another head model (YEAHM):

The YEAHM was developed by Fernandes *et al.* [15]. This model differs from the others mencioned above, mainly because it includes giry and sulci [15], which plays an important role in von Mises stress maximum value, and on reducing the stress and strain rates, especially for angular accelerations in the saggital plane. The YEAHM also takes into account the relative motion between the skull and brain, unlike many of the head models developed. This relative motion is determinant, since may lead to head injuries by damaging brain's surface and stretch or even tear bridging veins.

The geometry of this model was developed based on medical images, computed tomography (CT) was used to generate the skull, while Magnetic resonance imaging (MRI) was used to model the brain [178]. Figure 2.20, shows the modeling process of the YEAHM. The first step, was to obtain the STL model through the medical images, then the STL

meshes were imported into a CAD software, in order to create the 3D solid models of the skull, brain and CSF. The last step, was to import the 3D solid models into a finite element software.

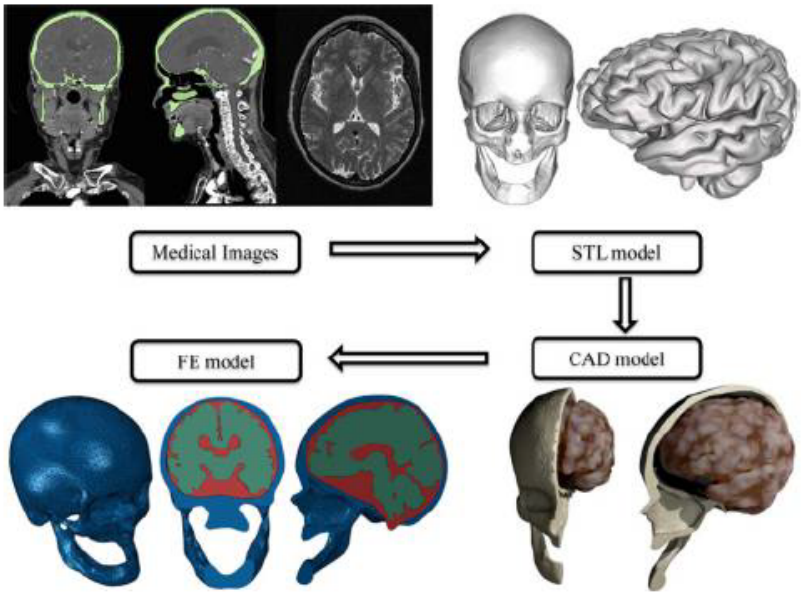

Figure 2.20: YEAHM modeling process.

The YEAHM model is composed by the skull, brain and CSF, as shown in Figure 2.21. The brain has all the important sections: frontal, parietal, temporal and occipital lobes, cerebrum, cerebellum, corpus callosum, thalamus, midbrain and brainstem. The CSF represents all the area between the skull and brain, due to the fact that MRI images did not have enough resolution to separate the membranes and bridging veins from the cerebrospinal fluid [15].

Figure 2.21: YEAHM sections, consisting of skull, CSF and brain.

Material definition is probably the most important part on a finite element model,

because the accuracy of the model is highly related to the mechanical properties of the material. To model the brain, the Ogden hyperelastic model was used to describe the non-linear elasticty, and a viscoelastic model to describe the time-dependent behaviour [15]. In Table 2.15, are shown the values used to model the brain. The CSF was modeled as a hyperelastic material, using the Mooney-Rivlin strain energy density function, and as solid with low shear modulus, the values used are shown in Table 2.16. Another possibility was to assume the CSF a fluid, however according to Fernandes *et al.* [15], the computacional power needed was to excessive. Finally, the skull was modeled assuming a linear elastic and isotropic behaviour, the parameters can be seen in Table 2.17.

Table 2.15: Properties used to model the brain in YEAHM.

$\rho[kg/m^3]$	$\mu_1[MPa]$	α_1	$D_1[MPa^{-1}]$	g_1	g_2	$\tau_1[s]$	$\tau_2[s]$
1040	0.012	5.0507	0.04	0.5837	0.2387	0.02571	0.02570

Table 2.16: Properties used to model the CSF in YEAHM.

$\rho[kg/m^3]$	$C_{10}[MPa]$	$C_{01}[MPa]$	$D_1[MPa^{-1}]$
1000	0.9	1	0.9

Table 2.17: Properties used to model the skull in YEAHM.

$\rho[kg/m^3]$	$E[MPa]$	ν
1800	6000	0.21

The authors of the YEAHM model, decided to use C3D10M elements to mesh all the diferent components of the head (skull, CSF and brain). Given the complexity of the model geometry, the hexaedral elements were quickly excluded, mesh generation would have been extremely difficult. The other option, was to use the standard linear tetrahedral element (C3D4), however this element exhibits volumetric locking in case of almost incompressible materials, fact that was detected during the simulations [15]. For all the reasons mencioned above, C3D10M was used, this element is reported to exhibit almost no shear and volumetric locking and is robust during finite deformation [15].

As said before, many of the models already developed have tied connections between the skull and brain, which is not biofidelic. The YEAHM model, in order to allow motion between the brain and skull, uses finite sliding formulation and kinematic contact method, with a friction coefficient for tangential behaviour of 0.2, between the skull and CSF and between the CSF and brain, as proposed by Miller *et al.* [179].

Chapter 3

Bridging veins material and geometric modeling

3.1 Finite element analysis (FEA)

Finite element simulation of head impacts is generally treated as dynamic nonlinear problem. What dictates if a FEA is linear or nonlinear is the change of the stiffness matrix with time. For linear problems the stiffness matrix remains constant, whereas in nonlinear problems the stiffness matrix depends on the displacements, changing in each increment [180]. In the case of linear systems modal analysis is used, being based on the eigenmodes method, while in the case of nonlinear systems direct integration methods are used [181].

There are two main integration methods, the implicit formulation and the explicit formulation. The explicit scheme obtains the solution at time $t + \Delta t$ based entirely on the values at time t. On the other hand, the implicit scheme obtains the values of the variables at time $t + \Delta t$ not only based on the values of the variables at time t but also on the values at $t + \Delta t$ [181]. Both integration methods are incremental, however the implicit scheme has the need to use an iterative process, such as Newton-Raphson, to get to the solution. The use of an iterative process makes the implicit method spend more computacional resources than the explicit method, however the explicit scheme because it is conditionally stable leads to the need for smaller time increments, opposed to the implicit method that allows the use of higher time increments, which can lead to longer simulations. Nevertheless, implicit scheme calculates the global matrices of the complete system at each step, requiring more disk space and memory [180].

Thus, in conclusion the implicit method is more appropriate for static or low frequency problems while the explicit method is better for high speed impacts with short duration, which is the case for this work. Throughout this work is used the Explicit version of the FE package ABAQUS.

3.2 Material model

As described in Chapter 2, State-of-the-art review, bridging veins are considered to be nonlinear, anisotropic and prone to rupture. Biological tissue is often modeled using the hyperelastic constitutive model. However, due to its computacional simplicity, elastic-

plastic theory is still widely used to mechanically characterize biological tissue. For the reasons mencioned above, the elastic-plastic constitutive model is the one that is going to be used in this work, to describe the BVs.

3.2.1 Elastoplastic material

Elastic-plastic theory is simpler to characterize the BVs than hyperelastic theory, fewer parameters are required. Figure 3.1, shows a representation of a typical stress-strain curve for the elastoplastic material, that can be divided into three fases. The initial fase, is characterized by a toe region followed by a linear segment, which describes the elastic behaviour. The second fase, which describes the plastic regime, begins after the yield point ending when the rupture point is reached, starting the third fase where the bridging veins tear.

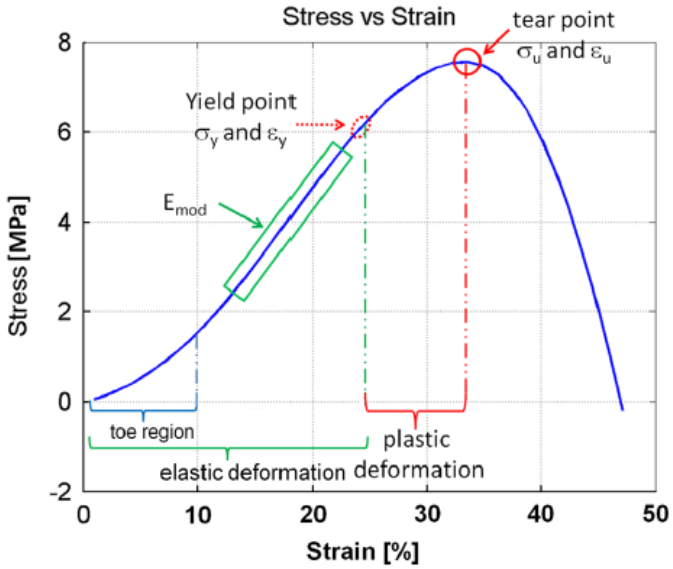

Figure 3.1: Typical stress-strain curve for a elastoplastic material. Adapted from Monea *et al.* [1].

In order to define the first part of the stress-strain curve, two parameters are necessary, the Young's modulus (E) and the Poisson's ratio (ν). The Young's modulus was chosen based on Table 2.3 of chapter 2, value reported by Monea *et al.* [1] after experiments conducted in human BVs. The value of the Poisson's ratio should be 0.5, because biological tissue can be considered an incompressible material. However, ABAQUS does not accept this value to avoid divisons by zero in stiffness matrix, for this reasons the value chosen was 0.45. Both, Young's modulus and Poisson's ratio can be seen in Table 3.1.

Table 3.1: Mechanical properties for the elastic regime.

Young's modulus [MPa]	Poisson's ratio
25.72	0.45

To define the plastic regime a stress-strain curve was chosen, from where the values of the stress and strain were collected. According to Monea *et al.* [1], the tear stress of the BVs is 4.19±2.37 (MPa), and the tear strain is 29.82±13.26 (%), as can be seen in Table 2.3. The curve that best met the requirementes mencioned above is the one pointed by the blue arrow in Figure 3.2, which was result of a mechanical stretch with a strain rate of 135.86 s^{-1} and an elongation velocity of 1358.55 mm/s. Using an online software [182], points of the curve were selected and then collected. Figure 3.3 shows in more detail the curve selected to use as experimental input in the material model validation.

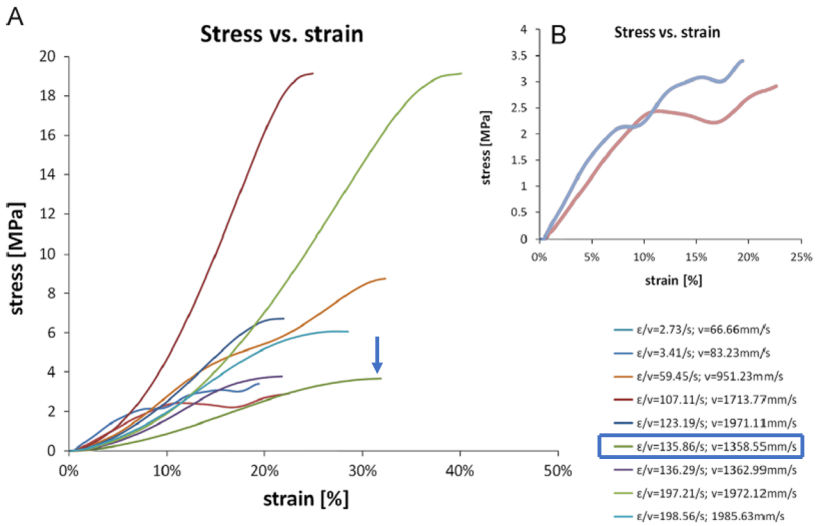

Figure 3.2: Stress-strain curves from experimental tests for different strain rates (A) and for low strain rates (B). Adapted from Monea *et al.* [1].

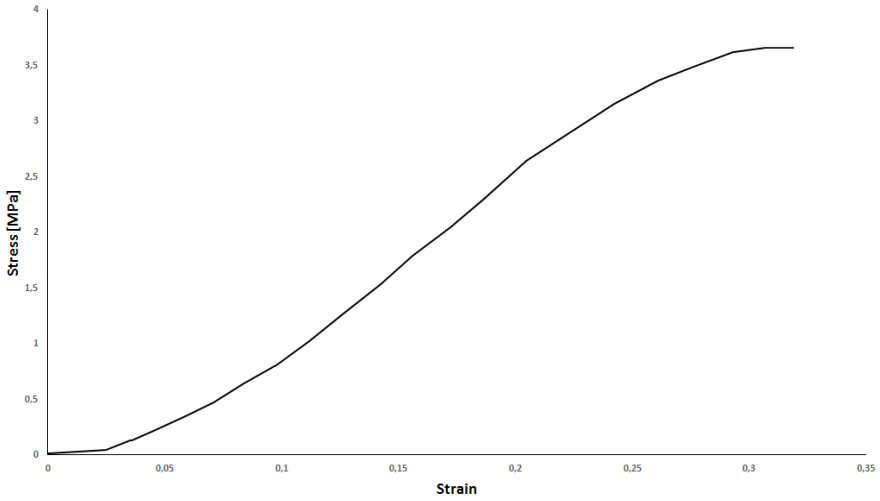

Figure 3.3: Experimental stress-strain curve used as experimental input for the material model validation.

In order to define the rupture point, from which the elements that exceed this value are eliminated during the simulation, it was necessary to implement a damage criterion. The chosen criterion was the ductile damage. This criterion is a phenomenological model that assumes that the equivalent strain ($\bar{\varepsilon}^{pl}_D$) at the onset of damage is a function of the stress triaxiality (η) and strain rate ($\dot{\bar{\varepsilon}}^{pl}$). The stress triaxiality is given by the following equation:

$$\eta = -p/q \tag{3.1}$$

where, p is the pressure stress and q the Mises equivalent stress.

The damage criterion is initiated when the following condition is satisfied:

$$\omega_D = \int \frac{d\bar{\varepsilon}^{pl}}{\bar{\varepsilon}^{pl}_D(\eta, \dot{\bar{\varepsilon}}^{pl})} = 1 \tag{3.2}$$

where, ω_D is a state variable that increases with the plastic deformation.

During the analysis each increment is given by the following condition:

$$\Delta\omega_D = \frac{\Delta\bar{\varepsilon}^{pl}}{\bar{\varepsilon}^{pl}_D(\eta, \dot{\bar{\varepsilon}}^{pl})} \geq 0 \tag{3.3}$$

The values of the four parameters necessary to define this criterion: fracture strain, strain rate, stress triaxiality and the displacement at failure are shown in Table 3.2. After the implementation of the damage criterion is expected that when the stress-strain curve of the element reaches the tear point the stress levels decrease, until get to zero.

Figure 3.4, shows the triaxiality curve reported by Migueis [14], the curve starts from the resting state and then increases until it stabilizes at the value of 0.33, increasing again after a while. This last increase happens when the material reaches the plastic regime. Thus, the value chosen for the triaxiality was 0.33.

Theoretically, the damage evolution parameter should be as close to zero as possible. Migueis [14], reported that a value of 0.05 is the one that best represents the mechanical behaviour of the bridging veins. For this reason, the value used for the damage evolution in this work, in order to validate the material model, was 0.05.

Table 3.2: Values used to define the damage evolution model.

Fracture strain	Stress triaxiality	Strain rate (s^{-1})	Displacement at fracture
0.31875	0.33	135.86	0.05

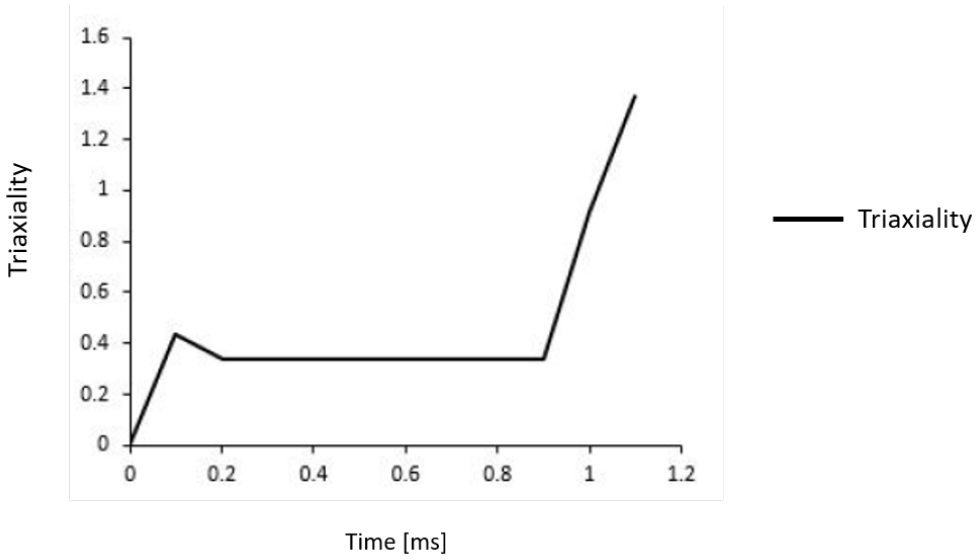

Figure 3.4: Triaxiality curve. Adapted from Migueis [14].

3.2.2 Material model validation

To validate the bridging veins material model, the mechanical test performed in Monea *et al.* [1] was recreated in Abaqus. To carry out this mechanical test they used a dynamic mechanical test machine (Figure 3.5 A), where they streched axially 110 BVs by applying a uniaxial displacement at various constant velocities between 254.02 mm/s and 2015.74 mm/s, and constant strain rate varying between 10.81 s^{-1} and 198.56 s^{-1}. The curves associated with each velocity and strain rate can be seen in Figure 3.2. It is important to mention that they used two laparoscopic surgical clamps, as shown in (Figure 3.5 B), to facilitate the fixation of the BVs to the test bench, reducing problems associated with slippage of the BVs [1]. To simulate the mechanical test, two approaches were used, one was to model the vein with solid elements and the other with shell elements. In both of them, the bridging vein was simplified to a cylindrical shape, with an outter diamter of 1.4 mm and thickness of 0.044 mm. However for the solid element the thickness was defined in the sketch, whereas in shell was defined at the section tab in the thickness parameter. Nevertheless, both were simulated with dynamic explicit analysis. After modeling the geometry, it was necessary to define the material, four conditions were used: density, to which the value given was 1130 kg/m^3, elastic regime, where two values were defined and can be seen in Table 3.1, plastic regime, defined by the curve shown in Figure 3.3, and the ductile damage criterion, being the values set according to Table 3.2. The next step was to define the boundary conditions, a velocity of 1358.55 mm/s was assigned to one end of the bridging vein, while the other end was fixed using the encastre BC. Finally, the mesh was assigned for the two approaches, being each one simulated with hexahedral and tetrahedral elements, in order to choose which element works best.

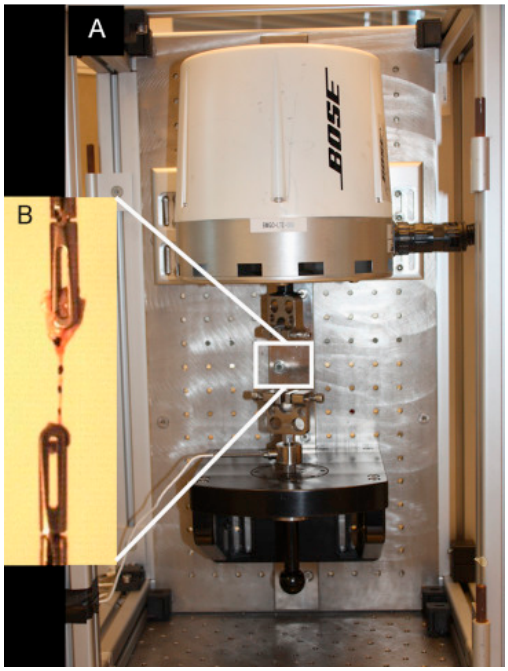

Figure 3.5: (A) Dynamic mechanical test machine used by Monea to carry out the uniaxial tensile tests on the BVs. (B) Close-up of a BV fixed with two laparoscopic surgical clamps. Adapted from Monea *et al.* [1].

Solid elements

The first step, as said before, it was to simulate with solid elements the mechanical test on the bridging vein. Figure 3.6, shows the stress-strain curves for the experimental test carried out by Monea *et al.* [1] and for the different types of solid elements.

The C3D4, a 4 node linear tetrahedron, had an unsatisfactory result since the tear strain was higher than expected, giving the material a similar behaviour to ductile materials such as steel and aluminum. The C3D10M, a 10 node modified second-order tetrahedron, had the same problem of the C3D4 element, but in addition the tear stress value also increased. Besides that the C3D10M element also increases the simulation time. The only element that had satisfactory results was the C3D8, a 8 node linear brick, however even this element was not perfect, due to the fact that the rupture point was a little bit below than expected, having a rupture strain of 0.2856. Figure 3.7, shows the initial and final state of the simulation with the C3D8 element.

Nevertheless, further in this work, it will be seen that the full geometry of the bridging veins and superior sagittal sinus has a very complex shape, which will make it almost impossible to use solid elements, being chosen another approach.

Shell elements

After the simulation with solid elements, were carried out simulations with three shell elements supported by the Abaqus explicit library. The three shell elements used were: the S4, a 4 node square, the S4R, a 4 node square with reduced integration and hourglass

control, and the S3R, a 3 node triangular element with reduced integration. By looking at the Figure 3.9, it can be seen that all three elements reproduced very accurately the stress-strain curve reported by Monea *et al.* [1]. After all the results being analysed, the element chosen to be used in the full model of the bridging veins and superior sagittal sinus, was the S4R. Using the S4R element will avoid problems like shear locking, which tends to affect fully integrated elements making them overly stiff in bending, and increase computacional efficiency, decreasing the simulation time. However reduced integration elements may suffer from hourglassing problems, which tends to make the element excessively flexible, nevertheless this problem can be solved by toggle on the hourglassing control option and by using finer meshes. Figure 3.8, shows the initial and final state of the simulation using the element S4R.

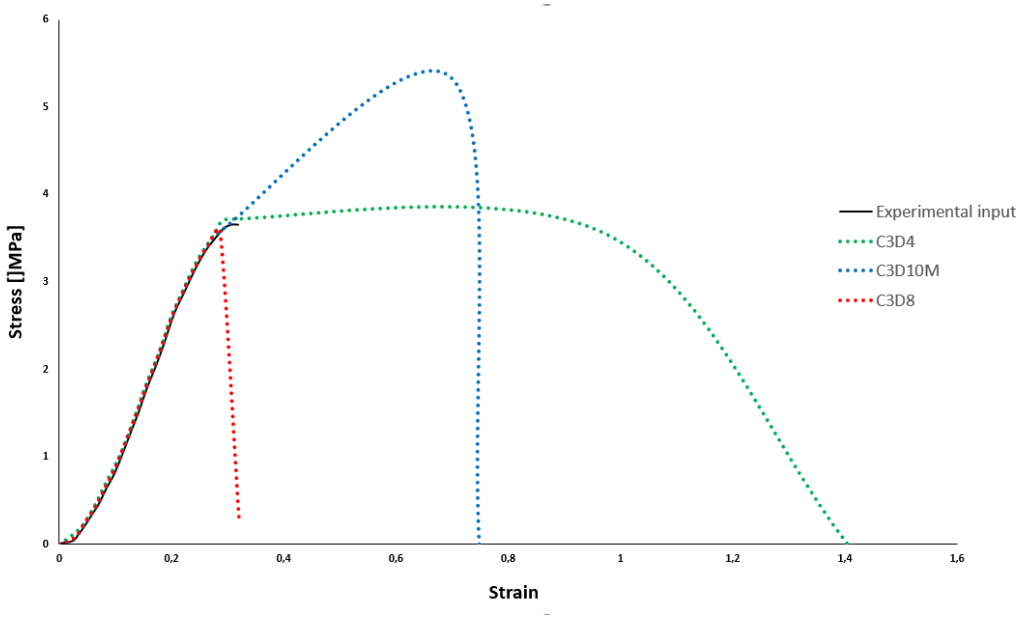

Figure 3.6: Experimental and simulated stress-strain curves for the bridging vein modeled with solid elements.

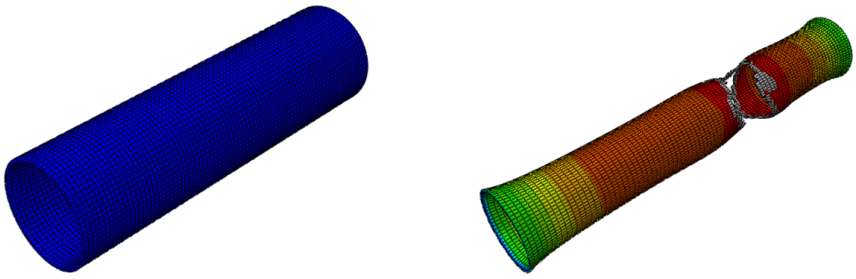

Figure 3.7: Illustration of the simulation of the mechanical test performed on the bridging vein using the C3D8 element, on the left side is the initial state and on the right the final state.

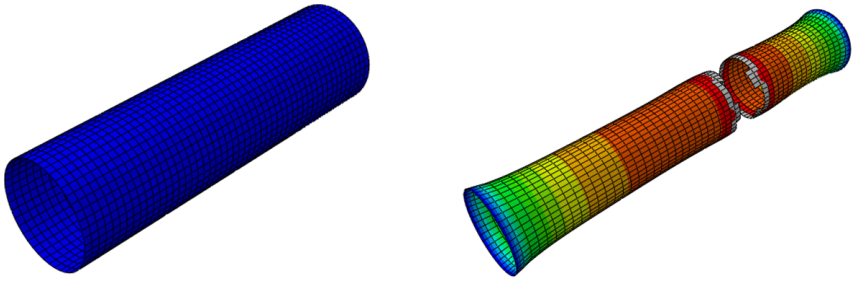

Figure 3.8: Illustration of the simulation of the mechanical test performed on the bridging vein using the S4R element, on the left side is the initial state and on the right the final state.

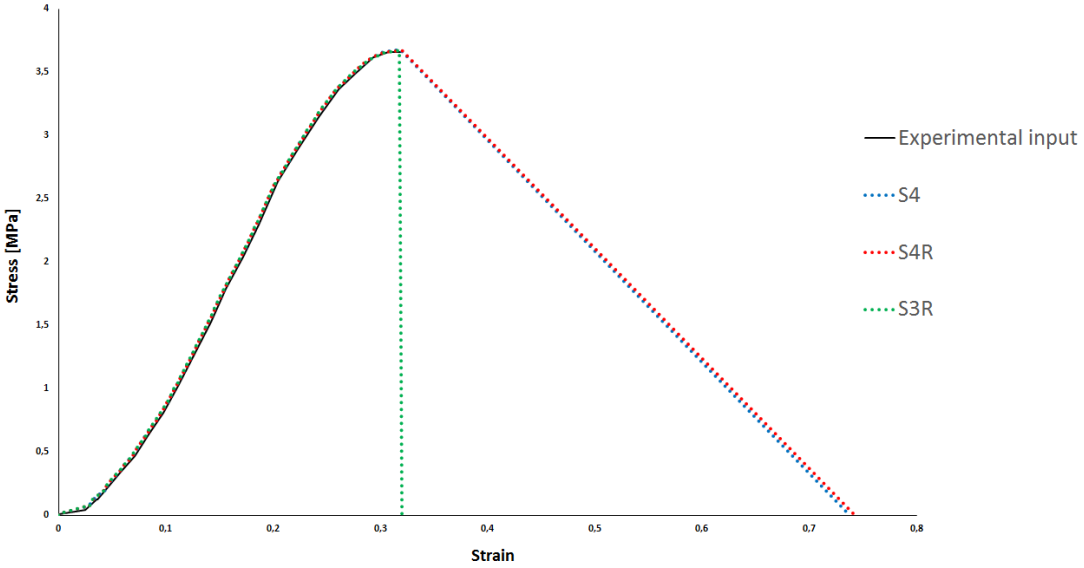

Figure 3.9: Experimental and simulated stress-strain curves for the vein modeled with shell elements.

3.3 Geometric model

The geometry of the model that is going to be used further in this work is an adaptation of the model developed by Migueis [14], which is composed of bridging veins, superior sagittal sinus, straight sinus and transverse sinus (right and left). The bridging veins were modeled with an outer diameter of 1.4 mm, the superior sagittal sinus with 6 mm, and the transverse and straight sinus with a diamter of 4 mm. All the dimensions used were based in the state-of-the-arte review, more specifically on the studies developed by Monea *et al.* [1], as can be seen in Table 2.2. The number of pairs of BVs used in this model was nine, which is in accordance with the values reported by several authors, stating the existence of eight to twelve pairs of bridging veins.

However, the CAD model developed by Migueis had two main problems. First, he modeled the bridging veins, SSS, transverse and straight sinus, considering a filled solid, as can be seen in Figure 3.10. The second problem, was that he considered the joint between the BVs and SSS totally perpendicular, having an angle of 90°, as shown in Figure 3.11, which may lead to stress concentration problems.

In order to solve this problems, the CAD developed by Migueis [14] was improved using the software SolidWorks 2017. In the first place, to improve the model, it was used a tool in the Surface tab named Offset Surface, which creates a shell with the same geometry as the original model. Figure 3.12, shows the new improved model with tubular shape veins. Then, the problem of perpendicularity between the BVs and the superior sagittal sinus was tackled. It was used a tool named fillet, as can be seen in Figure 3.13, in order to smooth the intersection.

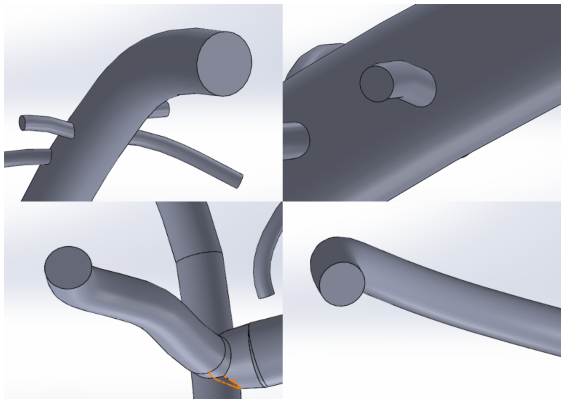

Figure 3.10: Images of the different parts of the model with filled solid geometry developed by Migueis [14].

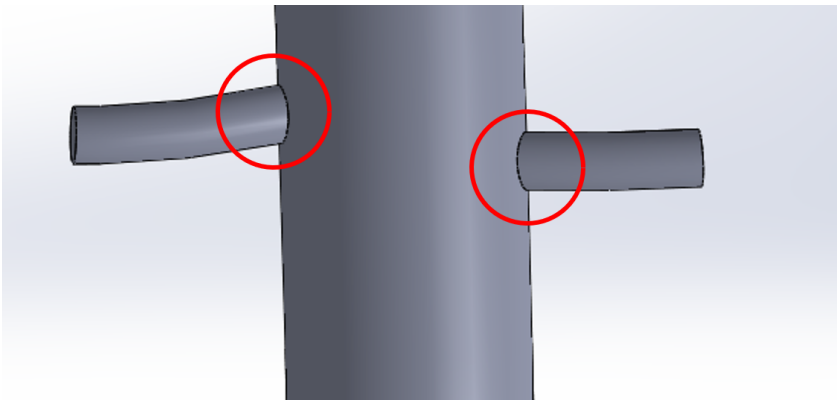

Figure 3.11: Confluence between the BVs and SSS in the model developed by Migueis [14].

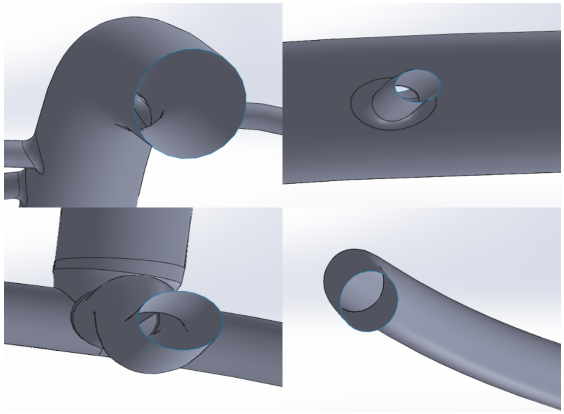

Figure 3.12: Images of the different parts of the improved model.

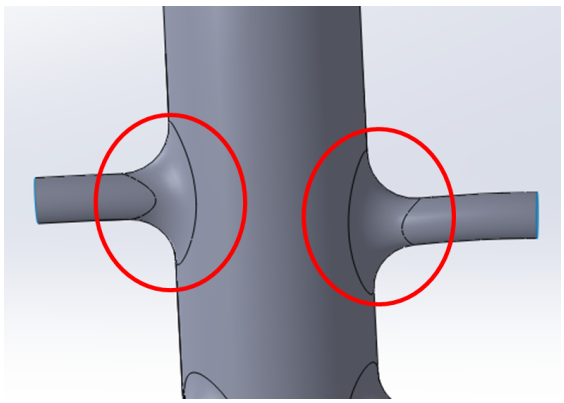

Figure 3.13: Confluence between the BVs and SSS in the improved model [14].

3.3.1 The impact of the fillet in the SSS-BV intersection

To study the impact of the fillet in the intersection between the superior sagittal sinus and the bridging veins, simulations were carried out, that reproduce the elongation of a bridging vein, using different sizes of fillets, and then by analysing the results try to understand how important is the use of the fillet and what size is the best. Due to the fact that the region of study was the intersection between only one bridging vein and the SSS, it was not necessary to use the full model in the simulations, instead it was used the model shown in Figure 3.14.

In order to carry out the simulations, first it was necessary to define the material properties, which were the same used before in the material model validation. Then, the boundary conditions were defined, an encastre on the SSS, and an elongation velocity of 1358.55 mm/s on the edge of the BV (Figure 3.15). Finally, the mesh was set using the S4R finite element. The reasons behind this choice were the same explained in the material model validation section.

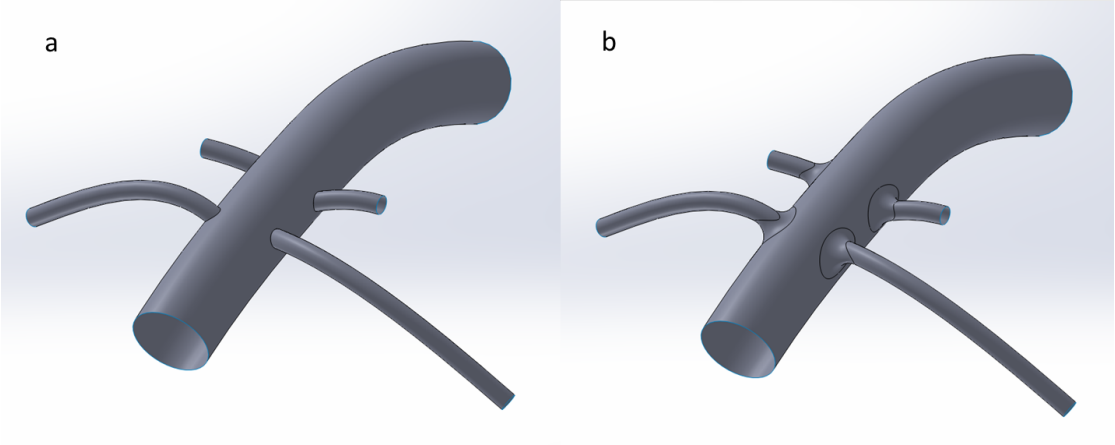

Figure 3.14: SSS-BV models, without fillet (a) and with fillet (b), used in the simulations to study the impact of the fillet.

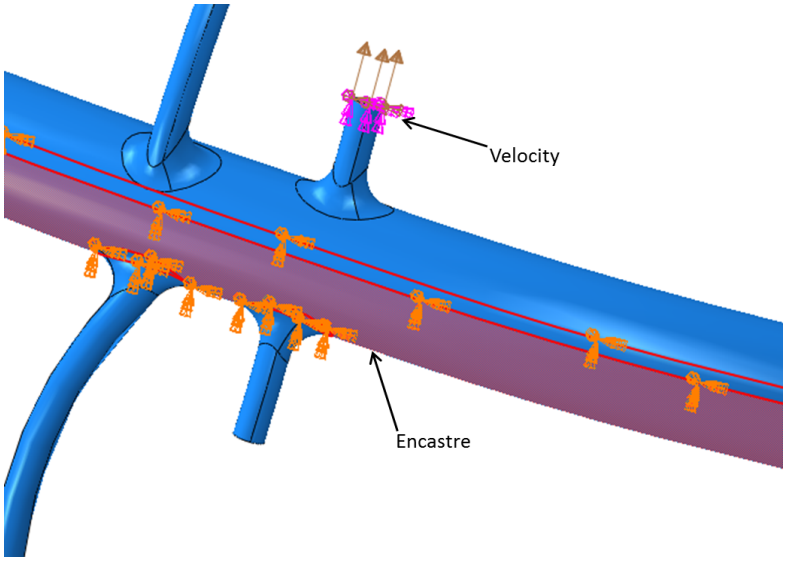

Figure 3.15: Boundary conditions used to simulate the impact of the fillets in the intersection between the BV and SSS.

To study the impact of the fillet in the SSS-BV intersection were used nine different configurations, one without fillet and eigth with fillet ranging from size 0.3 to 3 mm. For each case, five parameters were evaluated. First, as shown in Table 3.3, the regions where the maximum stress, maximum strain and rupture occured were reported. Then, for each case, was studied the mechanical behaviour of the material in the SSS-BV intersection and in the BV. For that the stress-strain curves were used, as can be seen in Figures 3.16, 3.17 and 3.18. It is important to mention that each figure has two curves, (a) corresponding to the SSS-BV intersection and (b) corresponding to the BV. Also, on the figure's label, each fillet is represented by its size multiplied by 1000 (example: 300 corresponds to 0.3 mm).

Analysing the results, two questions were asked: "which stress-strain curves were more accurate in comparison with the experimental one?" and "which case had the max stress, max strain and rupture in the same region?". The fillet that best simulated the experimental stress-strain curve, both in the intersection and in the BV, was the fillet of size 1.5 mm. Besides that, looking at the Table 3.3, it can be seen that for the fillet of size 1.5 mm all the three parameters took place in the same area.

The importance of adding fillets in the SSS-BV intersection was to reduce stress concentrations, that may appear later on the full model validation. As can be seen in Figures A.1-A.9, as the fillet size increases to 0.75 mm the stress increases in the SSS-BV intersection, only for fillet with size equal or bigger than 1 mm the stress decreases in the intersection and increases in the BV. Figure 3.19, shows the rupture in the simulation without fillet and with fillet of size 1.5 mm. As expected, for the case without fillet the rupture happens in the intersection, while for the case with fillet of 1.5 mm happens in the BV.

Finally, for all the reasons mencioned above the fillet size chosen was 1.5 mm, which was implemented on the full SSS+BV 3D CAD model shown in Figure 3.20.

Table 3.3: Region where the rupture and the maximum value of stress and strain occured for each fillet size. Int - intersection, BV - bridging vein.

	No Fillet	**Fillet 0.3 mm**	**Fillet 0.45 mm**	**Fillet 0.6 mm**	**Fillet 0.75 mm**	**Fillet 1 mm**	**Fillet 1.5 mm**	**Fillet 2 mm**	**Fillet 3 mm**
Max Stress	Int	Int	Int	Int	Int	Int	BV	BV	BV
Max Strain	Int	Int	Int	BV	BV	Int	BV	BV	BV
Region of rupture	Int	Int	BV	BV	BV	BV	BV	BV	BV

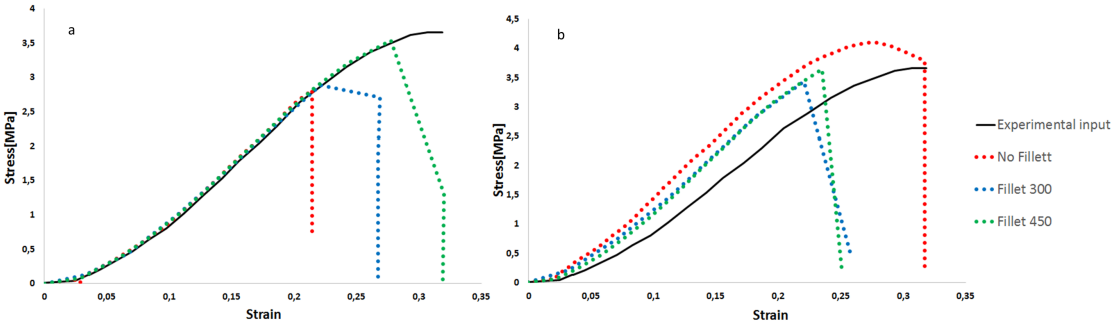

Figure 3.16: Comparasion between the experimental and simulated stress-strain curves, (a) in the BV and (b) in the SSS-BV intersection, for the case without fillet and the cases with fillet of size 0.3 and 0.45 mm.

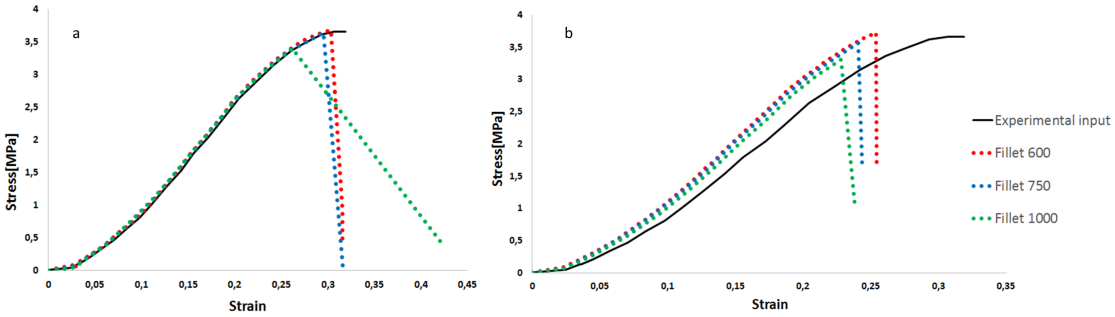

Figure 3.17: Comparasion between the experimental and simulated stress-strain curves, (a) in the BV and (b) in the SSS-BV intersection, for the cases with fillet of size 0.6, 0.75 and 1 mm.

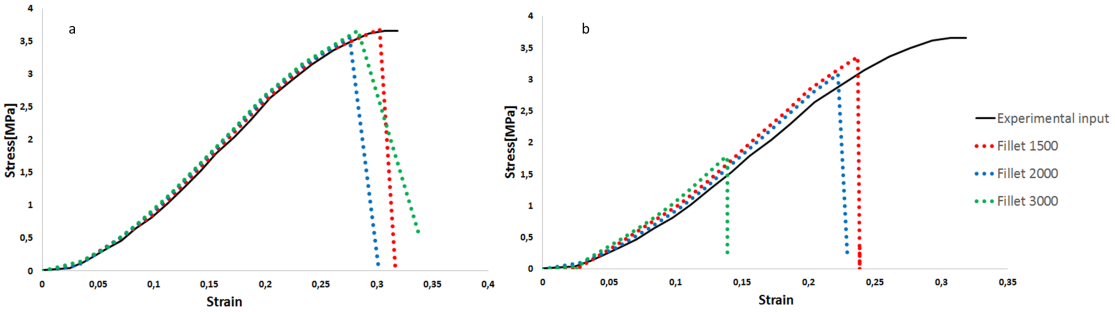

Figure 3.18: Comparasion between the experimental and simulated stress-strain curves, (a) in the BV and (b) in the SSS-BV intersection, for the cases with fillet of size 1.5, 2 and 3 mm.

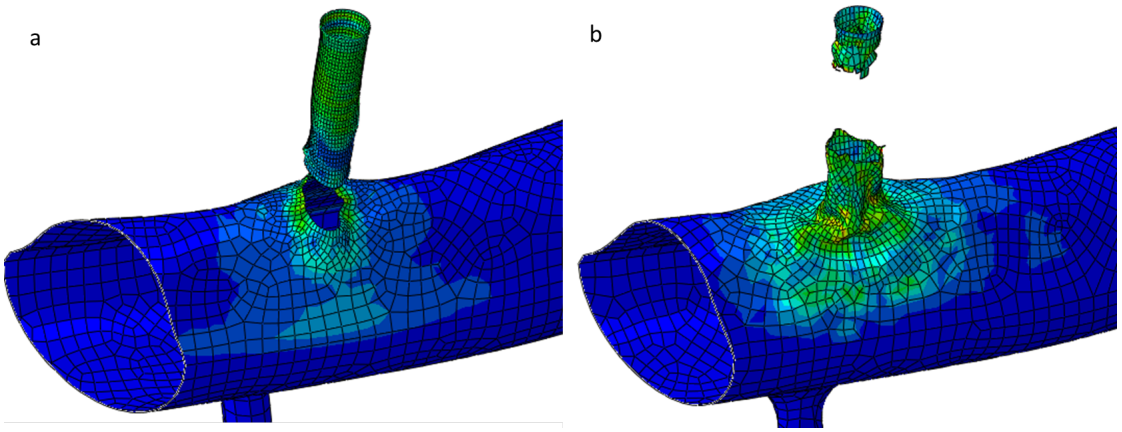

Figure 3.19: Region where the rupture occurred for the simulation (a) without fillet and (b) with fillet of size 1.5 mm.

Figure 3.20: SSS+BVs 3D CAD model.

Chapter 4

Bridging veins FE model

4.1 Depreitere's experiment

In order to validate the finite element model of the bridging veins, the experimental tests conducted by Depreitere and his colleagues [12] were simulated using the Explicit version of the FE package ABAQUS. During the experiments, Depreitere and his colleagues submitted the heads of 10 human cadavers, with mean age of 79.2 years, to impacts in the occipital area using a pendulum, and then checked if there was any BV rupture. The human cadavers were placed in an upright position in front of the pendulum with the back of the head facing it, as shown in Figure 4.1 (b). The head of the cadavers were held in position by a string attached to the nose in order to not influence the head kinematics.

The impactor used was a steel block that was attached to the end of the pendulum. To change the impact conditions, the mass of the impactor or the angle of release of the pendulum were varied.

After each impact, using a fluoroscope, they searched for a bridging vein rupture by injecting a fluid into the veins and then search for leaks. If no rupture was found, the cadaver was used for a second impact.

To collect the data from the impacts, three uniaxial accelerometers were fixed on the left side of the head, near to the ear, as shown in Figure 4.1 (a). The accelerometer in the middle was used to measure the linear acceleration, that was used to estimate the tangential acceleration of the head's centre of mass, while the combination of the three was used to obtain the mean rotational acceleration.

The acceleration curves collected by Depreitere and his colleagues are the ones that are going to be used as inputs to validate the model developed in this work. However, from the 18 impacts, only 12 have enough information to be used in the simulations. Even in these 12 cases, only the rotational acceleration curves are fully known. The linear acceleration curve is only reported for the case 2 and can be seen in Figure 4.2, while all the others had to be manipulated based on that one. Nevertheless, Depreitere and his colleagues state that the linear acceleration signals showed a typical pattern, which means that for all the cases, the curves have a similar shape, varying the peak and pulse duration [183]. Figures B.1 and B.2 show the linear acceleration curves for all the 12 cases created based on the case 2 curve, whereas Figures B.3 and B.4 show the rotational acceleration curves reported in Cui *et al.* [184]. Table 4.1 shows the different parameters for each one of the 12 cases. Each case is identified with a number, from 1 to 12, by the impact order, which is 1 if it was the first impact or 2 if it was the

second impact to the head, a peak rotational acceleration, a pulse duration from the linear acceleration curve, a peak tangential acceleration, and the side of the BV rupture.

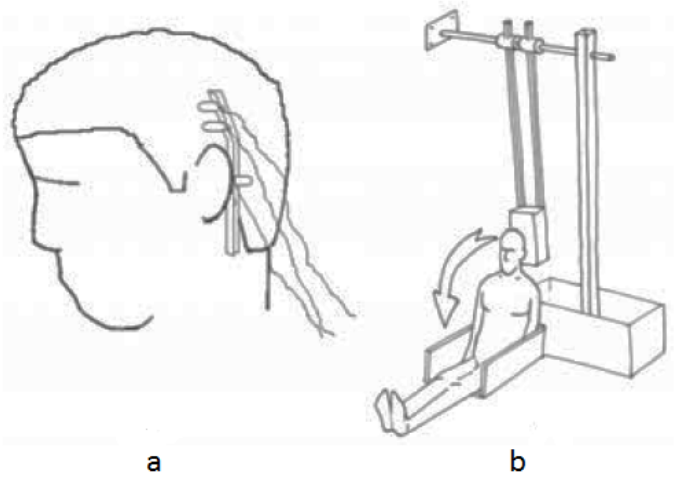

Figure 4.1: Illustration of the experimental tests conducted by Depreitere and his colleagues, (a) position of the three uniaxial accelerometers on the head, (b) position of the human cadaver relative to the set pendulum-impactor. Adapted from Depreitere *et al.* [183].

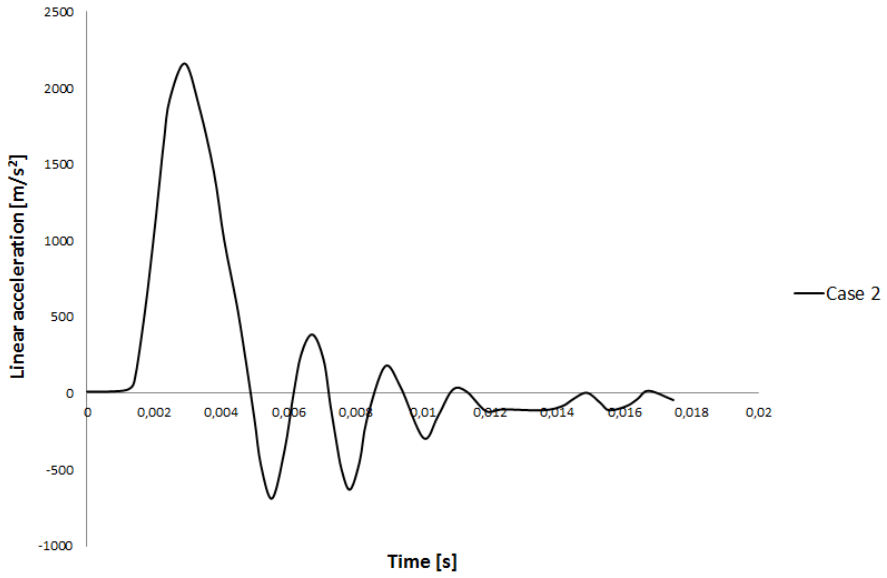

Figure 4.2: Linear acceleration curve for case 2. Adapted from Cui *et al.* [184].

Table 4.1: Summary of the parameters for the 12 impact experiments conducted by Depreitere and his colleagues. Adapted from Cui *et al.* [184].

Case no.	Impact order	Peak rotational acceleration (rad/s^2)	Pulse duration (ms)	Peak tangential acceleration of the head's center of mass (m/s^2)	Bridging vein rupture (side)
1	2	26262	5.2	4522	Rupture (left)
2	1	7312	4.5	2161	No rupture
3	2	7975	5.3	2021	No rupture
4	1	12867	15.4	1522	Rupture (right)
5	1	4950	10.4	1887	No rupture
6	1	6244	11.9	2329	No rupture
7	2	6056	10.5	1678	No rupture
8	1	15156	12	3676	No rupture
9	2	9708	12.6	2112	Rupture (right)
10	1	2454	10.2	1352	No rupture
11	1	3044	5.5	2041	No rupture
12	1	19572	7.7	2354	Rupture (right)

4.2 Finite element model definitions

In order to validate the bridging veins finite element model using ABAQUS, before running the simulations, several steps were necessary to develop the model. First the 3D CAD model of the SSS+BVs was imported from Solidworks to ABAQUS. Then, it was followed the same procedure as in Chapter 3, regarding the material model validation. A shell section with thickness of 0.044 mm was created and the material properties, according to the mechanical behaviour reported in the state-of-the-art and validated on Chapter 3, were assigned to the section. After that the SSS+BVs model was assembled on the YEAHM as shown in Figure 4.3, where it is also possible to see the nine pairs of bridging veins numbered. However, the right BV of pair 1 and the two BVs of pair 9 are not considered in the simulations since they are excessively small, which would led to false positive because a small displacement would rupture the BV.

The SSS+BVs model was meshed with S4R element, following the conclusions drawn from Chapter 3. However, due to the complex geometry of the SSS+BVs model it was necessary to use a "Quad-dominated" mesh, which means that a small part of the mesh elements are triangular. Nevertheless, as reported in Chapter 3 the S3R element also worked well alongside with the S4R element. The mesh has a total of 42359 elements, being 97.27% S4R and 2.73% S3R.

To simulate the interface between the different parts of the head, the contact interaction used was the same defined in the model developed by Migueis [14], a general contact "all with self" with a friction coefficient of 0.2. Also to simulate the stretch of the BVs due to the relative movement between the skull and the brain it was necessary to define tie constraints. A tie constraint fixes two surfaces together, which means that makes both linear and rotational motions equal for a pair of surfaces [181].

To recreate the experimental tests conducted by Depreitere and his colleagues, since the linear and rotational accelerations were measured as explained before, there is no need to model the impactor. Instead, the accelerations measured by Depreitere and his colleagues are applied on a node on the left side of the skull, as shown in Figure 4.4 (a), corresponding to the point where the accelerometers were positioned. The linear

acceleration was applied in the x axis direction while the rotational acceleration was applied around the y axis, as explained in Figure 4.4 (b).

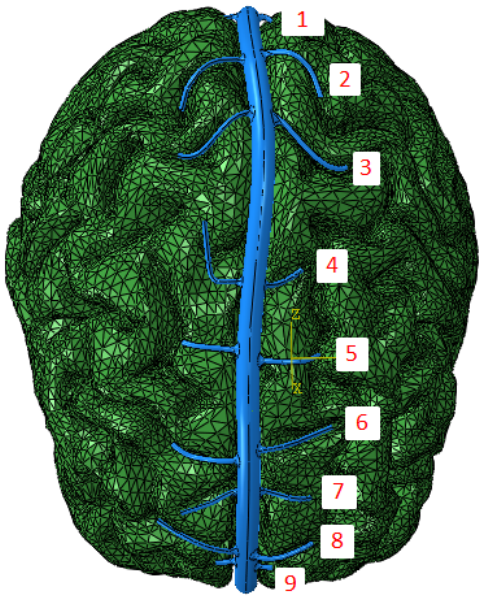

Figure 4.3: Assembly of the SSS+BVs model on the brain.

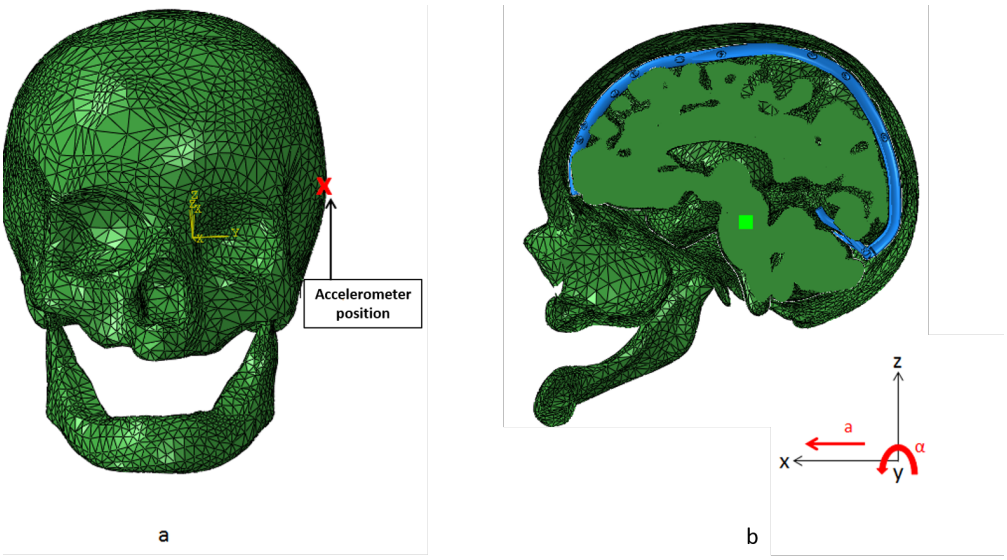

Figure 4.4: (a) Frontal view of the skull with the point where the linear and rotational acceleration were applied (b) Cutaway sagittal view of the skull, showing the axis of reference with the direction of the linear acceleration (a) and the rotational acceleration (α).

After all the definitions have been established, the SSS+BVs finite element model

was ready to be validated. The first case simulated was the case 2 since it is the only one that has the two original acceleration curves as explained before, being the reference case to analyze the model behaviour. After analysing the simulation results, it was clear that some things were not right. Besides the fact that existed multiple ruptures on the bridging veins, which was not supposed to happen in this case, the model showed strange behaviours. First, the bridging veins flattened, losing a significant amount of volume as can be seen in Figure 4.5. The second problem was that the SSS and BVs were being deformed by the CSF resulting in ruptures, what was not supposed to happen. Figure 4.6 shows on the left the interaction between the SSS and the CSF and on the rigth the missing elements of the SSS. Last but not least, the SSS was moving away too much from the brain as shown in Figure 4.7, this movement besides not being realistic will led to false results, since the frontal BVs will easily tear due to the SSS excessive displacement.

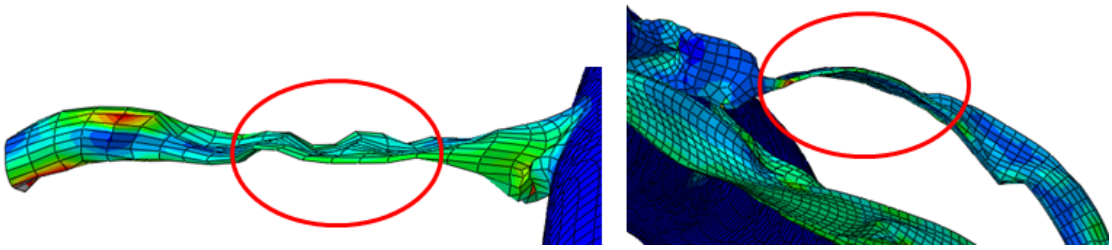

Figure 4.5: Example of the lost of volume in two different bridging veins.

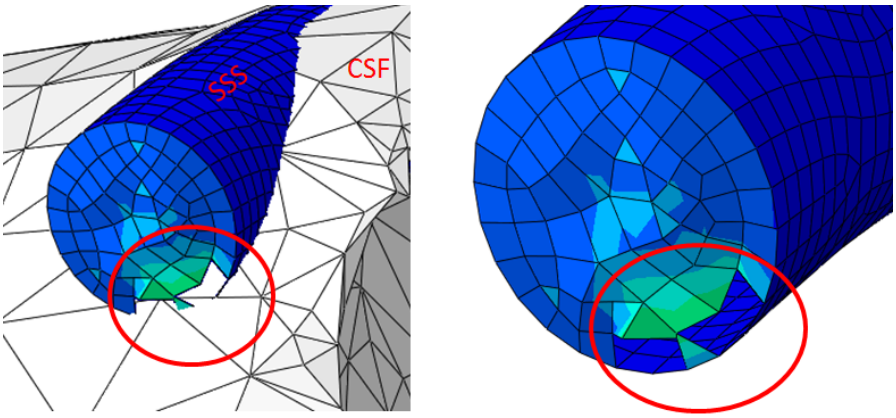

Figure 4.6: Example of a rupture in the SSS due to the interaction between the SSS and the CSF.

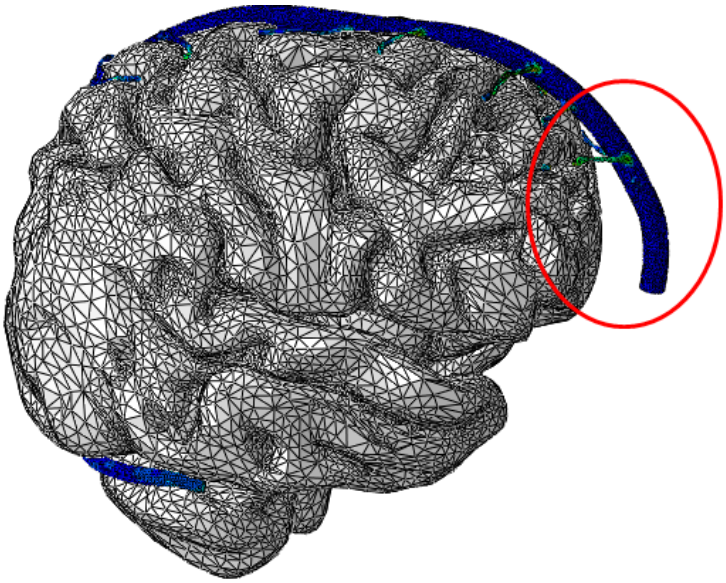

Figure 4.7: Excessive movement of the SSS relative to the brain.

The three main problems explained above had to be solved. To solve these issues several changes had to be made in the definitions of the SSS+BVs finite element model, which are explained below, step-by-step.

1st Problem - BVs loss of volume

As explained before and shown in Figure 4.5 the bridging veins flattened, losing volume. To solve this problem it was necessary to implement some condition to prevent the BVs to become flat. The best option was to add a fluid that simulates the blood, with the same mechanical properties, and most importantly, to pressurize the vessel in a similar manner to blood pressure in the bridging veins. The easiest way to model the blood was to use an interaction named fluid cavity. This interaction besides being easy to define is a very cost-effective alternative to simulate pressurized fluid-filled vessels in comparison with other numerical solutions to model fluids. However, the fluid cavity interaction requires the model to be a closed surface, otherwise it will abort the simulation. For this reason the damage model used in chapter 3 to eliminate the elements that exceeded the rupture strain was suppressed. From now on, the plastic strain (PE) value is monitored to determine failure, which means that if the strain is higher than 0.31875, there is a rupture.

To define the fluid cavity interaction it was necessary to set three parameters, the fluid density, the fluid bulk modulus (K), and the fluid pressure, which are presented in Table 4.2. It is important to mention that no report was found on the blood bulk modulus, so the value used of 2.66 GPa is from the white blood cells.

The blood pressure varies depending on the phases of the cardiac cycle. When the heart is contracting, it is in the so-called systolic phase, which is characterized by a higher pressure. On the other hand, if the heart is relaxed, it is in the diastolic phase, where the pressure is lower. Since the superior sagittal sinus and bridging veins are venous

blood vessels, they carry venous blood into the heart when it is relaxed, so the diastolic blood pressure was used. In a healthy person the diastolic pressure should not exceed 80 mmHg which is equivalent to 10.66 KPa.

Table 4.2: Blood mechanical properties used to define the fluid cavity interaction.

	Value	**Reference**
Density [kg/m^3]	1060	[185]
Bulk modulus [GPa]	2.66	[186]
Pressure [KPa]	10.66	[187]

2nd Problem - Interaction between the SSS+BVs and the CSF

As explained before and shown in Figure 4.6, the CSF was deforming the SSS and the BVs, what was not supposed to happen. This problem was being created by the contact interation defined by Migueis [14] in the previous model. As said before he used a general contact "all with self", which means that all the parts of the model interact with each other. To solve this problem the general contact continued to be used, however instead of use the "all with self" option was used the surface pairs option. With this option we are able to choose what parts of the model are interacting. Table 4.3 shows the surface pairs and respective friction coefficient used to define the general contact interaction. Since the surface pair SSS+BVs/CSF was excluded there will be no interaction between these two parts, this way the CSF will not deform neither the SSS nor the BVs.

Table 4.3: Surface pairs and respective friction coefficient used to define the general contact interaction.

First surface	**Second surface**	**Friction coefficient**
Skull	SSS+BVs	0.05
Skull	CSF	0.2
CSF	Brain	0.2
Brain	SSS+BVs	0.2

3rd Problem - SSS excessive movement

The third problem associated with the inital definitions of the finite element model was that the SSS was moving away from the brain too much as shown in Figure 4.7, leading to unrealistic ruptures in the frontal bridging veins. To solve this problem the tie defined between the SSS and skull had to be changed. The software ABAQUS has a result output that shows what elements are tied or not tied. As can be seen in Figure 4.8 the SSS was all tied to the skull, this causes the front part of the SSS to move away from the brain too much, as shown in Figure 4.7. To control this movement the tie was shortened as can be seen in Figure 4.9. Now the front part of the SSS is red which means that is not tied to the skull, this way the front part will not follow the skull thereby controlling the movement of the SSS.

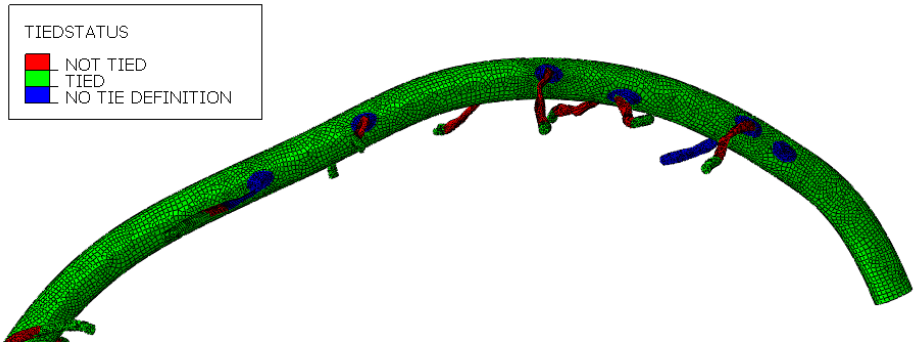

Figure 4.8: Initial tie between the skull and the SSS.

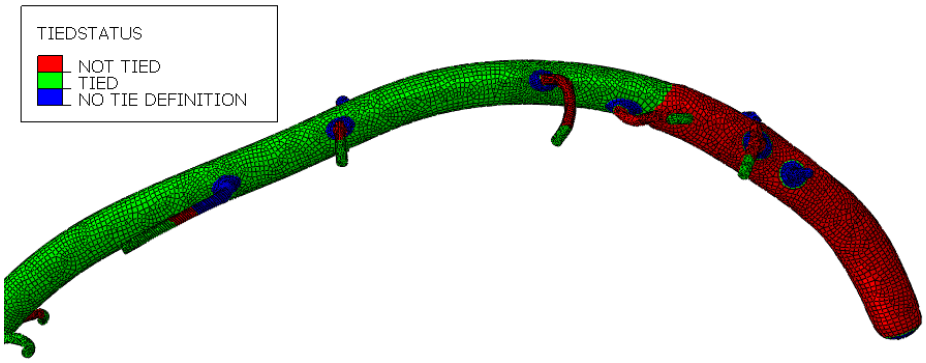

Figure 4.9: Improved tie between the skull and the SSS.

Once the changes were made, the case 2 was simulated again, to try to understand by comparing with the previous results if the changes had a positive outcome. Figure 4.10 shows the same two bridging veins shown in Figure 4.5 after the fluid cavity interaction has been implemented. It is clear that the bridging veins no longer lost volume.

As said before, because of the fluid cavity interaction, the damage model had to be supressed, so if an element exceeds the rupture strain, it is no longer eliminated. The strain value is used to determine if the elements ruptured. By looking at Figure 4.11 it can be see that unlike what happens in Figure 4.6 the SSS has no elements with the strain value higher than 0.31875, which means the interaction problem between the SSS+BVs and the CSF was successfully solved.

Last but not least, Figure 4.12 shows that the SSS is no longer excessively moving away from the brain in comparison to what happened before the tie was changed. This way, the SSS displacement is much more controlled, helping to prevent false ruptures of the frontal bridging veins.

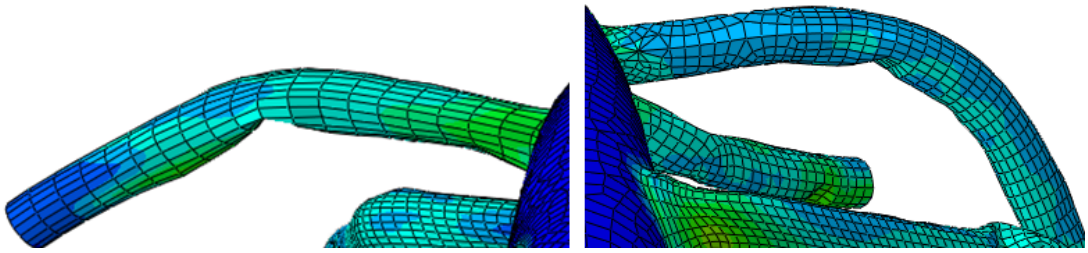

Figure 4.10: Bridging veins after the loss of volume has been solved.

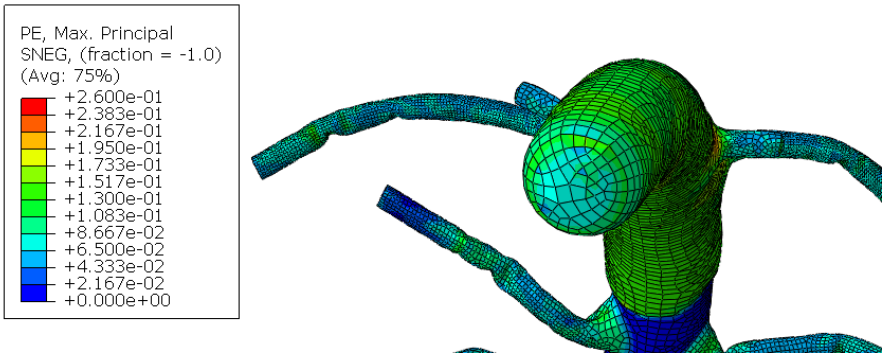

Figure 4.11: SSS deformation after the interaction problem between the SSS+BVs and the CSF has been solved.

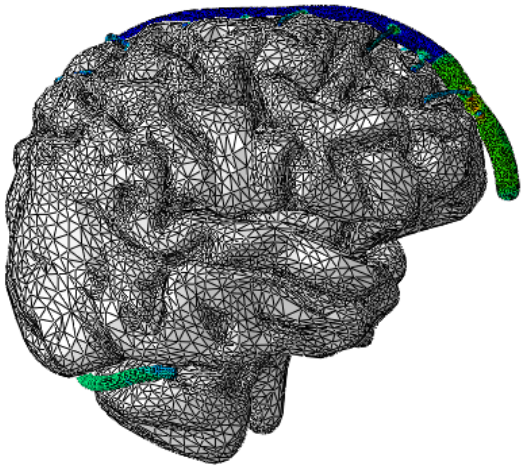

Figure 4.12: Positioning of the SSS relative to the brain after the excessive displacement of the SSS problem has been solved.

4.3 Validation of the bridging veins FE model

The definitions and conditions used by Migueis [14] to set the bridging veins FE model and simulate the Depreitere's experiments were assigned to the new model developed in this work. As explained before those definitions presented several issues. First the CSF was deforming and in some cases tearing the SSS and the BVs due to the general contact "all with self" definition, which assumes that all the parts of the model interact between each other. Then the SSS was moving too far from the brain leading to unrealistic ruptures on the frontal BVs. Lastly, since the model geometry was changed from a filled solid body to a tubular shape with thickness, instead of using solid elements had to be used shell elements. The use of shell elements brought new problems because the BVs were losing volume, becoming flat. Nevertheless all the issues were solved as explained before leaving the model ready to be validated.

To validate the model, the 12 cases from the Depreitere's experiments shown in Table 4.1 were simulated. Some studies that work on the success rate of FE models to predict ASDH such as the one developed by Cui *et al.* [184] use all 12 cases. However from those 12 cases, four are second impacts. For this reason, more recent studies such as the one developed by Kapeliotis *et al.* [27] uses only 8 cases, since they claim the applied damage from the first impact cannot be accounted for. Table 4.4 shows the success rate values for the Cui *et al.* [184] study and for the Kapeliotis *et al.* [27] study, as well as the number of false negatives and false positives. It is important to mention that the false negatives are less desirable from a head protection point of view. However, in this work, three methods of success rate calculation are presented, using 8, 10 and 12 cases. The reason for the use of 10 cases to calculate the success rate is that even though 4 cases are second impacts, two of those four are non-ruptures. If it was a second impact and yet no rupture was detected, logically if it was the first impact there would be no rupture either. The same cannot be stated for the other two cases, since it is not clear if they were first impacts would rupture or not for the same impact conditions. That said, the use of 10 cases to calculate the success rate seems the best option. Nevertheless, in order to compare the results against those in the literature the success rates based on the use of 8 and 12 cases were also computed.

Table 4.4: Success rate for two different studies.

Number of cases used	**Success rate** (%)	**False negatives**	**False positives**	**Reference**
8	87.5	1	0	[27]
12	75	3	0	[184]

The 12 cases were simulated multiple times to refine the tie contrains of each bridging vein in order to validate the model as accurate as possible. Figure 4.13 shows in green the final BVs and transverse sinuses ties to the brain. Each vein is identified with the number of the pair to which it belongs, as well as the side on which it is located. The same reasoning was applied to the transverse sinues.

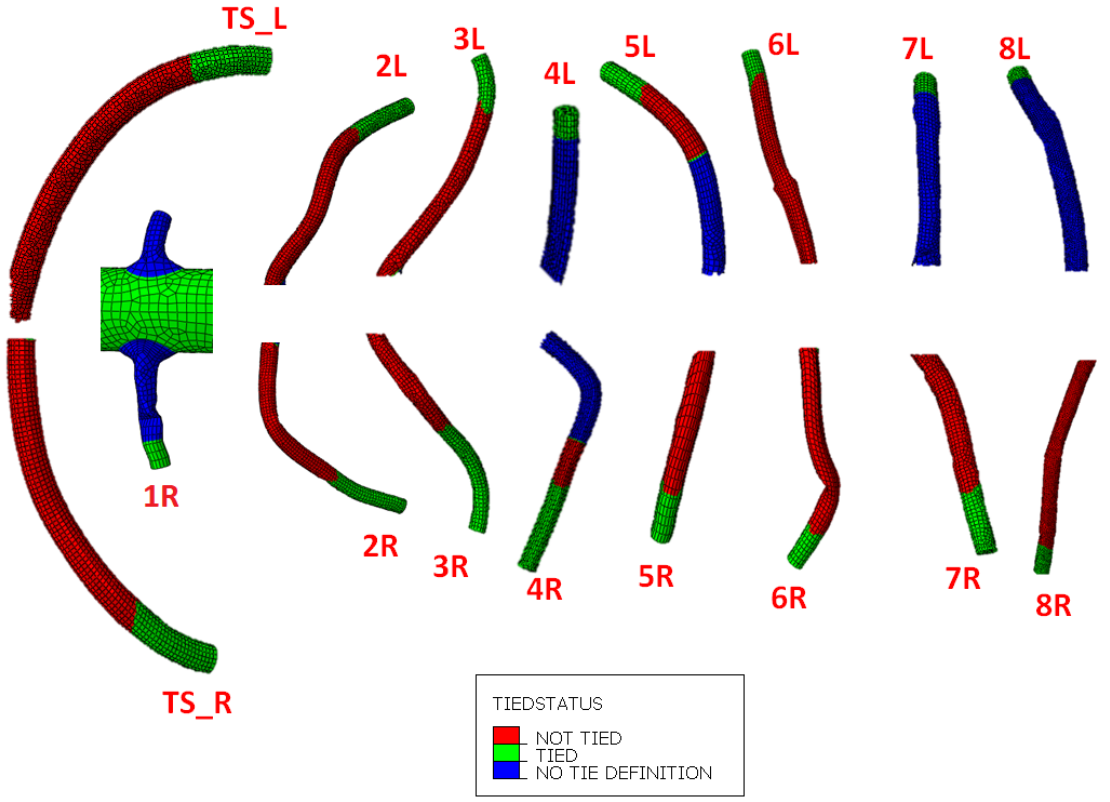

Figure 4.13: Elements of the bridging veins and transverse sinuses tied to the brain. L - left, R - right, TS - transverse sinuses.

The comparison between the Depreitere's experiments and the simulations using the YEAHM together with the bridging veins FE model is shown in Table 4.5. It is also reported the maximum plastic strain (PE) at the end of the simulation. Table 4.6 shows the success rates for the different number of cases used in this work in order to validate the bridging veins FE model, as well as the number of false negatives and false positives.

Figures 4.14, 4.15, 4.16 and 4.17 show cases 1, 4, 8 and 12 where ruptures occurred, which are highlighted with red circles. Figures 4.18 and 4.19 show the critical element for the cases 6 and 11, where the plastic strain (PE) exceeded the threshold of 0.31875. Although in these two cases the BVs did not rupture, as shown in Figures C.7 and C.8, there was an element that due to its poor quality exceeded the rupture strain. Nevertheless, this element is excluded from the bridging vein rupture analysis since it is not relevant. Figures C.1-C.6 show the simulation results for the cases without rupture and global strain value lower than 0.31875. It is also important to mention that in all the figures, it is reported the number of the BV pair.

Table 4.5: Comparison between the results of the Depreitere's experiments and the simulations with the bridging veins FE model. R - rupture, NR - no rupture, FN - false negative, FP - false positive.

Case no.	Depreitere's Experiment	Bridging veins FE model	Max strain	Observations
1	R	R	2.378	-
2	NR	NR	0.2887	-
3	NR	NR	0.2911	-
4	R	R	2.443	-
5	NR	NR	0.2824	-
6	NR	NR	1.872	-
7	NR	NR	0.2778	-
8	NR	R	1.799	FP
9	R	NR	0.2844	FN
10	NR	NR	0.26	-
11	NR	NR	0.4535	-
12	R	R	3.105	-

Table 4.6: Success rates obtained in this study for the different number of cases used.

Number of cases used	Success rate (%)	False negative	False positive
8	87.5	0	1
10	90	0	1
12	83.3	1	1

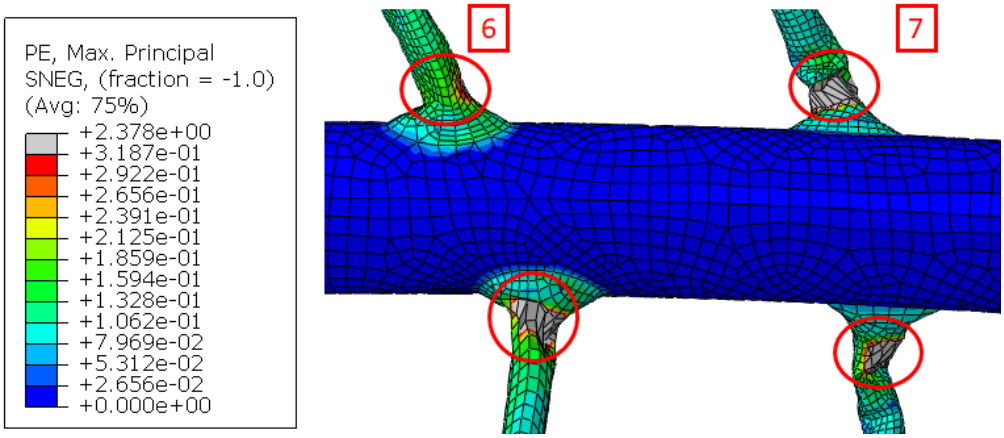

Figure 4.14: Maximum PE of the ruptured bridging veins for the case 1.

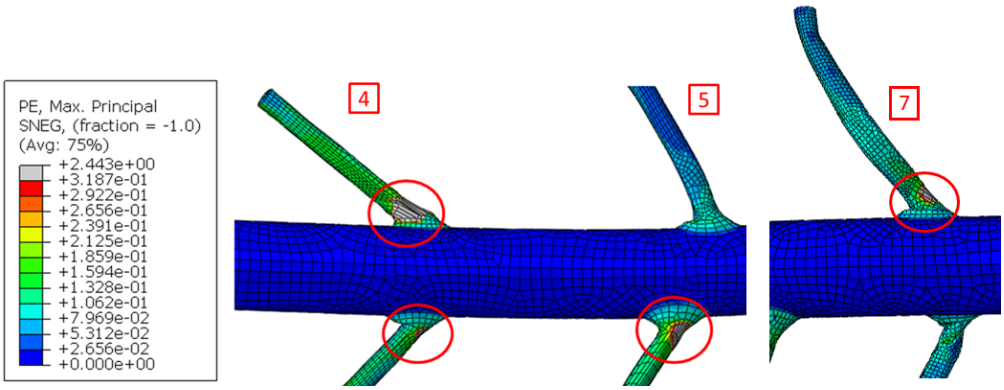

Figure 4.15: Maximum PE of the ruptured bridging veins for the case 4.

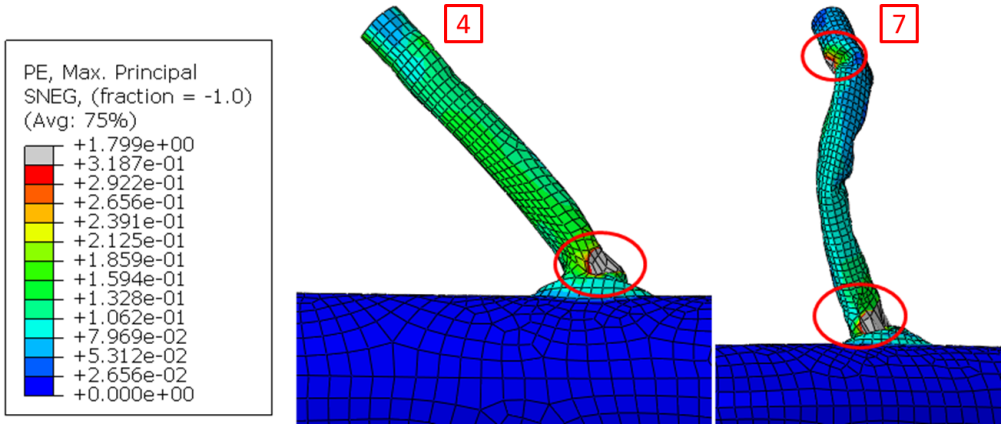

Figure 4.16: Maximum PE of the ruptured bridging veins for the case 8.

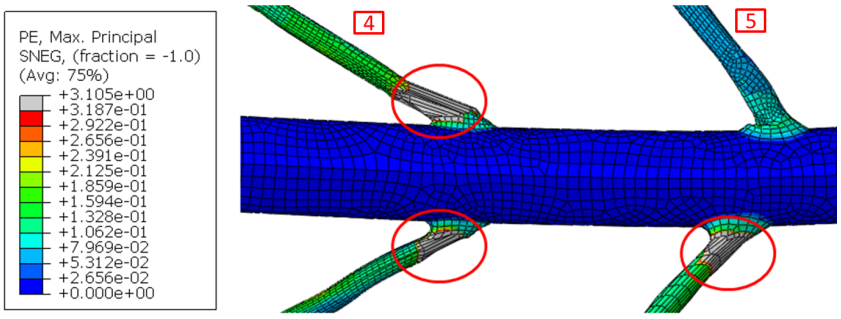

Figure 4.17: Maximum PE of the ruptured bridging veins for the case 12.

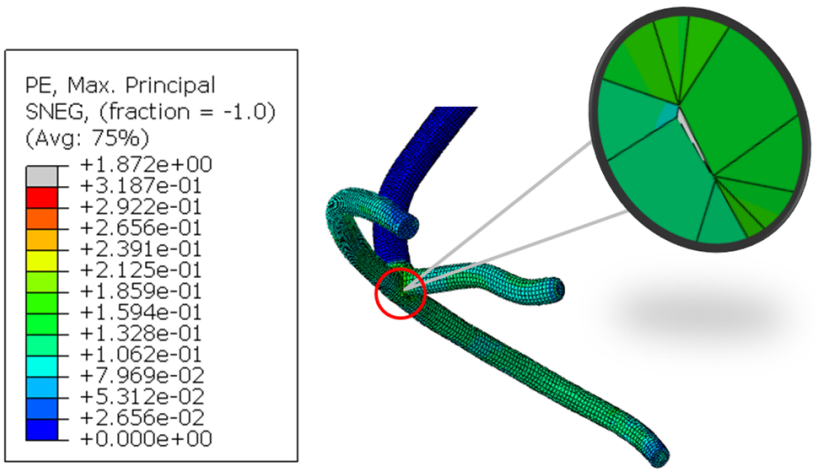

Figure 4.18: Maximum PE of the critical element for the case 6.

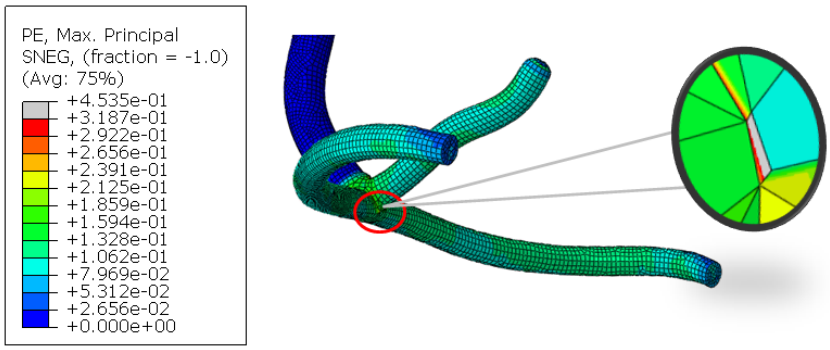

Figure 4.19: Maximum PE of the critical element for the case 11.

4.4 Discussion

The ultimate goal is to reach a bridging veins representation in FE head models that allows to predict BVs ruptures with 100% success rate in comparison with the Depreitere's experiments. Once the model has 100% success rate, it can be used in the reconstruction of injurious events by predicting ASDH, helping in the development of protective head gear as a design tool.

In this study, the goal was to develop a 3D bridging veins FE model with a high success rate on the prediction of BVs rupture, which would be a huge step in the FE head models field since to the author knowledge would be the first 3D bridging veins FE model with tubular shape, that also takes in consideration the blood pressure, to be developed and validated.

As said before the 12 cases from the Depreitere's experiments shown in Table 4.1 were simulated. The success rate consists on how many successful predictions the model can obtain, being 12 the maximum. As explained before there are several ways to calculate

the success rate, depending on how many cases are used. Some authors use all the 12 cases while others only use 8 cases, however for the reasons already explained the use of 10 cases seems to be the most logical. Nevertheless, for comparison purposes the success rate was calculated for the three methods, as can be seen in Table 4.6.

After analysing the simulation results it was clear that each case had to be analyzed individually, since for some cases the maximum strain value at the end of the simulation was not enough to dictate whether or not there was rupture in the BVs. In cases 6 and 11 even though the strain value at the end of the simulation was higher than the rupture strain, no rupture was detected in the BVs as can be seen in Figures C.7 and C.8. For these two cases the high strain value was created by an element with poor quality on the confluence of sinuses, as shown in Figures 4.18 and 4.19. However, for the analysis of the BVs rupture, the strain value in this element is irrelevant. On the other hand, for the other five cases where no ruptures were detected the global strain value was always lower than the rupture strain (0.31875), as can be seen in Figures C.1-C.6 (for those cases it was easy to detect the absence of ruptures). For the cases 1, 4, 8 and 12 where ruptures did occured, it is clear by looking at Figures 4.14, 4.15, 4.16 and 4.17 that the high strain value was not due to an element with poor geometry but because of real ruptures highlighted with red circles in the SSS-BV intersection.

Analysing Table 4.5, only two cases failed the prediction, the cases 8 and 9. Curiously the two cases are related, since the case 9 was the second impact to the cadaver head after the case 8 (first impact).

As said before the success rate is calculated based on the number of successful predictions that the model can obtain. Table 4.6 shows the success rate based on the number of cases used as well as the number of false negatives and false positives.

The success rate obtained in this work using 12 cases in comparison with the success rate reported by Cui *et al.* [184] also using 12 cases is significantly better. Even though the difference in the number of wrong predictions is only one, being 2 for this study and 3 in Cui *et al.* [184], because the number of total cases is low the change on the success rate is significantly high, going from 75% to 83.3%. Besides that, it also important to mention that in Cui *et al.* [184], all the wrong predictions are false negatives, whereas in this study only one is false negative being the other one false positive. This is important because false negatives are less desirable.

When using 8 cases the success rate obtained in this study was equal to the maximum success rate reported by Kapeliotis *et al.* [27]. However for the Kapeliotis *et al.* [27] study, the wrong prediction was in case 4, which means it is a false negative since in the simulation there was no rupture in the bridging veins, contrary to what was reported by Depreitere *et al.* [12]. On the contrary, in this work, the wrong prediction is a false positive. Once again, this is a relevant improvement since from the head safety point of view, the false negatives are less desirable.

It is also important to mention that in the cases with BVs ruptures, most occured in the middle area of the brain, similarly to the findings in Depreitere *et al.* [12], which states that all the ruptures occured in the rolandic and postrolandic area of the brain. Bridging veins pairs 4, 5 and 6 are considered to be located in the middle area of the brain. By looking at Figures 4.14-4.17, it is possible to see that from a total of 13 ruptures only 4 were located on the BVs pair 7, which is consider to belong to the frontal area of the brain.

In summary, it is fair to say that the bridging veins model developed in this work is

a huge step in the state of the art of FE models, regarding bridging veins, not only for being to the author knowledge the first 3D bridging veins FE model with tubular shape to be developed, that also takes in consideration the blood pressure, but also because presents better prediction results.

Nevertheless the improvement of the prediction success rate is not only related with the improvement of the bridging veins FE model but also with the improvement of the YEAHM. In the YEAHM the space between the skull and brain is consider to be the CSF, modeled as a solid with low shear modulus. It is expected that with the add of the three layers of meninges, dura mater, arachnoid mater and pia mater, as well as the add of the falx cerebri, the reliability of the bridging veins FE model will increase even more. Also, it would be important to take into account the intracranial pressure. For that, it is necessary to model the CSF as a fluid, similar to what was done with the bridging veins in this work.

Finally, in order to increase the confidence level of the bridging veins FE models, more experimental data for validation is required, because right now the results are based on only 12 cases from the Depreitere's experiments. It would be important to collect data from other head impact areas with different acceleration directions, since it is likely the pattern of bridging veins ruptures will change.

Chapter 5

Conclusions and future work

5.1 Conclusions

The main goal of this work was to improve and validate the 3D bridging veins FE model developed by Migueis [14], that later could be used to predict ASDH and consequently help on the development of damage criteria and head protective gear.

At a first stage, the material and damage model were validated using both shell and solid elements. Bridging veins are described as nonlinear, anisotropic, viscoelastic and prone to rupture. Although biological tissue is often modeled using the hyperelastic constitutive model, instead it was used the elastoplastic constitutive model. The reson for this choice was that elastic-plastic theory was simpler to characterize the BVs, even from a computacional point of view. With the material model validation it was concluded that the shell elements were the best choice. Furthermore, it was seen that due to the complex geometry of the SSS+BVs 3D CAD model, the shell elements were the only viable option.

After the material model validation the 3D CAD model developed by Migueis [14] was improved. This model presented two major problems. The first problem was the modeling of SSS and bridging veins as completely solid structures (cylinders). The second problem was the over simplified intersections between the SSS and BVs (90°angles). Both issues made the model unrealistic. The model was changed to a pipe-like structure with the same geometry of the original body. To solve the SSS-BVs intersection problem, uniaxial tests were simulated using several fillet sizes to analyze which one presented better results. After the results have been analyzed, the fillet size chosen was 1.5 mm and the model was assembled to the YEAHM.

To validate the model against the 12 cases from the Depreitere's experiments the complete time history of the linear and rotational acceleration curves reported by Depreitere [12] were used. However Depreitere only reported the linear acceleration curve for the case 2, all the other linear acceleration curves had to be manipulated based on that one and on the peak linear acceleration and pulse duration. Nevertheless, before the validation process the FE model definitions had to be set. Part of the definitions initially set were the same used by Migueis [14] on his model. However, these presented several issues. The general contact "all with self" used by Migueis [14] had to be changed to surface pairs, in order to exclude the interaction between the CSF and the SSS+BVs model. The SSS tie constraint to the skull also had to be changed in order to control the SSS excessive movement that consequently was tearing the frontal bridging veins.

The use of shell elements also brougth a new problem, the bridging veins loss of volume, becoming flat. To solve this problem, it was used an interaction named fluid cavity. This interaction simulates the blood pressure inside the bridging veins internal walls. However, with the add of this new interaction, the damage model had to be suppressed because the fluid cavity interaction requires the body to be a closed surface. Without the damage model, another solution had to be found in order to distinguish ruptures from non-ruptures. The solution was to monitor the strain value. Once the strain value exceeds the failure strain, it is consider a rupture.

The model validation consists on the calculation of the model prediciton success rate and ideally obtain a value of 100%. The success rate is nothing more than the amount of successful predictions the model can obtain out of 12 cases. However, the number of maximum cases used to validate the model varies from author to author. Some authors use the 12 cases while others only use 8 cases. This is mainly explained by the fact that 4 of the 12 cases are second impact, which some authors claim that the applied damage from the first impact cannot be accounted for. Nevertheless in this study is presented a new possiblity, which is to use 10 cases. From the 4 cases that are second impacts 2 of them are non-ruptures. If it was a second impact and no rupture was reported it is logical that if it was the first impact no rupture would be found either.

The tie constraining of the bridging veins was an effort task. The 12 cases were simulated several times in order to refine the BVs tie contraints to the brain in order to obtain the highest success rate possible. The simulation results were separated for the three different possibilities of total cases used. For each case, the success rate was calculated as well as the number of false positives and false negatives. When using 10 cases to validate the model, the success rate obtained was 90%, with only one false positive. In comparison with the two main studies that work on the success rate of FE models to predict ASDH due to bridging veins ruptures, the work here developed presents better results. When comparing with the Cui *et al.* [184] study that uses a total of 12 cases, the success rate increases from 75% with 3 false negatives to 83.3% with only one false negative and one false positive. When comparing with the Kapeliotis *et al.* [27] study that uses a total of 8 cases, both presented only one wrong prediction. However, in this work, the unsuccessful prediction is false positive whereas in Kapeliotis *et al.* [27] is false negative. The distinction between false positive and false negative is important because false negatives are less desirable from a head protection point of view. It is also important to mention that from all the ruptures, more than 68% occured in the brain's middle area. This is relevant because Depreitere and his colleagues reported that all ruptures occured in the rolandic and postrolandic area of the brain.

In conclusion, it is fair to say that the bridging veins model developed in this work is a huge step in this field, being to the author knowledge, the first model to be developed that takes in consideration the blood pressure, but manly because it presents better results.

Nevertheless, the improvement of the prediction success rate is not only related with the improvement of the bridging veins FE model but also with the improvement of the YEAHM. Therefore, two things can be done to improve the YEAHM, change the CSF from solid to fluid, and add the three layers of meninges as well as the falx cerebri and tentorium.

Finally, in order to increase the confidence level of the bridging veins FE models more experimental data is required for validation, because right now, the results are based

only in the 12 cases from the Depreitere's experiments. It would be important to collect experimental data for different directions of the acceleration vectors and for different rotation planes, since the bridging veins are likely to respond differently depending on the directions of the applied forces.

5.2 Future work

In this work, a new FE model of pressurized bridging veins was developed and validated with a maximum success rate of 90% when using 10 cases. In comparison with other studies and models available in the literature to predict ASDH caused by rupture of cerebral veins, the results are better. Nevertheless, in the future more data is required to be able to validate the FE models with more confidance.

With all the conclusions drawn from this work, it is fair to say that the model here developed is one of the first, if not the first step on the development of bridging veins FE models that also take in consideration the blood pressure. However there is still a lot of work to be done, not only in the bridging veins model but also on the YEAHM. The following future work is suggested:

- Study the influence of different material mechanical properties on the success rate of the bridging veins FE model.
- Change from isotropic elastoplastic model to anisotropic hyperelastic constitutive model.
- Divide the bridging vein wall into three layers with their own mechanical properties.
- Study the influence of the entry angles of the bridging veins into the superior sagittal sinus on the success rate of the bridging veins FE model.
- Improve and refine the bridging veins FE model mesh.
- Study the possibility of using another option to replace the tie constraints.
- Model the three layers of meninges, dura mater, aracnhoid mater and pia mater, as well as the falx cerebri and tentorium.

Bibliography

[1] Monea, A.G., Baeck, K., Verbeken, E., Verpoest, I., Sloten, J.V., Goffin, J., Depreitere, B., 2014. The Biomechanical behaviour of the bridging vein-superior saggital sinus complex with implications for the mechanopatology of acute subdural heamatoma. J. Mech. Behav. Biomed. Mater. 32C, 155-165.

[2] Kwong Ming Tse, Siak Piang Lim, Vincent Beng Chye Tan, Heow Pueh Lee. A Review of Head Injury and Finite Element Head Models. American Journal of Engineering, Technology and Society. Vol. 1, No. 5, 2014, pp. 28-52.

[3] Gennarelli, T. A., Champion, H. R., Sacco, W. J., Copes, W. S. and Alves, W. M., 1989. Mortality of patients with head injury and extracranial injury treated in trauma centers. J Trauma 1989 Sep; 29(9):1193-201.

[4] Bruzzone, E., Cocito, L. and Pisani, R. Intracranial delayed epidural hematoma in a soccer player: A case report. *Am J Sports Med* 2000 Nov-Dec; 28(6):901-903.

[5] Elhammali, N., Bremerich, A. and Rustemeyer, J. Demographical and clinical aspects of sports-related maxillofacial and skull base fractures in hospitalized patients. *Int J oral Maxillofac Surg* 2010 Sep; 39: 857-862.

[6] Kawanish, A., Nakauama, M. and Kadota, K. Heading injury precipitating subdural hematoma associated with arachnoid cysts–two case reports.. *Neurol Med Chir* 1999 Mar; 39(3):231-233.

[7] Prabhu, V.C. and Bailes, J.E. Chronic subdural hematoma complicating arachnoid cyst secondary to soccer-related head injury: Case report. *Neurosurg* 2002 Jan; 50(1):195-197.

[8] Radelet, M.A., Lephart, S.M., Rubinstein, E.N. and Myers, J.B. Survey of the injury rate fot children in community sports *Pediatrics* 2002 Sep; 110(3):e28.

[9] Pellman, E.J., Viano, D.C., Tucker, A.M. and Casson, I.R. Concussion in professional football: Location and direction of helmet impacts - Part 2. *Neurosurg* 2003 Dec; 53(6):1328-40.

[10] Fernandes, F.A.O. and Alves de Sousa, R.J. Head injury predictors in sports trauma - A state-of-the-art review. Journal of Engineering in Medicine 2015 Aug; 229(8):592-608.

[11] Gennarelli, T.A., Thibault, L.E., 1982. Biomechanics of acute subdural hematoma. J. Trauma Acute Care Surg 1982 Aug; 22(8):680-6.

[12] Depreitere, B., Van Lierde, C., Vander Sloten, J., Van Audekercke, R., Vander Perre, G., Plets, C., Goffin, J. Mechanics of acute subdural hematomas resulting from bridging vein rupture. J. *Neurosurg.* 2006 Jun; 104(6):950-956.

[13] Monea, A.G., Vander Perre, G., Baeck, K., Delye, H., Verschueren, P., Forausebergher, E., VanLierde, C., Verpoest, I., Vander Sloten, J., Goffin, J., Despreitere, B. The relation between mechanical impact parameters and most frequent bicycle related head injuries. J. Mech. Behav. Biomed. Mater. 2014 May, 33:3-15.

[14] Migueis, G.F.J., 2018. Simulação numérica da ocorrência de hematomas subdurais no cérebro. Tese de Mestrado, Universidade de Aveiro, Aveiro, Portugal.

[15] Fernandes, F.A.O., Tchepel, D., Alves de Sousa, R.J. and Ptak, M. 2018, Development and validation of a new finite element human head model, Engineering Computations, Vol. 35 No. 1, pp. 477-496.

[16] Hiatt, J.L.; Gartner, L.P. Textbook of Head & Neck Anatomy. Lippincott Williams and Wilkins, 4th edition, 2009.

[17] The Partnership in Education, Duquesne University, 2018. Retrieved April 10, 2019 from https://www.thepartnershipineducation.com/resources/nervous-system.

[18] Mayfield Brain & Spine, April 2018. Brain Anatomy, Anatomy of the brain. Retrieved April 10, 2019, from https://mayfieldclinic.com/pe-anatbrain.htm.

[19] Spinal Cord, Inc, 2019, Swope, Rodante P.A. Retrieved April 10, 2019, from https://www.spinalcord.com.

[20] Gray, H., 2008. Gray's Anatomy: The Anatomical Basis of Medicine and Surgery. Elsevier, Churchill Livingstone.

[21] Famaey, N., Ying Cui, Z., Musigazi, G.U., Ivens, J., Depreitere, B., Verbeken, E., Sloten, J.V., 2014. Structural and mechanical characterisation of bridging veins: A review. J. Mech. Behav. Biomed. Mater. Jan; 41:222-40 41:222-40.

[22] Duke University School of Medicine, 2014. Retrieved April 15, 2019 from https://web.duke.edu/anatomy/mbs/Lab19_MBS/Lab19.html.

[23] Oka, K., Rhoton, A.J., Barry, M., Rodriguez, R., 1985. Microsurgical anatomy of the superficial veins of the cerebrum. J. Neurosurg. Nov; 17(5):711-48.

[24] Brockmann, C., Kunze, S., Scharf, J., 2011. Computed tomographic angiography of the superior sagittal sinus and brdging veins. Surg. Radiol. Anat. Mar; 33(2):129-34.

[25] Han, H., Tao, W., Zhang, M., 2007. The dural entrance of cerebral bridging veins into the superior sagittal sinus: an anatomical comparison between cadavers and digital subtraction angiography. Neuroradiology Feb; 49(2):169-75.

[26] Musigazi, G.U., Depreitere, B., 2015. Study of bridging vein anatomy based on ct angiogram data for optimization of finite element models simulating acute subdural hematoma.

[27] Kapeliotis, M., Musigazi, G.U., Famaey, N., Depreitere, B., Kleiven, S., Vander Sloten, J. The sensitivity to inter-subject variability of the bridging vein entry angles for prediction of acute subdural hematoma. J Biomech. 2019 Jul 19;92:6-10.

[28] Vignes, J.R., Dagain, A., Guérin, J., Liguoro, D., 2007. A hypothesis of cerebral venous system regulation based on a study of the junction between the cortical bridging veins and the superior sagittal sinus. Laboratory investigation. J. Neurosurg. Dec; 107(6):1205-10.

[29] Pang, Q., Lu, X., Gregersen, H., von Oettingen, G., Astrup, J., 2001. Biomechanical properties of porcine cerebral bridging veins with reference to the zero-stress state. J. Vasc. Res. Jan-Feb; 38(1):83-90.

[30] Yamashima, T., Friede, R.L., 1984. Why do bridging veins rupture into the virtual subdural space?. J. Neurol. Neurosurg. Psychiatry Feb; 47(2): 121-127.

[31] Lee, M.C., Haut, R.C., 1989. Insensitivity of tensile failure properties of human bridging veins to strain rate: implications in biomechanics of subdural hematoma. J. Biomech. 22(6-7):537-42.

[32] Sampei, T., Yasui, N., Okudera, T., Fukasawa, H., 1996. Anatomic study of anterior frontal cortical bridging veins with spacial reference to the frontopolar vein. Neurosurgery May; 38(5):971-5.

[33] Monson, K.L., Goldsmith, W., Barbaro, N.M., Manley, G.T., 2005. Significance of source and size in the mechanical response of human cerebral blood vessels. J. Biomech. Apr; 38(4):737-44.

[34] Delye, H., Goffin, J., Verschueren, P., Vander Sloten, J., Vander Perre, G., Alaerts, I., Berckmans, D., 2006. Biomechanical properties of the superior sagittal sinus-bridging veins complex. Stapp Car Crash J. Nov;50:625-36.

[35] Kiliç, T., Akakin, A., 2008. Anatomy of cerebral veins and sinuses. Front. Neurol. Neurosci. 23:4-15.

[36] Anatomy & Physiology of the vascular access system, Bard UK. Retrieved April 18, 2019 from http://www.quidditymedia.co.uk/access/anatomy.html.

[37] Nierenberger, M., Wolfram-Gabel, R., Decock-Catrin, S., Boehm, N., Rémond, Y., Kahn, J.L., Ahzi, S., 2013a. Investigation of the human bridging veins structure using optical microscopy. Surg. Radiol. Anat. May;35(4):331-7.

[38] Si, Z., Luan, L., Kong, D., Zhao, G., Wang, H., Zhang, K., Yu, T., Pang, Q., 2008. MRI-based investigation on outflow segment of cerebral venous system under increased ICP condition. Eur. J. Med. Res. Mar 31; 13(3):121-6.

[39] Famaey, N., Vander Sloten, J., 2008. Soft tissue modelling for applications in virtual surgery and surgical robotics. Comput. Methods Biomech. Biomed. Eng. Aug; 11(4):351-66.

[40] Silver, F.H., Snowhill, P.B., Foran, D.J., 2003. Mechanical behaviour of vessel wall: a comparative study of aorta, vena cava, and carotid artery. Ann. Biomed. Eng. Jul-Aug; 31(7):793-803.

[41] Holzapfel, G., Gasser, T., Stadler, M., 2002. A structural model for the viscoelastic behaviour of arterial walls: continuum formulation and finite element analysis. Eur. J. Mech. A/Solids 21(3), 441-463.

[42] Zulliger, M.A., Kwak, N.T.M.R., Tsapikouni, T., Stergiopulos, N., 2002. Effects of longitudinal stretch on VSM tone and distensibility of muscular conduit arteries. Am. J. Physiol. Heart Circ. Physiol. Dec; 283(6):H2599-605.

[43] Holzapfel, G.A.; Gasser, T.C.; Ogden, R.A.Y.W., 2000. A new constitutive frame work for arterial wall mechanics and a comparative study of material models. J.Elast.61,1-48.

[44] Fung, Y.C, Cowin, S.C., 1994. Biomechanics: Mechanical Properties of Living Tissues, 2nd ed.." ASME. J. Appl. Mech. December 61(4): 1007.

[45] Kleiven, S., 2007. Predictors for traumatic brain injuries evaluated through accident reconstructions. StappCarCrashJ. Oct; 51:81-114.

[46] Gasser, T.C., Ogden, R.W., Holzapfel, G.A., 2006. Hyperelastic modelling of arterial layers with distributed collagen fibre orientations. J. R. Soc. Interface3 Feb 22; 3(6):15-35.

[47] Rezakhaniha, R., Stergiopulos, N., 2008. A structural model of the venous wall considering elastin anisotropy. J. Biomech. Eng. Jun; 130(3):031017.

[48] Nierenberger, M., Rémond, Y., Ahzi, S., 2013b. A new multiscale model for the mechanical behavior of vein walls. J. Mech. Behav .Biomed. Mater. Jul; 23:32-43.

[49] Fung, Y.C., 1993. Biomechanics Mechanical Properties of Living Tissues. Springer-Verlag New York.

[50] Löwenhielm, P., 1974. Dynamic properties of the parasagittal bridging veins. Z. Rechtsmed Mar 29; 74(1):55-62.

[51] Löwenhielm, P., 1975. Mathematical simulation of gliding contusions. J. Biomech. 8(6):351-6.

[52] Schmitt, K., Niederer, P., Muser, M., Walz, F., 2007. Trauma Biomechanics - Accidental injury in traffic and sports. Springer-Verlag Berlin Heidelberg, Second edition, chapter 3.

[53] Caring For Special Needs Kids, 2016. Retrieved April 23, 2019 from http://caringforspecialneedskids.com/infant-skull-fracture.

[54] Cooper, P.R., 1982. Post-traumatic intracranial mass lesions. In: Cooper PR (ed) Head injury. Williams and Wilkins, Baltimore London, pp 185-232.

[55] Oehmichen, M., Auer, R.N., König, H.G., 2006. Forensic Neuropathology and Associated Neurology. Springer-Verlag Berlin Heidelberg, First edition.

[56] Gennarelli, T.A, 1983. Head injury in man and experimental animals: Clinical aspects. Acta Neurochirurgica Supplementum 32:1-13.

[57] Sahuquillo-Barris, J., Lamarca-Ciuro, J., Vilalta-Castan, J., Rubio-Garcia, E., Rodriguez-Pazos, M., 1988. Acute subdural hematoma and diffuse axonal injury after severe head trauma. J. Neurosurg. Jun; 68(6):894-900.

[58] Lineage Medical, Inc., 2019. Retrieved April 23, 2019 from https://step2.medbullets.com/neurology/120300/subdural-hematoma.

[59] Melvin J.W., Lighthall J.W. (2002) Brain-Injury Biomechanics. In: Nahum A.M., Melvin J.W. (eds) Accidental Injury. Springer, New York, NY

[60] Whitaker, J., 1980. A survey of motorcycle accidents. TRRL Laboratory Report LR 913, Crowthorne.

[61] Clayton E.H., Genin G.M., Bayly P.V. Transmission, attenuation and reflection of shear waves in the human brain. J R Soc Interface. 2012 Nov 7; 9(76):2899-2910.

[62] Wright R.M. et al. A multiscale computational approach to estimating axonal damage under inertial loading of the head. J Neurotrauma. 2013 Jan 15; 30(2):102-18.

[63] Su E., Bell M., Diffuse Axonal Injury. In: Laskowitz D, Grant G, editors. Translational Research in Traumatic Brain Injury. Boca Raton (FL): CRC Press/Taylor and Francis Group; 2016. Chapter 3.

[64] Meythaler J.M. et al. Current concepts: Diffuse axonal injury-associated traumatic brain injury. Arch Phys Med Rehabil. 2001; 82(10):1461-1471.

[65] Gennarelli, T.A; Thibault, L.E.; Adams, J.H.; Graham, D.I.; Thompson, C.J.; Marcincin, R.P., 1982b. Diffuse axonal injury and traumatic coma in the primate. Ann. Neurol. Dec; 12(6):564-74.

[66] Gennarelli, T.A., 1981. Mechanistic approach to head injuries: clinical and experimental studies of the important types of injury. Ed. Ommaya, A.K., in Head and neck injury criteria: a consensus workshop, U.S. Dept. of Transportation, National Highway Traffic Safety Administration, Washington DC, pp. 20-25.

[67] AccidentAttorneys.org. (2013). Brain Injury: What is a Diffuse Axonal Injury? Retrieved April 25, 2019 from https://accidentattorneys.org/brain-injury-diffuse-axonal-injury/.

[68] Tarriere, C. (1981) Risk of head and neck injury if there is no direct head impact, in Proceedings of Head and Neck Injury Criteria: A Consensus Workshop, Session 1, National Highway Traffic Safety Administration, Washington, DC, pp. 13-15.

[69] McLean, A. J. (1995) Brain injury without head impact? Journal of Neurotrauma Aug; 12(4):621-5.

[70] Yanagida, Y., Fujiwara, S. and Mizoi, Y. (1989)Differences in the intracranial pressure caused by a 'blow' and/or a 'fall'–an experimental study using physical models of the head and neck. Forensic Science International, Apr-May; 41(1-2):135-45.

[71] McLean, A. J. and Anderson W. G. Robert. Biomechanics of closed head injury. Head injury: pathophysiology and management. Published in 1997 by Chapman & Hall, London. ISBN 0 412 58540 5.

[72] Schneider, D. and Nahum, A. Impact studies of facial bones and skull. In: 16th Stapp car crash conference, Detroit, MI, November 1972, paper no. 720965. Warrendale, PA: SAE International.

[73] Nahum, A., Gatts, J., Gadd, C. and Danforth, J. Impact tolerance of the skull and face. In: 12th Stapp car crash conference, Detroit, MI, October 1968, paper no. 680785. Warrendale, PA: SAE International.

[74] Yoganandan, N., Sances, A., Pintar, F.A., Walsh, P.R., Ewing, C.L., Thomas, D.J., et al. Biomechanical tolerance of the cranium. In: International off-highway & powerplant congress & exposition, Warrendale, PA, October 1994, paper no. 94172. Warrendale, PA: SAE International.

[75] Allsop, D., Warner, C., Wille, M. and Schneider, D. Facial impact response - A comparison of the hybrid III dummy and human cadaver. In: 32nd Stapp car crash conference, Atlanta, GA, October 1988, paper no. 881719. Warrendale, PA: SAE International.

[76] Hodgson, V.R. and Thomas, L.M. Breaking strength of the human skull vs. impact surface curvature. Report, Wayne State University School of Medicine, USA, 1971.

[77] Advani, S.H., Huston, J. and Ojala, S.J. Human head impact response. Experimental data and analytical simulations. In: IRCOBI conference, Birmingham, UK, September 1975, pp. 153-163. Zurich, Switzerland: IRCOBI.

[78] Voo, L., Pintar, F., Yoganandan, N., Sances, A., Ewing, C.L., Thomas, D.J., et al. Biomechanical analysis of tractor induced head injury. In: International off-highway & powerplant congress & exposition, Warrendale, PA, October 1994, paper no. 941726. Warrendale, PA: SAE International.

[79] Allsop, D., Perl, T. and Warner, C. Force/deflection and fracture characteristics of the temporo-parietal of the human head. In: 35th Stapp car crash conference, San Diego, CA, November 1991, paper no. 912907. Warrendale, PA: SAE International.

[80] Advani, S., Ommaya, A. and Yang, W. Head injury mechanisms. In: Ghista DN (ed) Human body dynamics. Oxford: Oxford University Press, 1982.

[81] Hume, A., Mills, N.J. and Gilchrist, A. Industrial head injuries and the performance of the helmets. In: 1995 IRCOBI conference, Brunnen, Switzerland, 13-15 September 1995. pp. 217-231. Zurich, Switzerland: IRCOBI.

[82] Holbourn, A. H. S. (1943) Mechanics of head injuries. Lancet, ii, 438-441.

[83] Cairns, H. and Holbourn, H., (1943). Head injuries in motor-cyclists: with special reference to crash helmets. British Medical Journal, 15 May, 591-598.

[84] Ommaya, A.K. and Gennarelli, T.A. (1974) Cerebral concussion and traumatic unconsciousness. Brain, Dec; 97(4):633-54.

[85] Gurdjian, E.S., Webster, J.E., Lissner, H.R., Observations on the mechanism of brain concussion, contusion and laceration, Surgery, Gynecology and Obstetrics. Surg Gynecol Obstet. 1955 Dec; 101(6):680-90.

[86] Gurdjian, E.S., Lissner, H.R., Latimerr, F.R., Haddad, B.F., Webster, J.E., Quantitative determination of acceleration and intracranial pressure in experimental head injury. Neurology, 1953 Jun; 3(6):417-23.

[87] Wismans, J., 1994. Injury biomechanics. Second printing edition, no. 4552, Eindhoven University of Technology, The Netherlands.

[88] van den Bosch HLA. Crash helmet testing and design specifications. PhD Thesis, Technische Universiteit Eindhoven, The Netherlands, 2006.

[89] Hayes, W.C., Erickson, M.S., Power, E.D., 2007. Forensic Injury Biomechanics. The Annual Review of Biomedical Engineering 9:55-86.

[90] Got, C., Patel, A., Fayon, A., Tarrière, C. et al., "Results of Experimental Head Impacts on Cadavers: The Various Data Obtained and Their Relations to Some Measured Physical Parameters," SAE Technical Paper 780887, 1978

[91] Stalnaker, R.L., McElhaney, J.H. and Roberts, V.L. MSC tolerance curve for human heads to impact. In: ASME biomechanical and human factors conference, New York, November-December 1971, paper no. 71-WA/BHF-10. New York: ASME.

[92] Versace, J. A review of the severity index. In: 15th Stapp car crash conference, Coronado, CA, November 1971, paper no. 710881. New York: SAE International.

[93] Peng, Y., Deck, C., Yang, J., Otte, D. and Willinger, R. A study of kinematics of adult pedestrian and head impact conditions in case of passenger car collisions based on real world accident data. In: IRCOBI conference, Dublin, Ireland, 12-14 September 2012, pp. 766-778. Zurich, Switzerland: IRCOBI.

[94] Newman, J.A. A generalized model for brain injury threshold (GAMBIT). In: 1986 IRCOBI conference, Zurich, Switzerland, September, pp. 121-131. Zurich, Switzerland: IRCOBI.

[95] Mertz, H., Prasad, P. and Irwin, A. Injury risk curves for children and adults in frontal and rear collisions. In: 41st Stapp car crash conference, Lake Buena Vista, FL, November 1997, paper no. 973318. Warrendale, PA: SAE International.

[96] King, A., Yang, K., Zhang, L., Hardy, W. and Viano, D. Is head injury caused by linear or angular acceleration? In: IRCOBI conference, Lisbon, Portugal, September 2003, pp. 1-10. Zurich, Switzerland: IRCOBI.

[97] Newman, J., Barr, C., Beusenberg, M., Fournier, E., Shewchenko, N., Welbourne, E., et al. A new biomechanical assessment of mild traumatic brain injury. Part 2: Results and conclusions. In: IRCOBI conference, Montpellier, France, 20-22 September 2000. pp. 223-233. Zurich, Switzerland: IRCOBI.

[98] Zhang, L., Yang, K. and King, A. A proposed injury threshold for mild traumatic brain injury. J. Biomech. Eng. 2004; 126(2): 226-236.

[99] Duma, S.M., Manoogian, S.J., Bussone, W.R., Brolinson, P.G., Goforth, M.W., Donnenwerth, J.J., et al. Analysis of realtime head accelerations in collegiate football players. Clin. J. Sports. Med. 2005; 15:3-8.

[100] Guskiewicz, K.M., Mihalik, J.P., Shankar, V., Marshall, S.W., Crowell, D.H., Oliaro, S.M., et al. Measurement of head impacts in collegiate football players: Relationship between head impact biomechanics and acute clinicaloutcome after concussion. Neurosurg 2007; 61(6):1244-1253.

[101] Rowson, S. and Duma, S. Development of the STAR evaluation system for football helmets: Integrating player head impact exposure and risk of concussion. Ann. Biomed. Eng. 2011; 39(8): 2130-2140.

[102] McAllister, T.W., Ford, J.C., Ji, S., Beckwith, J.G., Flashman, L.A., Paulsen, K., et al. Maximum principal strain and strain rate associated with concussion diagnosis correlates with changes in corpus callosum white matter indices. Ann. Biomed. Eng. 2012; 40(1): 127-140.

[103] McIntosh, A.S., Patton, D.A., Fréchède, B., Pierré, P., Ferry, E. and Barthels, T. The biomechanics of concussion in unhelmeted football players in Australia: A case-control study. Br. Med. J. 2014; 4(5):1-9.

[104] Shuaeib, F.M., Hamouda, A.M.S., Umar, R.S.R., Hamdan, M.M. and Hashmi, M.S.J. Motorcycle helmet: Part I. Biomechanics and computational issues. J Mater Process Technol 2002; 123(3): 406-421.

[105] Hopes, P.D. and Chinn, B.P. Helmets: A new look at design and possible protection. In: IRCOBI conference, Stockholm, Sweden, September 1989, pp. 39-54. Zurich, Switzerland: IRCOBI.

[106] Horgan, T.J. A finite element model of the human head for use in the study of pedestrian accidents. PhD Thesis, University College Dublin, Ireland, 2005.

[107] Marjoux, D., Baumgartner, D., Deck, .C and Willinger, R. Head injury prediction capability of the HIC, HIP, SIMon and ULP criteria. Accid Anal Prev 2008; 40(3):1135-1148.

[108] Hertz, E., 1993. A note on the head injury criterion (HIC) as a predictor of the risk of skull fracture, 37th Annual Proceedings of the Association for the Advancement of AutomotiveMedicine.

[109] Gennarelli, T.A., Pintar, F.A. and Yoganandan, N. Biomechanical tolerances for diffuse brain injury and a hypothesis for genotypic variability in response to trauma. In: 47th american association for automotive medicine annual conference, San Diego, CA, October 2003, pp. 624-628. Denver: AAAM.

[110] Löwenhielm, P. Strain tolerance of the Vv. cerebri sup. (bridging veins) calculated from head-on collision tests with cadavers. Z. Rechtsmed 1974; 75(2):131-144.

[111] Löwenhielm, P. Tolerance levels for bridging vein disruption calculated with a mathematical model. J Biosci. Bioeng. 1978; 2: 501-507.

[112] Ommaya, A.K., Hirsch, A.E., Yarnell, P. and Harris, E.H. Scaling of experimental data in cerebral concussion in sub-human primates to concussive threshold for man. In: 11th Stapp car crash conference, New York, USA, November 1967, pp. 47-52. Warrendale, PA: SAE International.

[113] Ommaya, A.K. and Hirsch, A.E. Tolerances for cerebral concussion from head impact and whiplash in primates. J. Biomech. 1971; 4(1): 13-21.

[114] Unterharnscheidt, F. and Higgins, L.S. Traumatic lesions of brain and spinal cord due to non-deforming angular acceleration of the head. Texas Rep Biol Med 1969; 27(1): 127-166.

[115] Ono, K., Kikuchi, A., Nakamura, M., Kobayashi, H. and Nakamura, N. Human head tolerance to sagittal impact: Reliable estimation deduced from experimental head injury using subhuman primates and human cadaver skulls. In: 24th Stapp car crash conference, Troy, MI, October 1980, paper no. 801302. Warrendale, PA: SAE International.

[116] Pincemaille, Y., Trosseille, X., Mack, P. and Tarrière, C. Some new data related to human tolerance obtained from volunteer boxers. Report for the SAE. Report no. 892435, 1 October 1989. Warrendale, PA: SAE International.

[117] Thibault, L.E., Gennarelli, T.A., Margulies, S.S., Marcus, J. and Eppinger, R. The strain dependent pathophysiological consequences of inertial loading on central nervous system tissue. In: IRCOBI conference, Berlin, Germany, September 1990, pp. 191-202. Zurich, Switzerland: IRCOBI.

[118] Newman, J.A., Shewchenko, N. and Welbourne, E. A new biomechanical head injury assessment function: The maximum power index. Stapp Car Crash J 2000; 44: 215-247.

[119] Viano, D.C., Casson, I.R., Pellman, E.J., Zhang, L., King, A.I. and Yang, K.H. Concussion in professional football: Brain responses by finite element analysis: Part 9. Neurosurg 2005; 57(5): 891-916.

[120] Fijalkowski, R.J., Ellingson, B.M. and Stemper, B.D. Interface parameters of impact induced mild traumatic brain injury. Biomed Sci Instrum 2006; 42: 108-113.

[121] Fijalkowski, R.J., Stemper, B.D., Pintar, F.A., Yoganandan, N. and Gennarelli, T.A. Influence of angular acceleration duration on functional outcomes following mild diffuse brain injury. In: IRCOBI conference, Maastricht, The Netherlands, September 2007, pp. 161-171. Zurich, Switzerland: IRCOBI.

[122] Kleiven, S. Head injury biomechanics and criteria: Biomechanics and neuronics. KTH Royal Institute of Technology, Sweden, 2007.

[123] Pellman, E.J., Viano, D.C., Tucker, A.M., Casson, I.R. and Waeckerle, J.F. Concussion in professional football: Reconstruction of game impacts and injuries. Neurosurg 2003; 53(4): 799-814.

[124] Rowson, S., Duma, S.M., Beckwith, J.G., Chu, J.J., Greenwald, R.M., Crisco, J.J., et al. Rotational head kinematics in football impacts: An injury risk function for concussion. Ann. Biomed. Eng. 2012; 40(1): 1-13.

[125] Broglio, S.P., Schnebel, B., Sosnofff, J.J., Shin, S., Feng, X., He, X., et al. Biomechanical properties of concussions in high school football. Med. Sci. Sports Exercise 2010; 42(11):2064-2071.

[126] Patton, D.A., McIntosh, A.S. and Kleiven, S. The biomechanical determinants of concussion: Finite element simulations to investigate brain tissue deformations during sporting impacts to the unprotected head. J. Appl. Biomech. 2013; 29: 721-730.

[127] Gennarelli, T., Thibault, L., Tomei, G. and Wiser, R. Directional dependence of axonal brain injury due to centroidal and non-centroidal acceleration. In: 31st Stapp car crash conference, New Orleans, LA, 1987, paper no. 872197. Warrendale, PA: SAE International.

[128] Gennarelli, T.I. and Thibault, L.E.. Clinical rationale for a head injury angular acceleration criterion. In: Head injury mechanisms, Washington, DC, USA, October 1989, pp. 5-8. Denver: AAAM.

[129] Margulies, S.S. and Thibault, L.E. A proposed tolerance criterion for diffuse axonal injury in man. J Biomech 1992; 25(8): 917-923.

[130] Ommaya, A., Goldsmith, W. and Thibault, L. Biomechanics and neuropathology of adult and paediatric head injury. Br J Neurosurg 2002; 16(3): 220-242.

[131] Davidsson, J., Angeria, M. and Risling, M.G. Injury threshold for sagittal plane rotational induced diffuse axonal injuries. In: IRCOBI conference, York, UK, September 2009, pp. 43-56. Zurich, Switzerland: IRCOBI.

[132] Yoganandan, N., Pintar, F.A., Zhang, J., Gennarelli, T.A. and Beuse, N. Biomechanical aspects of blunt and penetrating head injuries. In: Gilchrist MD (ed) IUTAM symposium on impact biomechanics: From fundamental insights to applications, Dublin, Ireland, 11-15 July 2005, pp. 173-184. Dordrecht, Netherlands: Springer.

[133] Ewing, C., Thomas, D., Lustick, L., Becker, E., Becker, G., Willems, G., et al. The effect of the initial position of the head and neck to Gx. Impact acceleration. In: 19th Stapp car crash conference, San Diego, CA, November 1975, pp. 487-512. Warrendale, PA: SAE International.

[134] Ommaya, A.K. Biomechanics of head injury. In: Nahum M (ed) Biomechanics of trauma. Norwalk: Appleton-Century-Crofts, 1984.

[135] Tarrière C. Relationship between experimental measuring techniques and real world accidents. In: Head injury symposium, New Orleans, USA, 1987, pp. 47-85. Denver: AAAM.

[136] Thomson, R., Lövsund, P., Norin, H., Jakobsson, L., Boström, O. and Håland, Y. Brain injuries in real world accidents: A multidisciplinary investigation. In: IRCOBI conference, Isle of Man, UK, September 2001, pp. 173-188. Zurich, Switzerland: IRCOBI.

[137] European Cooperation in Science and Technology. COST327: Motorcycle safety helmets. Report for the European Union, 2001.

[138] Mellor, A. and St Clair. V. Advanced motorcycle helmets. In: 19th international technical conference on the enhanced safety of vehicles, Washington, DC, USA, 6-9 June 2005, pp. 1-13. Washington, DC: NHTSA.

[139] Kleiven, S., 2003. Influence of impact direction on the human head in prediction of subdural hematoma. J. Neurotrauma 20(4),365-379.

[140] DiMasi, F., Eppinger, R.H. and Bandak, F.A. Computational analysis of head impact response under car crash loadings. In: 39th Stapp car crash conference, Warrendale, USA, November 1995, paper no. 952718. Warrendale, PA: SAE International.

[141] Bandak, F.A. On the mechanics of impact neurotrauma: A review and critical synthesis. J Neurotrauma 1995; 12(4): 635-649.

[142] Bandak, F.A. Impact traumatic brain injury: A mechanical perspective. In: Oehmichen, M. and König, H.G. (eds) Neurotraumatology-Biomechanic aspects, cytologic and molecular mechanisms. Lübeck: Schmidt-Römhild, 1997, pp. 59-83.

[143] Nahum, A.M., Smith, R. and Ward, C.C. Intracranial pressure dynamics during head impact. In: 21st Stapp car crash conference, New Orleans, LA, 19-21 October 1977, pp. 339-366. Warrendale, PA: SAE International.

[144] Ward, C. and Chan, M. Rotation generated shear strains in the brain. In: 8th annual international workshop on human subjects for biomechanical research, Troy, USA, 14 October 1980, pp. 5-6. Warrendale, PA: SAE.

[145] Raul, J.S., Baumgartner, D., Willinger, R.and Ludes, B. Finite element modelling of human head injuries caused by a fall. Int J Legal Med 2006; 120(4): 212-218.

[146] Willinger, R., Kang, H.S. and Diaw, B. Three-dimensional human head finite-element model validation against two experimental impacts. Ann Biomed Eng 1999; 27(3):403-410.

[147] Baumgartner D. Mécanismes de lésion et limites de tolérance au choc de la tête humaine - Reconstruction numérique et expérimentale de traumatismes crâniens. PhD Thesis, Université Louis Pasteur, France, 2001.

[148] Yao, J., Yang, J. and Otte, J. Investigation of brain injuries by reconstructions of real world adult pedestrian accidents. In: IRCOBI conference, Madrid, Spain, 2006, pp. 241-252. Zurich, Switzerland: IRCOBI.

[149] Yao, J., Yang, J. and Otte, D. Investigation of head injuries by reconstructions of real-world vehicle-versus-adultpedestrian accidents. Saf Sci 2008; 46(7): 1103-1114.

[150] Kang, H., Willinger, R., Diaw, B.M. and Chinn, B. Validation of a 3D anatomic human head model and replication of head impact in motorcycle accident by finite element modelling. SAE Trans 1997; 41: 849-858.

[151] Anderson, R. A study of the biomechanics of axonal injury. PhD Thesis, University of Adelaide, Australia, 2000.

[152] Willinger, R., Baumgartner, D., Chinn, B. and Neale, M. Head tolerance limits derived from numerical replication of real world accidents. In: IRCOBI conference, Montpellier, France, 20-22 September 2000, pp. 209-222. Zurich, Switzerland: IRCOBI.

[153] Deck, C., Baumgartner, B. and Willinger, R. Helmet optimisation on head-helmet modelling. Struct Mater 2003; 13: 319-328.

[154] Baumgartner, D., Willinger, R., Shewchenko, N. and Beusenberg, M. Tolerance limits for mild traumatic brain injury derived from numerical head impact replication. In: IRCOBI conference, Isle of Man, UK, September 2001, pp. 353-355. Zurich, Switzerland: IRCOBI.

[155] Willinger, R. and Baumgartner, D. Human head tolerance limits to specific injury mechanisms. Int J Crashworthiness 2003; 8(6): 605-617.

[156] Willinger, R. and Baumgartner, D. Numerical and physical modelling of the human head under impact - Toward new injury criterion. Int J Veh Des 2003; 32(1-2): 94-115.

[157] Deck, C. and Willinger, R. Improved head injury criteria based on head FE model. Int J Crashworthiness 2008; 13(6): 667-678.

[158] Hardy, C. and Marcal, P. (1973), "Elastic analysis of a skull", Journal of Applied Mechanics, Vol. 40 No. 4, pp. 838-842.

[159] Shugar, T.A. (1975). Transient structural response of the linear skull rain system. In: Proceedings of 19th Stapp Car Crash Conference, San Diego, USA, pp. 581-614: Society of Automotive Engineers (SAE).

[160] Chan, H.S. (1974). Mathematical model for closed head impact. In: Proceedings of 18th Stapp Car Crash Conference, Ann Arbor, USA, pp. 557-579: Society of Automotive Engineers (SAE).

[161] Khalil, T.B. and Hubbard, R. P. (1977). Parametric study of head response by finite element modeling. Journal of Biomechanics 10(2), pp. 119-132.

[162] Hosey, R.R. and K., L.Y. (1981). A homeomorphic finite element model of the human head and neck. In: Simon, B.R., Gallagher, R.H., Johnson, P.C. and Gross, J.F. (Eds.) Finite elements in biomechanics. pp. 379-401: Wiley & Son.

[163] Horgan, T.J. and Gilchrist, M.D. (2003), "The creation of three-dimensional finite element models for simulating head impact biomechanics", International Journal of Crashworthiness, Vol. 8 No. 4, pp. 353-366.

[164] Mao, H., Zhang, L., Jiang, B., Genthikatti, V.V., Jin, X., Zhu, F., Makwana, R., Gill, A., Jandir, G., Singh, A. and Yang, K.H. (2013), "Development of a finite element human head model partially validated with thirty five experimental cases", Journal of Biomechanical Engineering, Vol. 135 No. 11, pp. 111002-111015.

[165] Ruan, J. S., Khatil, T. B. and King, A. I. (1993). Finite element modeling of direct head impact. In: Proceedings of 37th Stapp Car Crash Conference, San Antonio, USA, pp. 69-81: Society of Automotive Engineers (SAE), SAE Paper No. 933114.

[166] Sahoo, D., Deck, C. and Willinger, R. (2014), "Development and validation of an advanced anisotropic visco-hyperelastic human brain FE model", Journal of the Mechanical Behavior of Biomedical Materials, Vol. 33, pp. 24-42.

[167] Takhounts, E.G., Ridella, S.A., Hasija, V., Tannous, R.E., Campbell, J.Q., Malone, D., Danelson, K., Stitzel, J., Rowson, S., Duma, S., 2008. Investigation of traumatic brain injuries using the next generation of simulated injury monitor(SIMon) finite element head model. Stapp Car Crash Journal. 52(November), 1-31.

[168] Yang, J. (2011), "Investigation of brain trauma biomechanics in vehicle traffic accidents using human body computational models", in Wittek, A., Nielsen, P.M.F. and Miller, K. (Eds), Computational Biomechanics for Medicine: Soft Tissues and the Musculoskeletal System, Springer SciencebBusiness Media, LLC.

[169] Zhang, L., Yang, K., Dwarampudi, R., Omori, K., Li, T., Chang, K., Hardy, W.N., Khalil, T.B. and King, A.I. (2001), "Recent advances in brain injury research: a new human head model development and validation", Stapp Car Crash Journal, Vol. 45, pp. 369-394.

[170] Cloots, R.J., Gervaise, H.M., van Dommelen, J.A. and Geers, M.G.D. (2008), "Biomechanics of traumatic brain injury: influences of the morphologic heterogeneities of the cerebral cortex", Annals of Biomedical Engineering, Vol. 36 No. 7, pp. 1203-1215.

[171] Ho, J. and Kleiven, S. (2009), "Can sulci protect the brain from traumatic injury?", Journal of Biomechanics, Vol. 42 No. 13, pp. 2074-2080.

[172] Shugar, T., 1977. A finite element head injury model. In: Theory, Development, and Results, vol. I. Tech. Rep., U.S. Dept. of Transportaton Report No. DOT-HS-289-3-550-IA.

[173] Huang, H.-M.M., 1999. Three-dimensional finite element analysis of subdural hematoma. J. Trauma-Inj. Infect. Crit. Care, 538-544.

[174] Kleiven, S., 2006. Evaluation of head injury criteria using a finite element model validated against experiments on localized brain motion, intracerebral acceleration, and intracranial pressure. Int.J. Crashworthiness 11 (1), 65-79.

[175] Kleiven, S., 2002. Finite Element Modeling of the Human Head (Ph.D.thesis). Royal University of Technology.

[176] Zhou, C., Khalil, T.B., King, A.I., 1995. A new model comparing impact responses of the homogeneous and inhomogeneous human brain. In: Proceedings of the 39th Stapp Car Crash Conference, November 8-10, San Diego, CA, USA (SAE Technical Paper 952714), pp. 121-37.

[177] Zhang, L., Yang, K.H., King, A.I., 2001. Comparison of brain responses between frontal and lateral impacts by finite element modeling. J. Neurotrauma 18 (1), 21-30.

[178] Tchepel, D., Fernandes, F.A.O. and Alves de Sousa, R.J. (2016a), "A more geometrically detailed brain model to evaluate injury: preliminary results", Brain Injury, Vol. 30 Nos 5/6, pp. 481-817.

[179] Miller, R., Margulies, S., Leoni, M., Nonaka, M. et al., "Finite Element Modeling Approaches for Predicting Injury in an Experimental Model of Severe Diffuse Axonal Injury", 42nd Stapp Car Crash Conference Proceedings, 1998-P-337, SAE 1998 Transactions - Journal of Passenger Cars-V107-6.

[180] Teixeira-Dias, F., Pinho-da-Cruz, J., Fontes Valente, R.A., Alves de Sousa, R.j., 2018. Método dos Elementos Finitos - Técnicas de Simulação Númerica em Engenharia. ETEP - Edições Técnicas e Profissionais.

[181] Abaqus User's Manual. Providence, Rohde Island, USA: Dassault Systèmes. Simulia Corporation ABAQUS version 6.10.

[182] Rohatgi, A., 2012. WebPlotDigitalizer: HTML5 based online tool to extract numerical data from plot images. Version 4.2. https://automeris.io/WebPlotDigitizer/.

[183] Depreitere, B. *et al.* (2005) Cerebral Bridging Vein Rupture in Humans. In: Gilchrist M.D. (eds) IUTAM Symposium on Impact Biomechanics: From Fundamental Insights to Applications. Solid Mechanics and Its Applications, vol 124. Springer, Dordrecht.

[184] Cui, Z.Y., Famaey, N., Depreitere, B., Ivens, J., Kleiven, S., Vander Sloten, J. On the assessment of bridging vein rupture associated acute subdural hematoma through finite element analysis. Comput. Methods Biomech. Biomed. Engin. 2017 Apr; 20(5):530-539

[185] The Physics Factbook. Density of blood. Retrieved August 25, 2019, from https://hypertextbook.com/facts/2004/MichaelShmukler.shtml.

[186] Habibi, R., Devendran, c. and Neild, A. Trapping and patterning of large particles and cells in a 1D ultrasonic standing wave. Lab Chip. 2017 Sep 26;17(19):3279-329.

[187] Mayo Foundation for Medical Education and Research. Blood pressure chart: What your reading means. Retrieved August 25, 2019, from https://www.mayoclinic.org/diseases-conditions/high-blood-pressure/in-depth/blood-pressure/art-20050982.

Appendix A

Simulation figures of the fillet impact tests

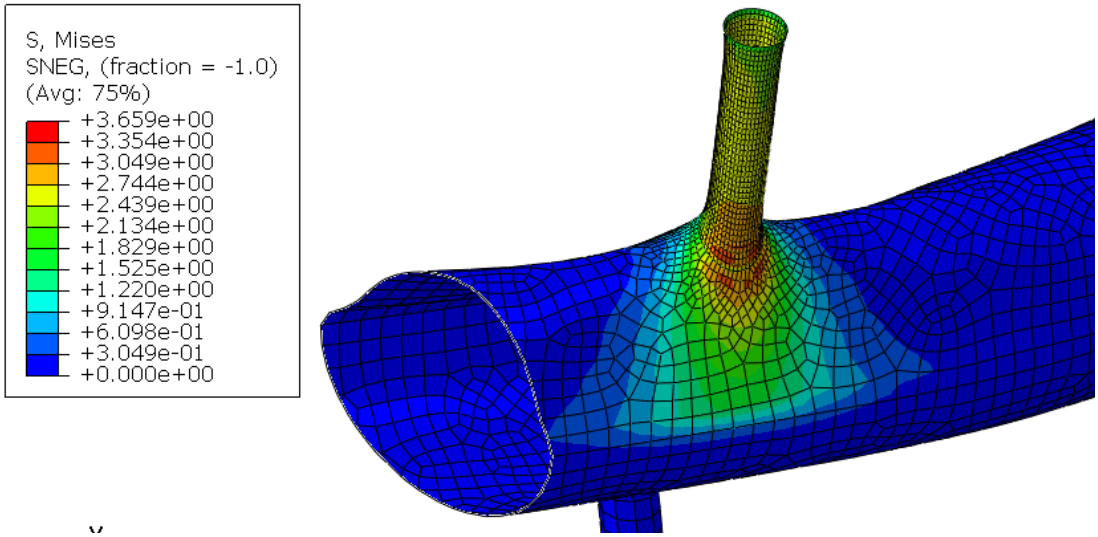

Figure A.1: von Mises stress for the simulation without fillet.

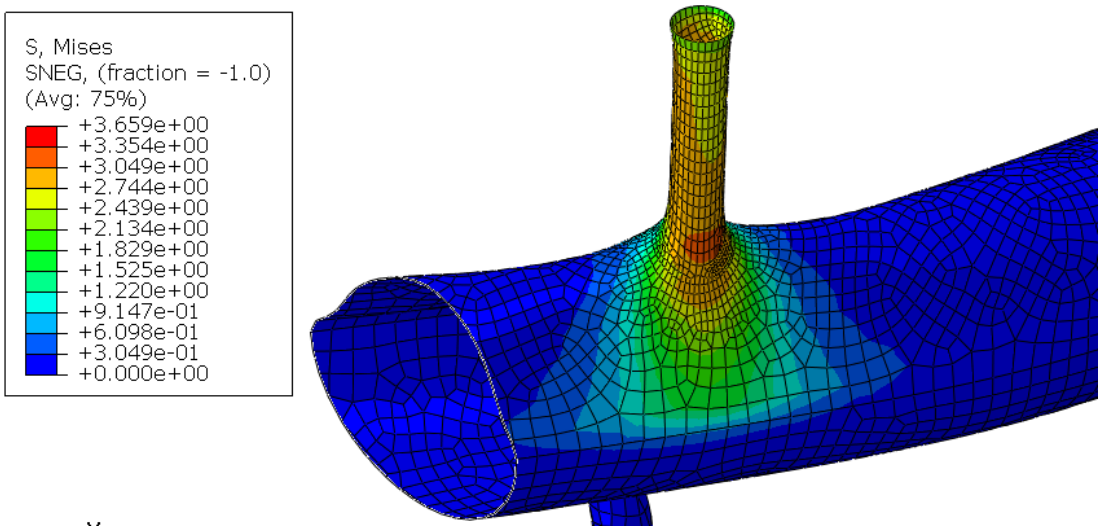

Figure A.2: von Mises stress for the simulation with fillet of size 0.3 mm.

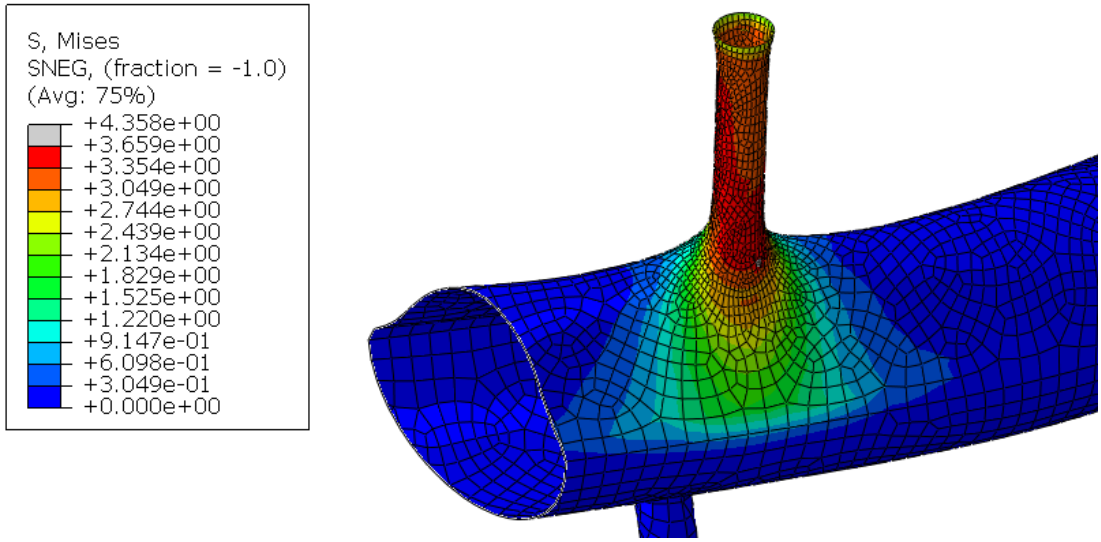

Figure A.3: von Mises stress for the simulation with fillet of size 0.45 mm.

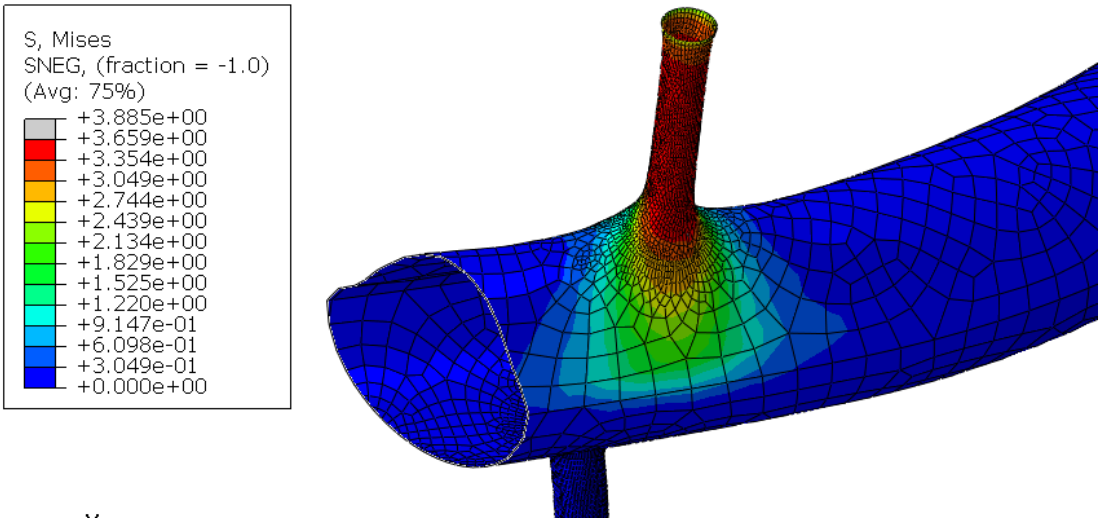

Figure A.4: von Mises stress for the simulation with fillet of size 0.6 mm.

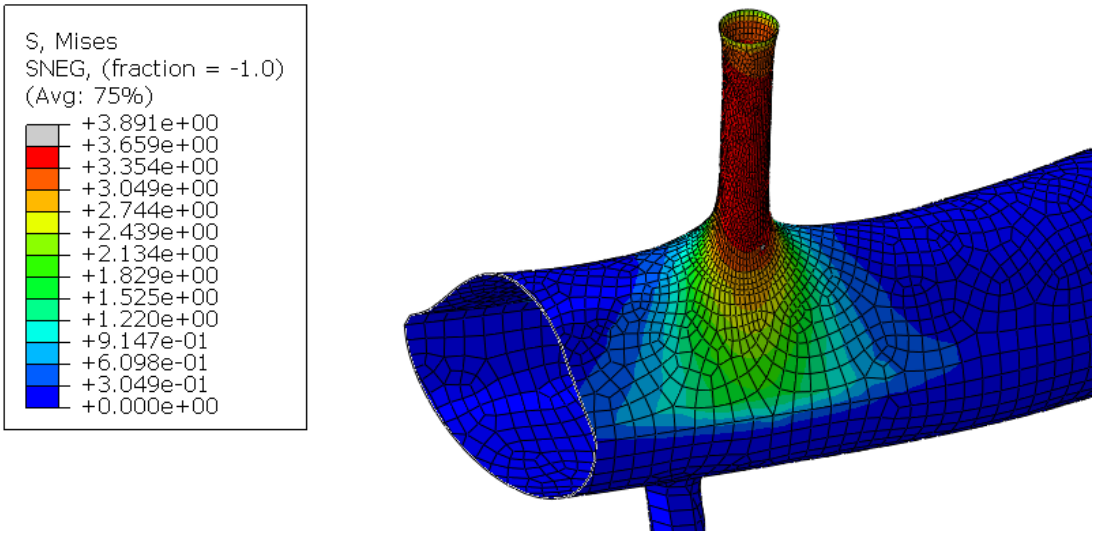

Figure A.5: von Mises stress for the simulation with fillet of size 0.75 mm.

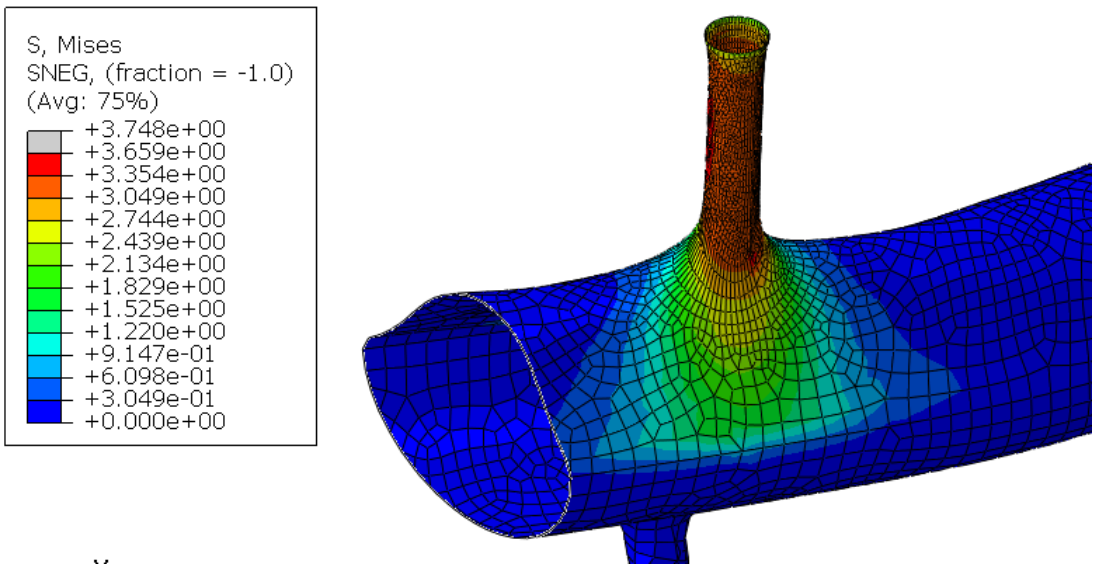

Figure A.6: von Mises stress for the simulation with fillet of size 1 mm.

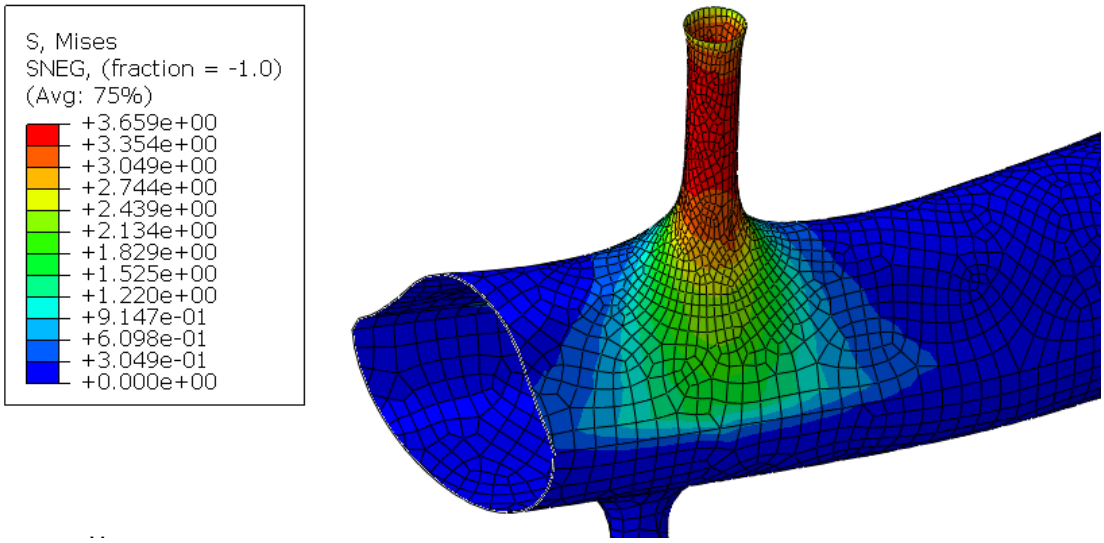

Figure A.7: von Mises stress for the simulation with fillet of size 1.5 mm.

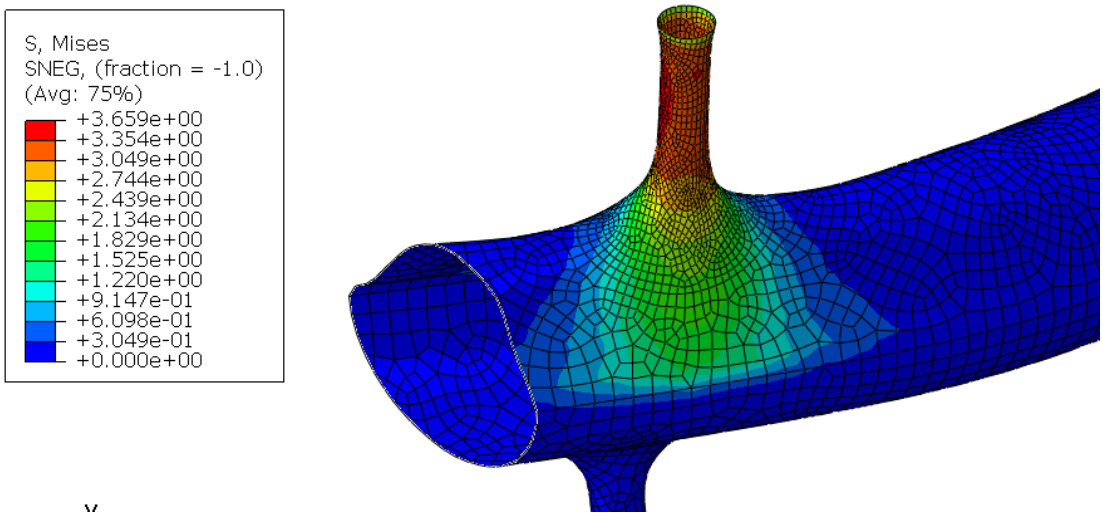

Figure A.8: von Mises stress for the simulation with fillet of size 2 mm.

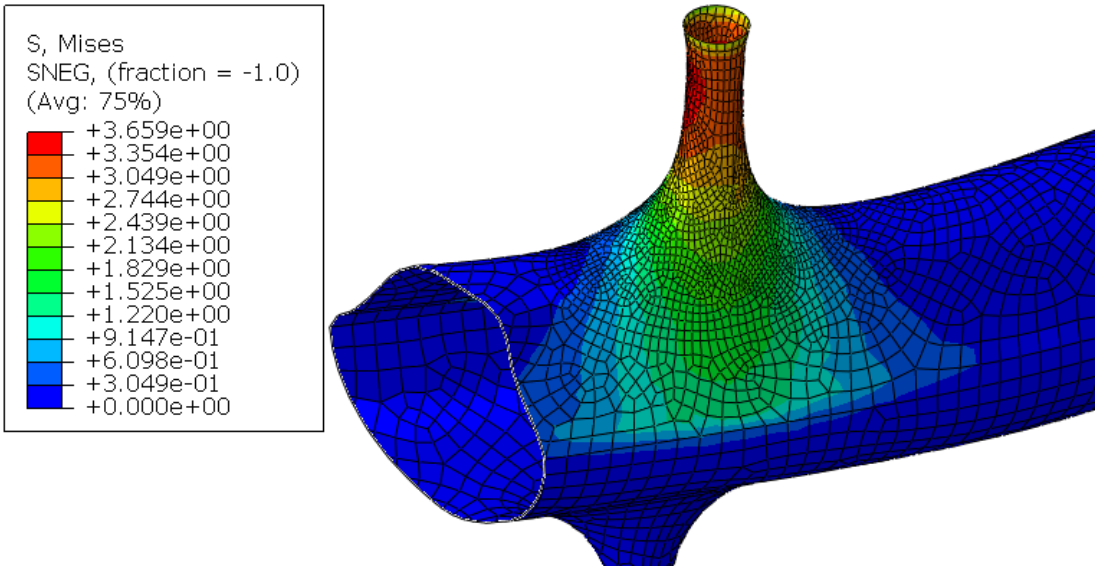

Figure A.9: von Mises stress for the simulation with fillet of size 3 mm.

Appendix B

Acceleration curves

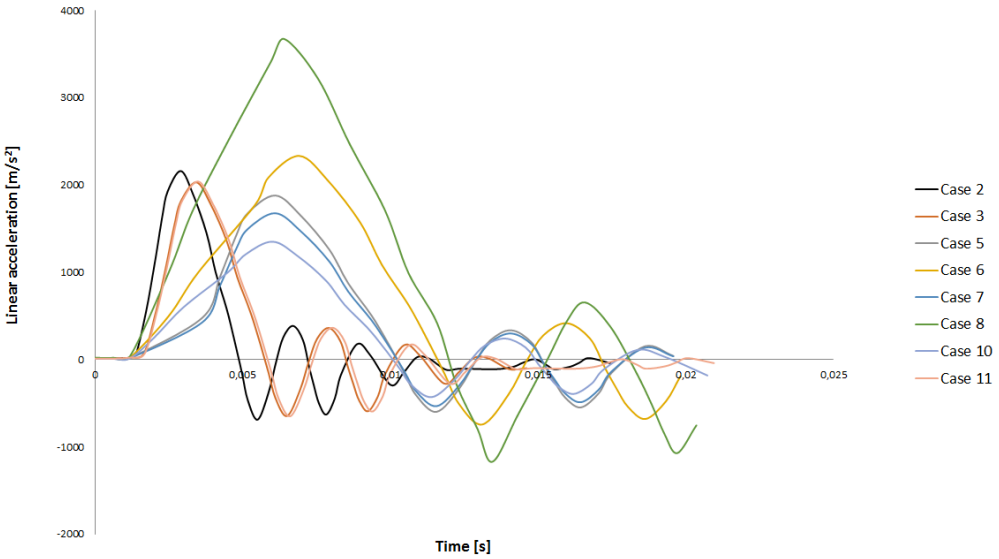

Figure B.1: Linear acceleration curves for the cases without BV rupture.

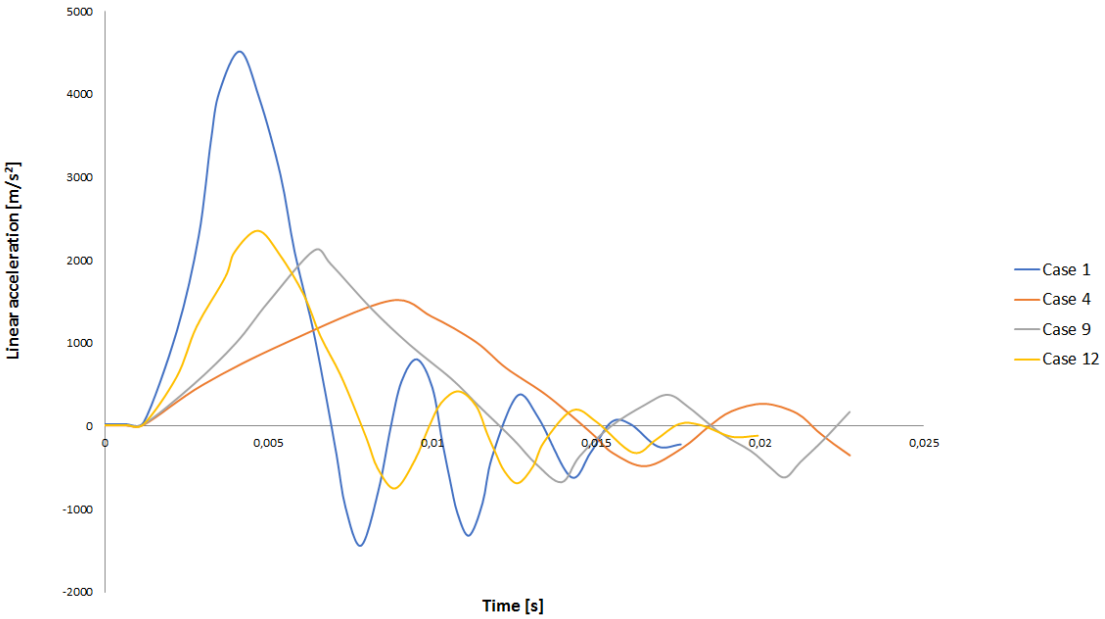

Figure B.2: Linear acceleration curves for the cases with BV rupture.

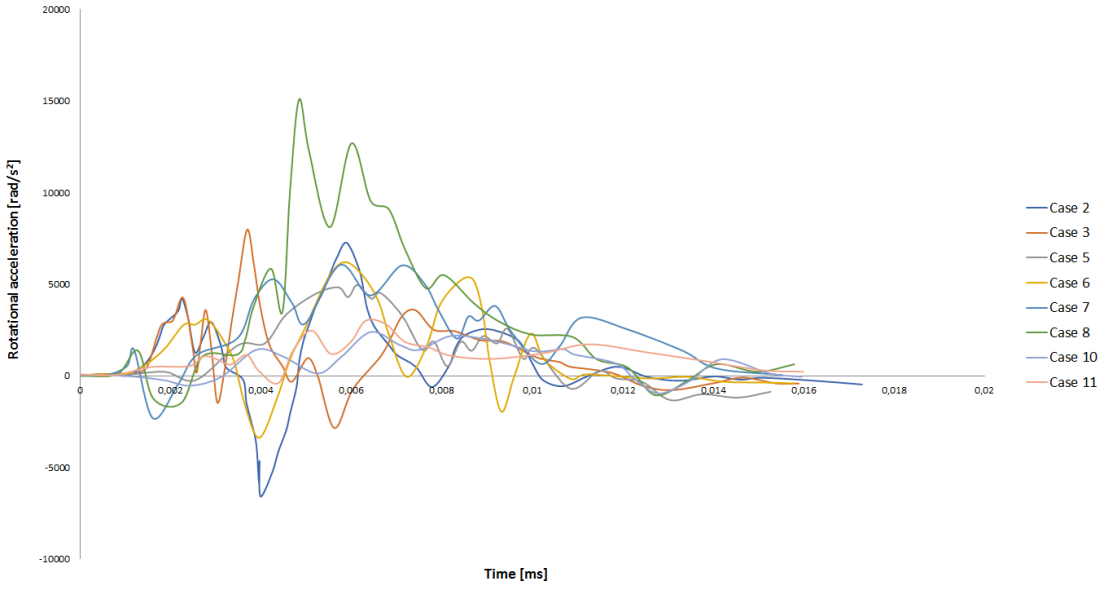

Figure B.3: Rotational acceleration curves for the cases without BV rupture. Adapted from Cui *et al.* [184].

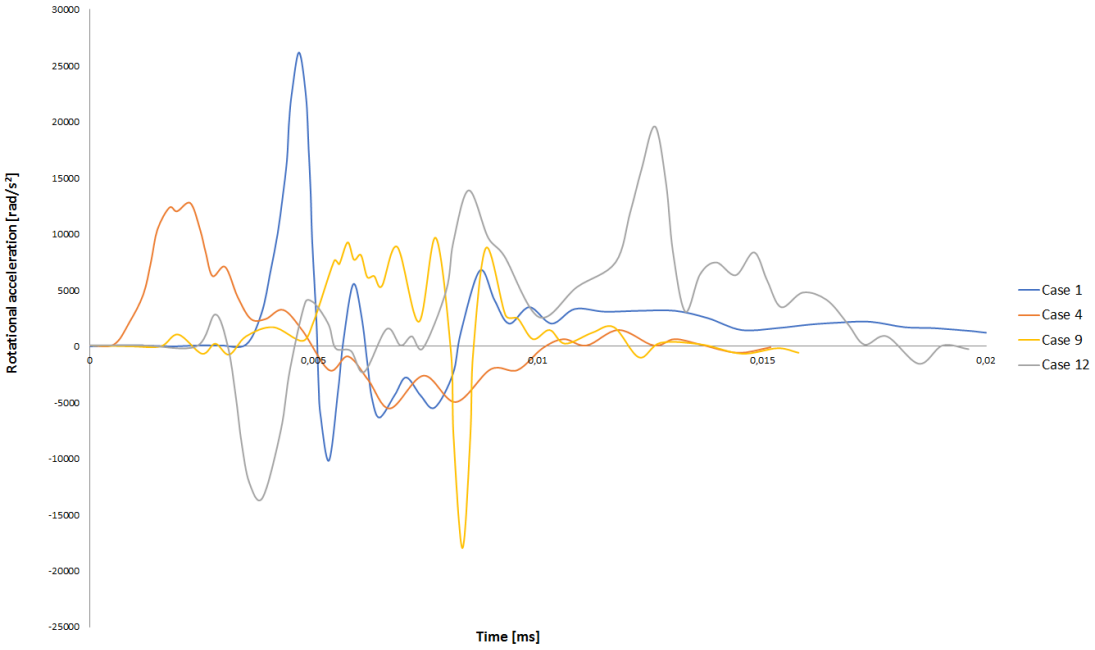

Figure B.4: Rotational acceleration curves for the cases with BV rupture. Adapted from Cui *et al.* [184].

Appendix C

Images of the simulations of the FE model validation

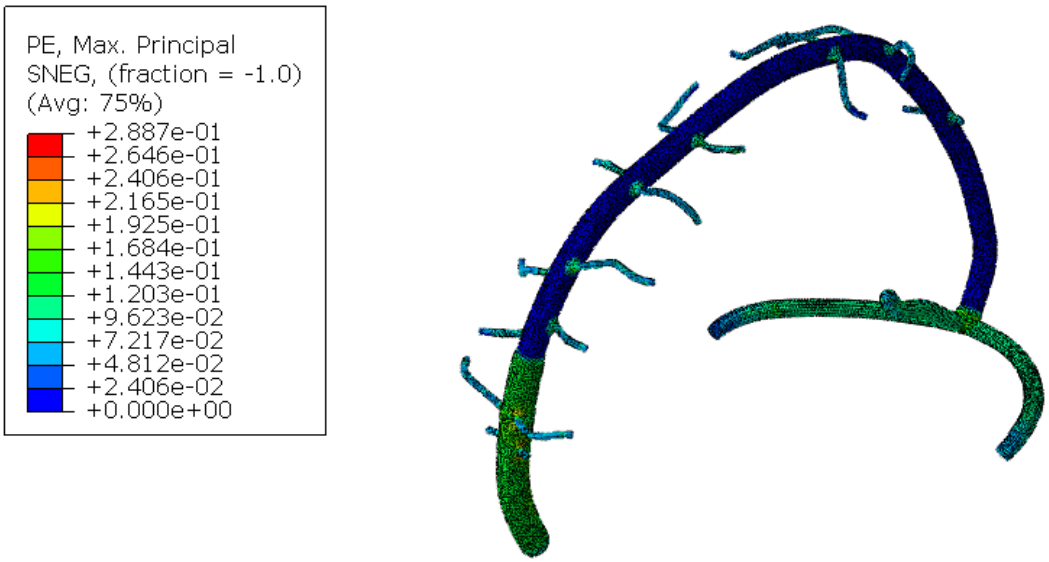

Figure C.1: Maximum PE for case 2.

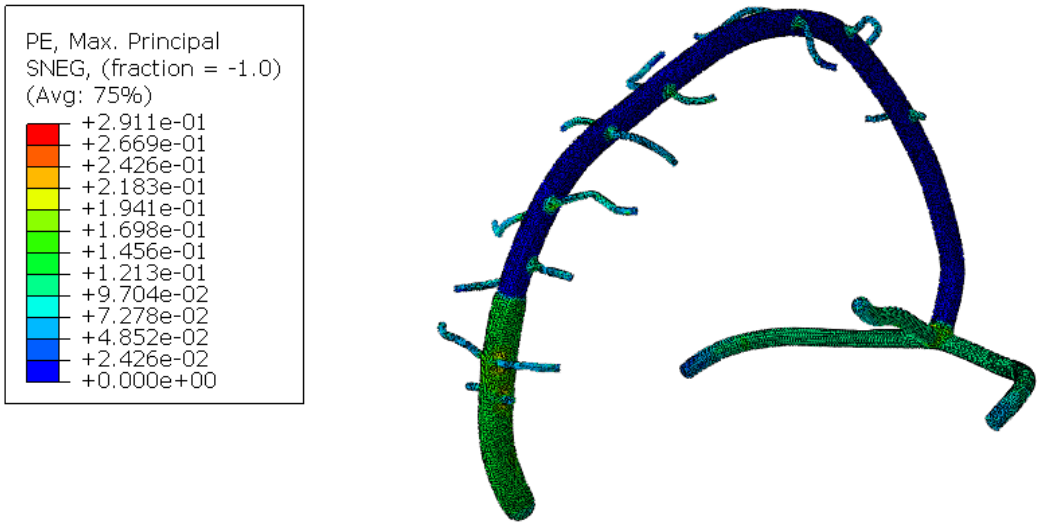

Figure C.2: Maximum PE for case 3.

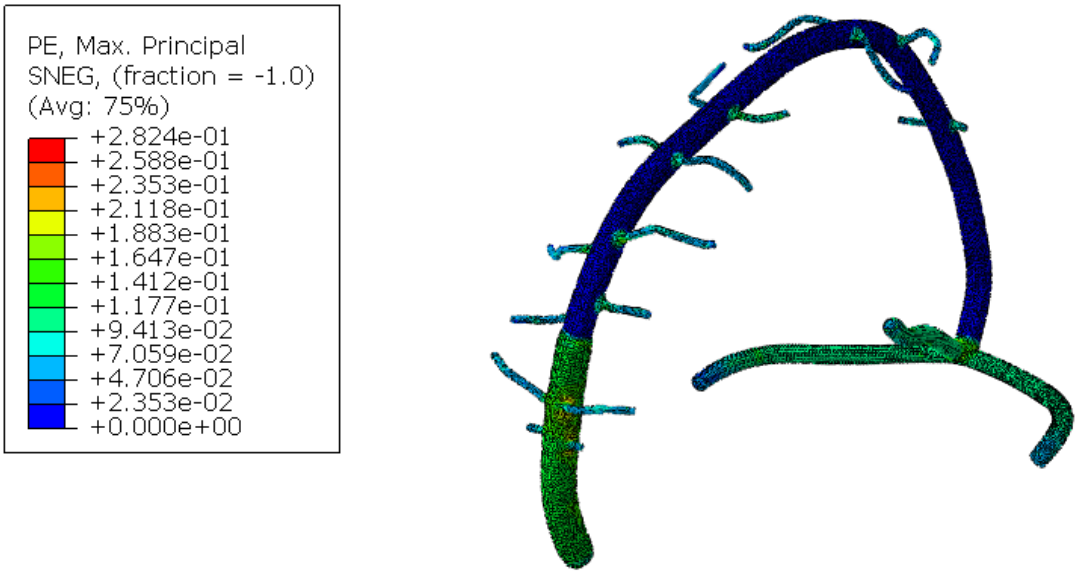

Figure C.3: Maximum PE for case 5.

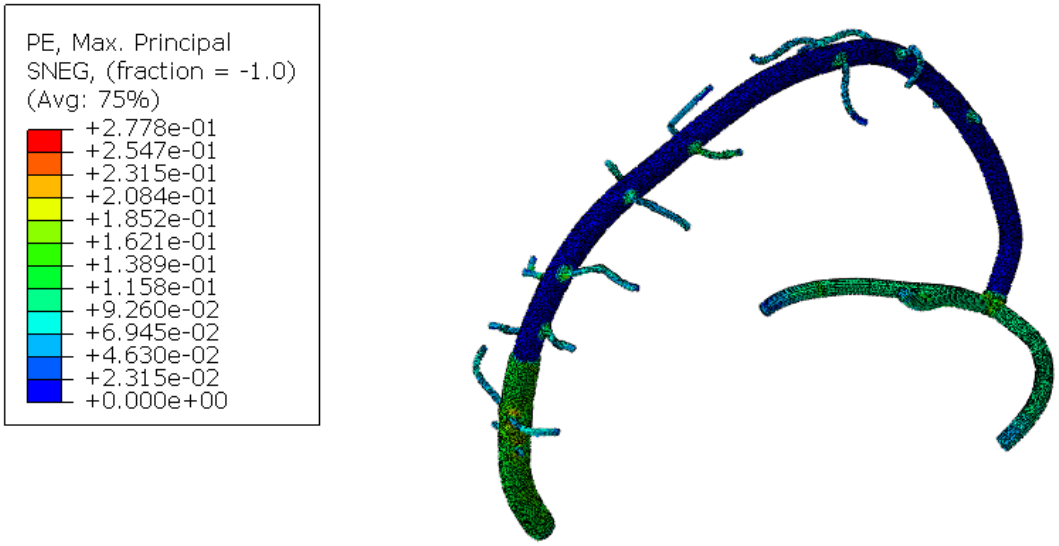

Figure C.4: Maximum PE for case 7.

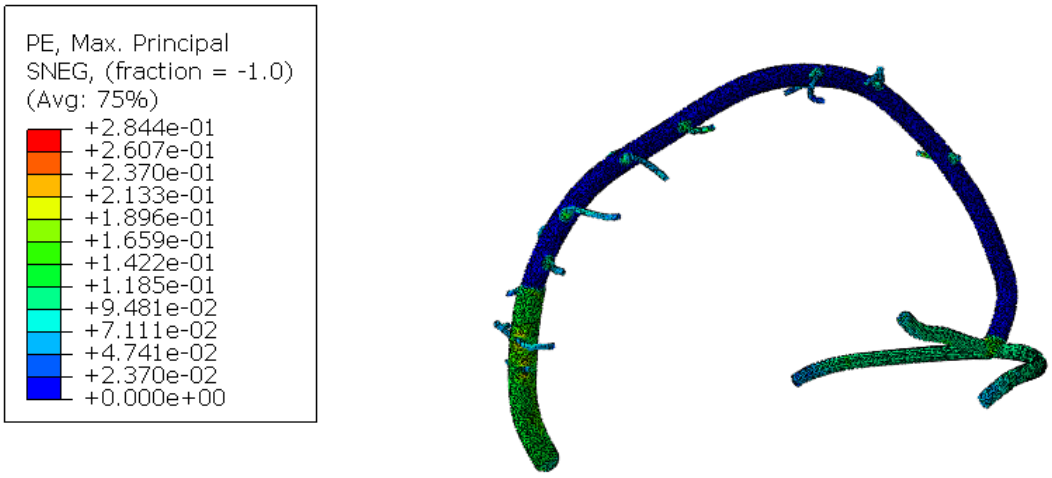

Figure C.5: Maximum PE for case 9.

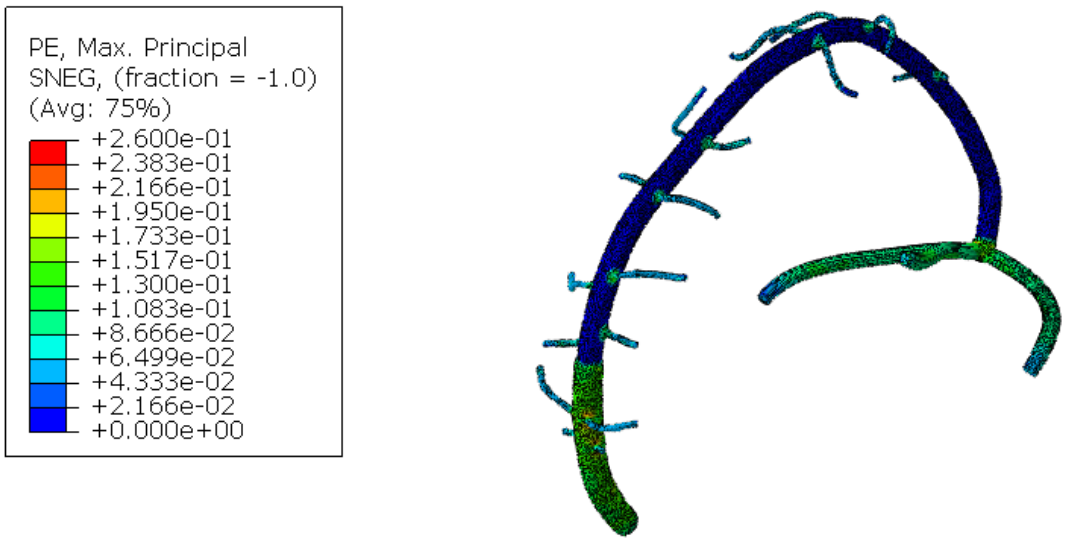

Figure C.6: Maximum PE for case 10.

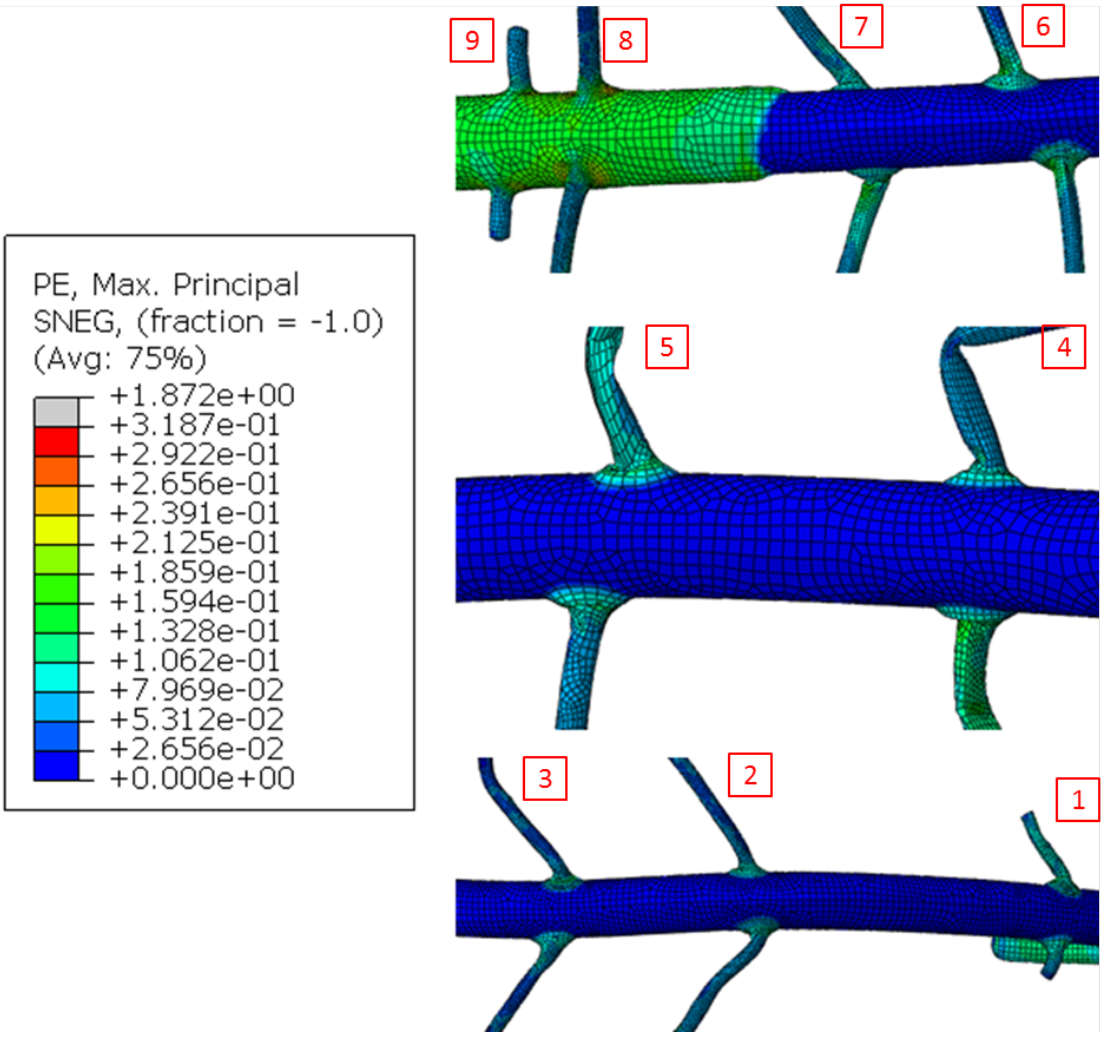

Figure C.7: PE values in the bridging veins for case 6.

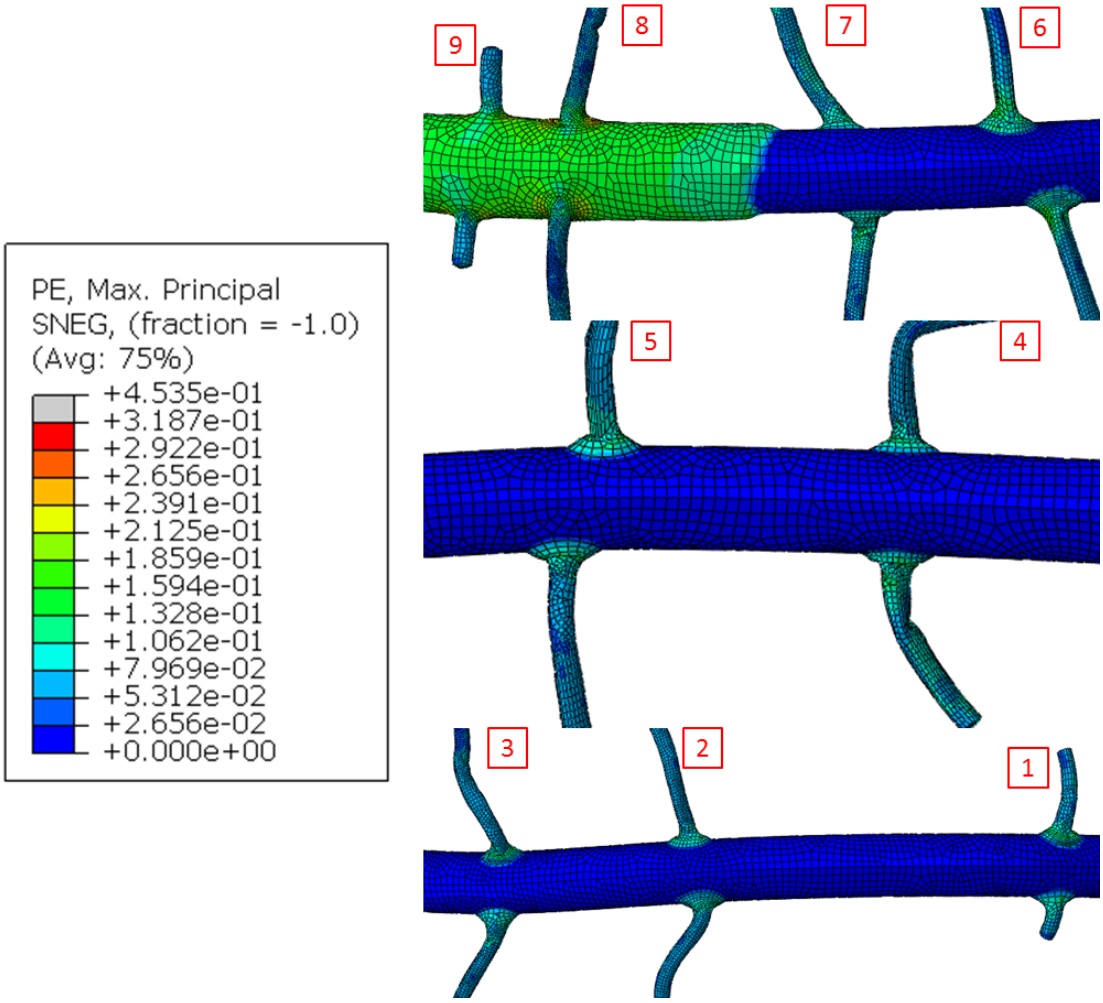

Figure C.8: PE values in the bridging veins for case 11.